

Particle Acceleration in the Inner Heliosphere: Diffusive Shock Acceleration and Quiet-Time Processes

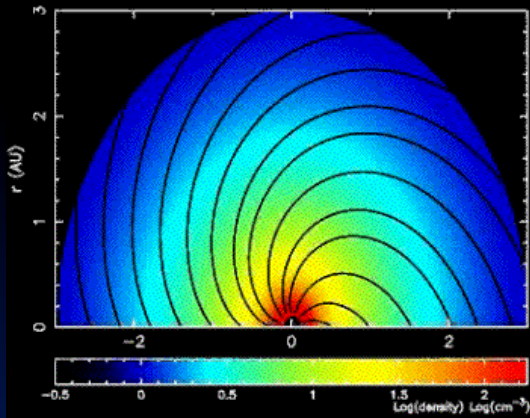
G.P. Zank

Gang Li, Olga Verkhoglyadova

Center for Space and Aeronomic Research (CSPAR)

Department of Space Science

University of Alabama in Huntsville



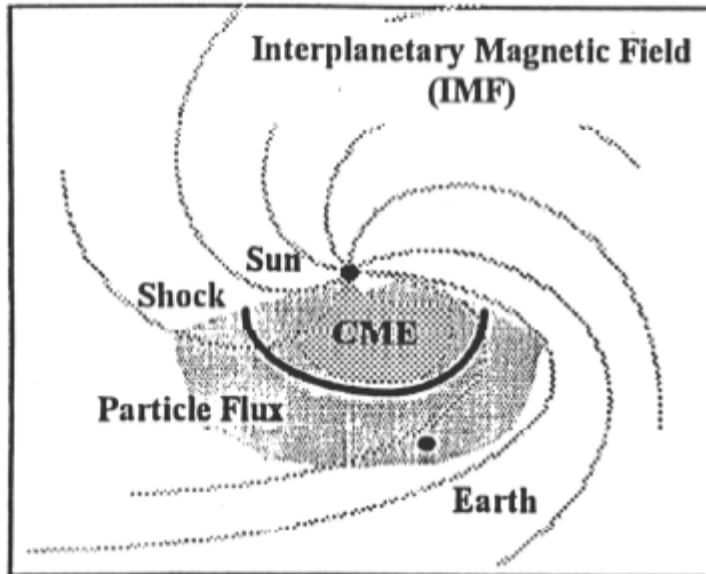
Particle Acceleration at Interplanetary Shocks

Review particle acceleration by interplanetary shocks:

- 1. Time scales for the interplanetary shock acceleration problem.*
- 2. Unsteady diffusive shock acceleration at a quasi-parallel shock.*
 - Protons*
 - Heavy ions*
- 3. Particle acceleration at quasi-perpendicular shocks.*
- 4. Modeling specific events*

Two Classes of Solar Energetic Particle Events

CME-Associated (Gradual Event)



Proton-Rich

Long-Lived (Days)

60-180 Degrees Solar Longitude

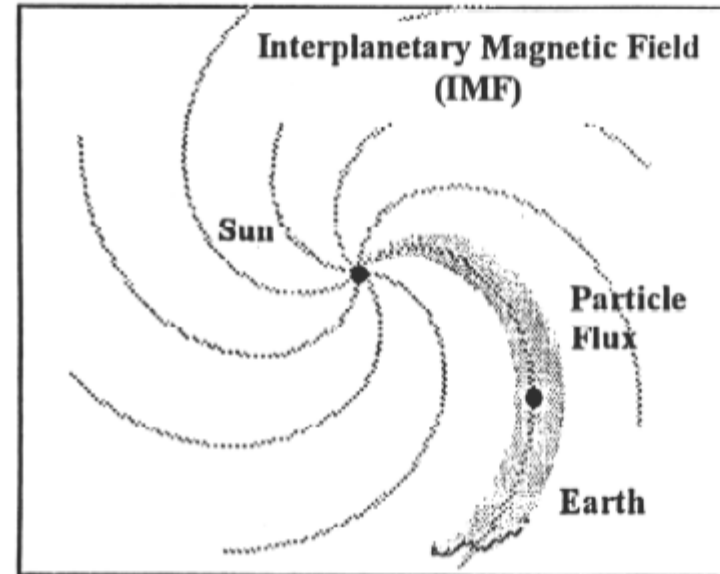
$Fe/O \approx 0.1 - 0.2$

${}^3He/{}^4He \approx .0004$

$Q(Fe) \approx 14$

Shocks accelerate solar wind

Impulsive Flare-Associated (Impulsive Event)



Electron-Rich

Short-Lived (Hours)

30-45 Degrees Solar Longitude

$Fe/O \approx 1$

${}^3He/{}^4He \approx 0.1 - 10$

$Q(Fe) \approx 20$

Heated flare material accelerated

Criteria summarized by Reames (1995)

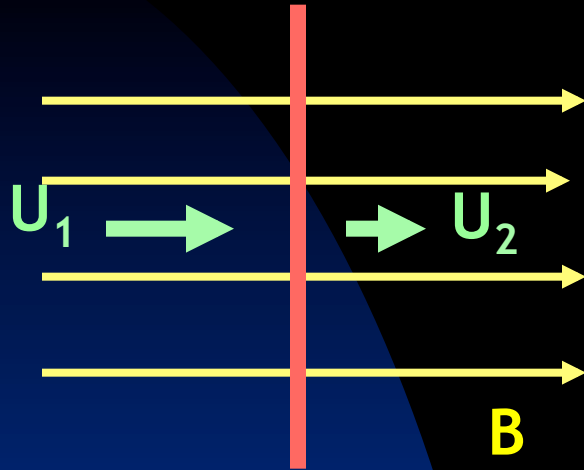
Basic diffusive shock acceleration theory

2nd-Order Fermi Acceleration: In original model of Enrico Fermi, "magnetic clouds" or "scattering centers," moving randomly, scattered particles. More "head-on" collisions than "overtaking" collisions ensures particle slowly gains energy - slow diffusive gain in energy.

1st-Order Fermi Acceleration: Suppose some agency organizes the scatterers so that, only "head-on" collisions. Energy gain faster - a *first-order* process. Shock separates high-speed and a low-speed flow, therefore scattering centers approach one another from each side of the shock. Thus, only head-on collisions. Called Diffusive Shock Acceleration.

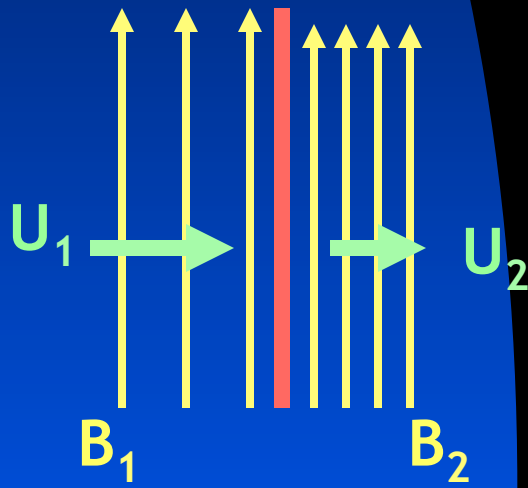
CSPAR-UAH *Basic diffusive shock acceleration theory*

Parallel shock *shock*



- Acceleration time can be very long.
- Can accelerate thermal-energy particles -- good "injectors"

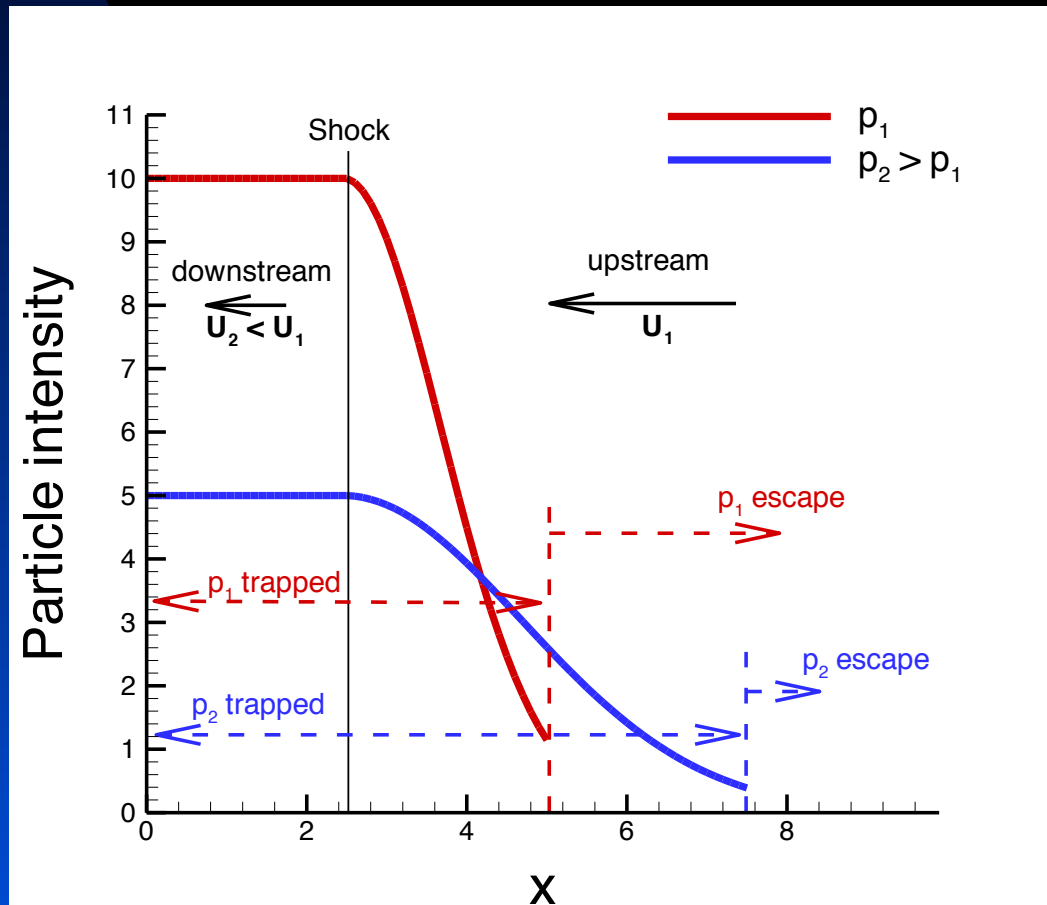
Perpendicular shock *shock*



- Acceleration time is very short compared to a parallel shock
- Cannot easily accelerate low energy particles -- poor "injectors"

Diffusive shock acceleration

- The accelerated particle intensities are constant downstream of the shock and exponentially decaying upstream of the shock.
- The scale length of the decay is determined by the momentum dependent diffusion coefficient (steady state solution).



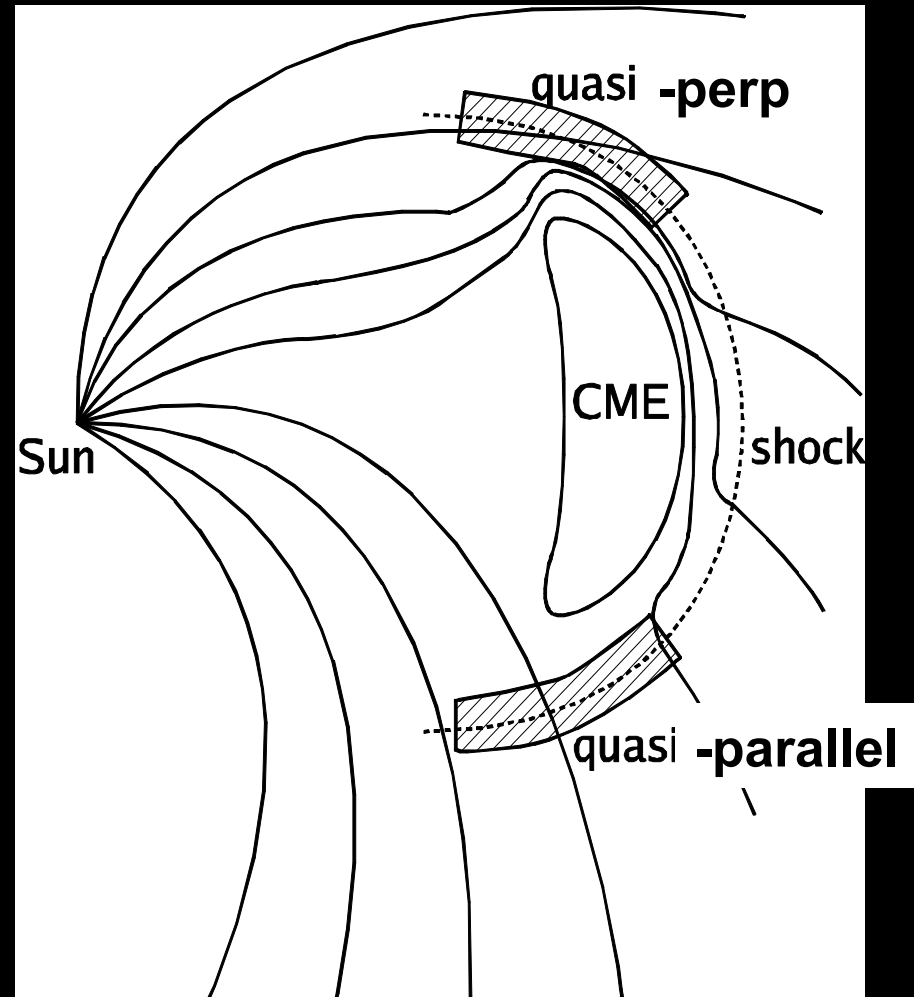
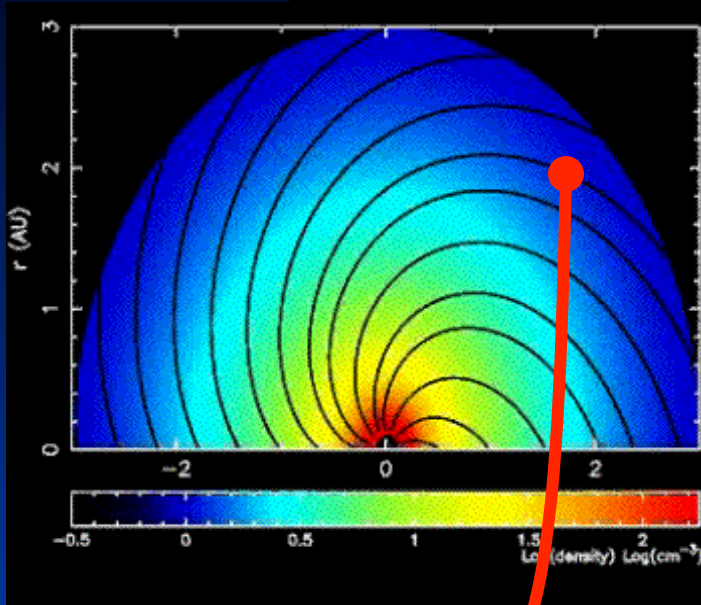
Trapped particles

- convect
- cool
- diffuse.

Escaped particles

- Transport to 1 AU (weak scattering).

Shock geometry

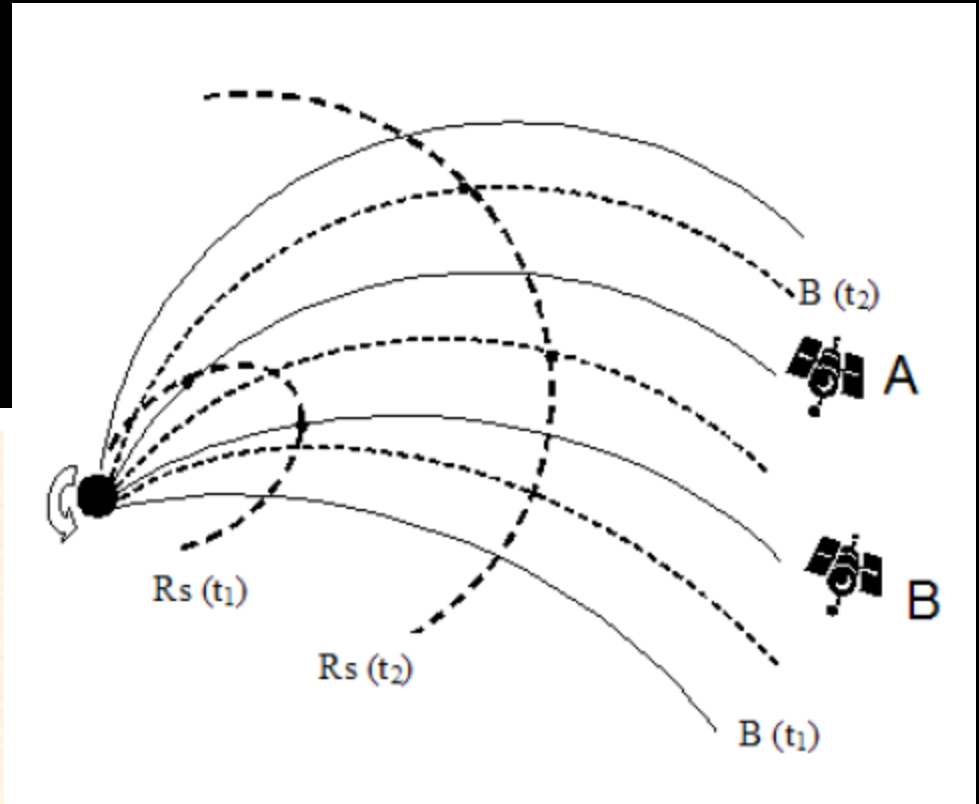
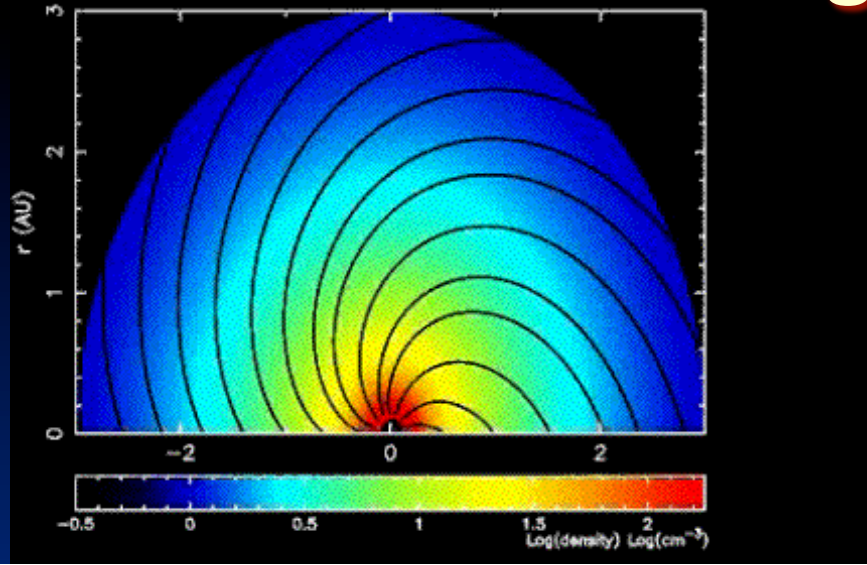


Red dot (spacecraft) connected to quasi-perpendicular shock initially and the connection gradually evolves to much more quasi-parallel configuration.

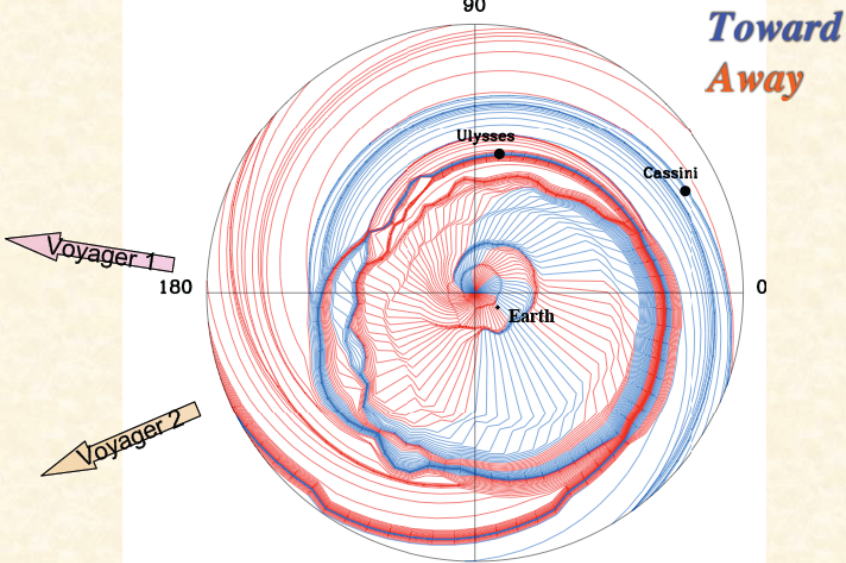
$$\tau_{convect} \sim L/U$$

$$\tau_{DYN} \sim R/dR/dt \Rightarrow \tau_{\theta} \sim \sqrt{\frac{L}{U} R/dR/dt}$$

Shock geometry



Ecliptic Plane IMF to 10 AU
00 UT, Nov 6, 2003
90



Intriligator et al., *JGR*, 2005a

Time scales for the SEP/ESP problem

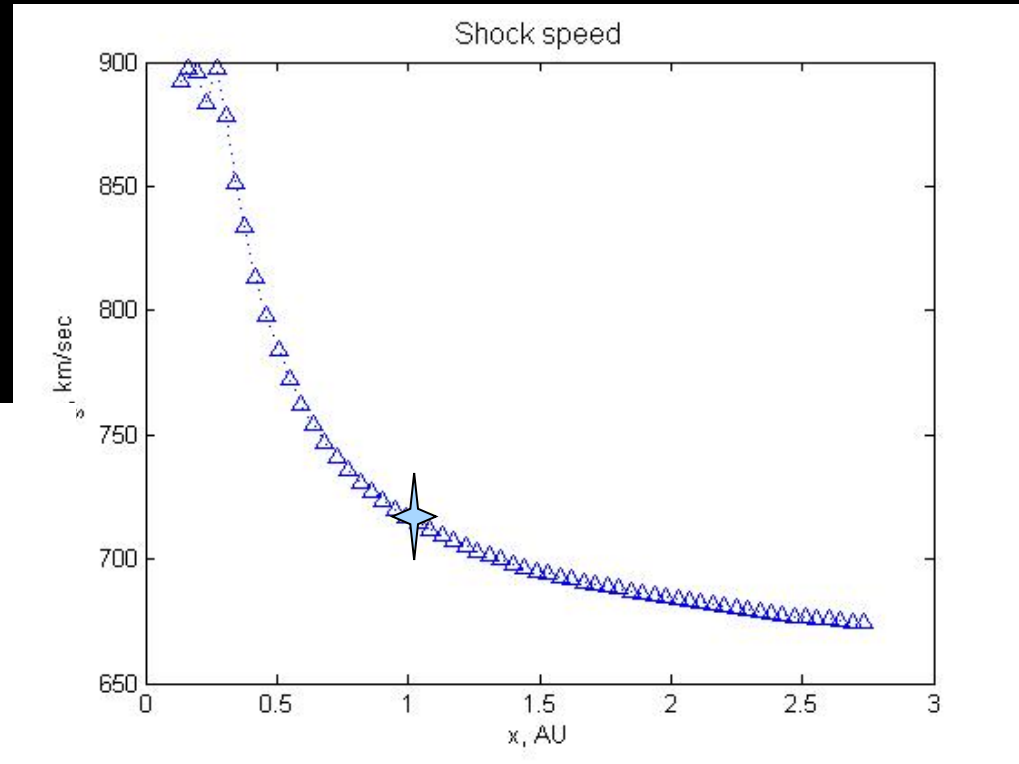
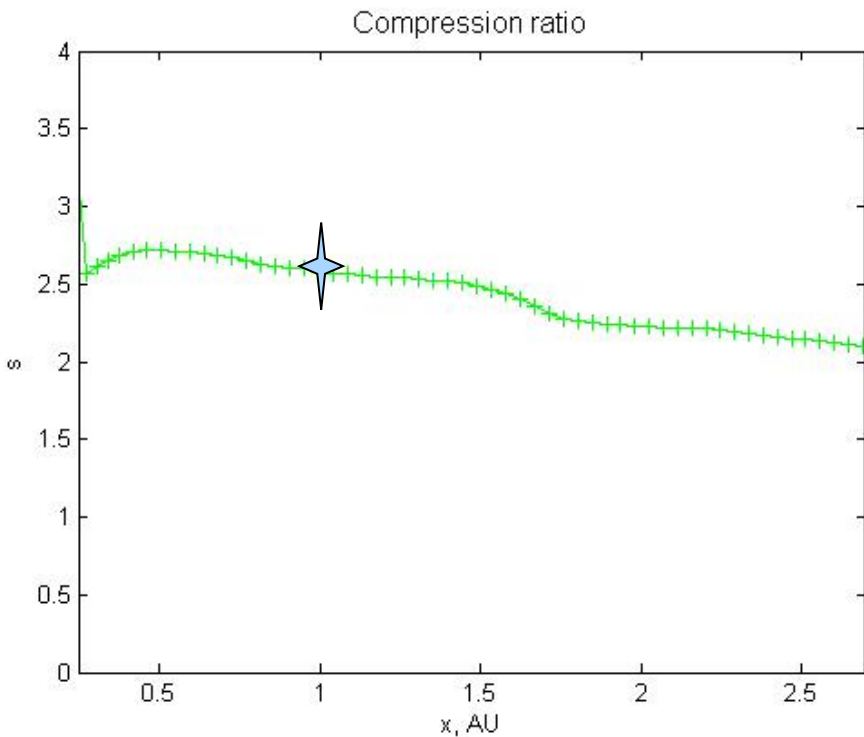
- Shock propagation in an inhomogeneous solar wind – expanding, decelerating, decreasing magnetic field strength, in situ turbulence convection, decay, driving, variability of shock normal
- Particle acceleration time scales; maximum energy, shock obliquity
- Variability in generation of shock turbulence by streaming energetic particles; particle trapping and escape
- Diffusive time scales (diffusive mfp)
- Transport time scales/length scales (transport mfp)

The shock itself introduces a multiplicity of time scales, ranging from shock propagation time scales to particle acceleration time scales at parallel and perpendicular shocks, and many of these time scales feed into other time scales (such as determining maximum particle energy scalings, escape time scales, etc.).

CSPAR-UAH

Shock position, velocity and compression ratio are computed from 0.1 AU to up to several AU.

Simulation results of the shock velocity dependence on radial distance from the Sun. The decaying shock propagates from 0.1 AU, reaching a compression ratio of about 1.8 at 1AU. The modeling was performed for 61 shells.



SEP Event # 215 (shock arrival at ACE: Sept. 29, 2001, 09:06 UT)

- Shock dynamical time scale:
- Post-shock complex time scales: Convection, adiabatic expansion
- Magnetic field change:

$$\tau_{DYNAMICAL} = \frac{R(t)}{dR/dt}$$

$$\frac{B}{B_0} = \left(\frac{R_0}{r}\right)^2 \left[1 + \left(\frac{\Omega_0 R_0}{u}\right)^2 \left(\frac{r}{R_0} - 1\right)^2 \sin^2 \theta \right]^{1/2}$$

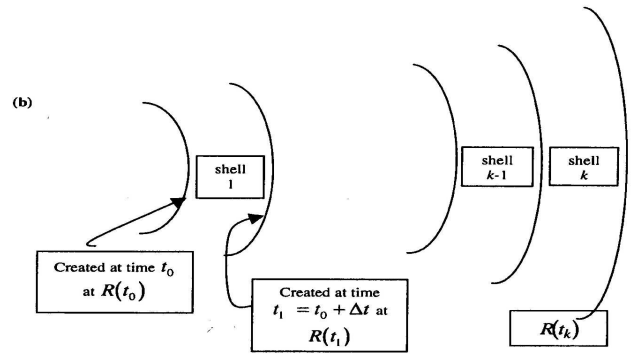
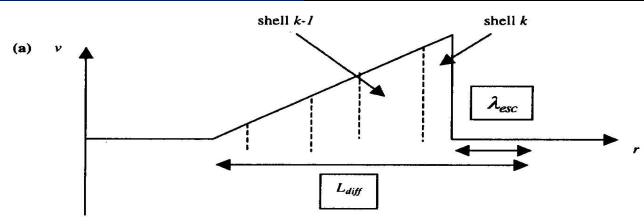


Figure 1. (a) Schematic of the density structure of an interplanetary blast wave. The total structure is subdivided into a series of concentric shells with the most recently formed shells labeled $k-1$ and k . Two length scales are identified: the escape length scale ahead of the shock front, λ_{esc} , beyond which energetic particles do not scatter diffusively back to the shock, and the scale size of the structure within which energetic ions are transported diffusively, L_{diff} . (b) A related schematic showing the concentric shells and their formation time as the shock propagates into the inhomogeneous solar wind. At time t_k the shock front is located at $R(t_k)$, which creates the edge of the outermost shell, identified as shell k . After formation the shells continue to evolve, being convected with the solar wind and expanding adiabatically.

Example:
Sedov-Taylor blast wave

$$R(t) = \left(\frac{E}{\rho}\right)^{1/5} t^{2/5}$$

$$\Rightarrow \frac{R}{dR/dt} = \frac{2}{5} t$$

- Post-shock complex time scales: Convection, adiabatic expansion, growth of post shock region and weakening of shock front.

$$\delta v(t) = \frac{\delta v_i}{\sqrt{1 + (\alpha_v \delta v_i) t}} \quad \alpha_v \equiv \frac{C_{f0}^2 + \gamma C_{sd0}^2 + 2C_{A0}^2}{2C_{f0}^2}$$

$t = t_i$

$t = t_{i+1} = t_i + \Delta t$

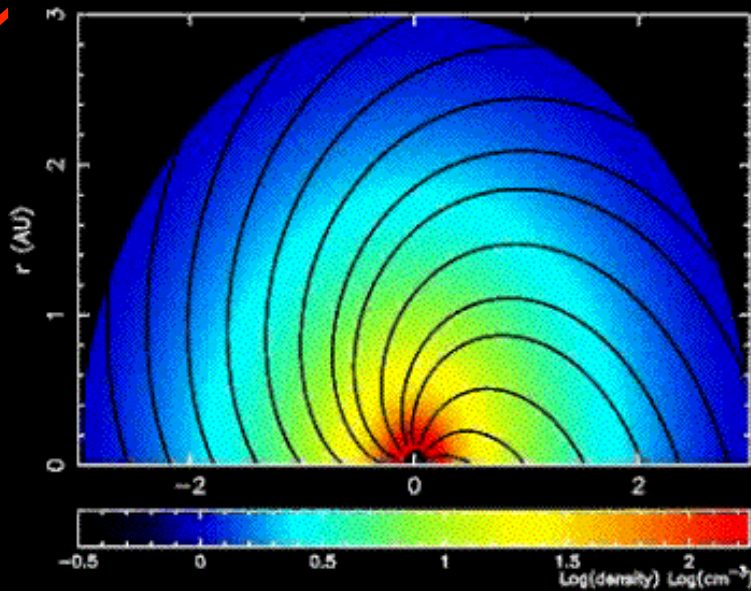
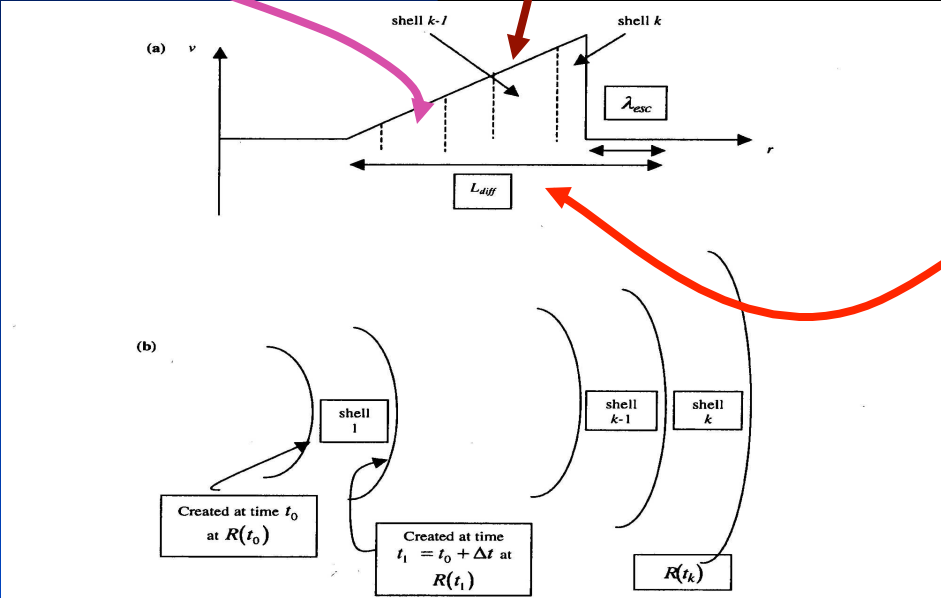
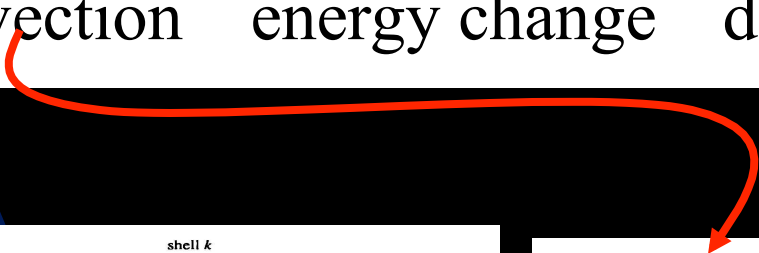


Figure 1. (a) Schematic of the density structure of an interplanetary blast wave. The total structure is subdivided into a series of concentric shells with the most recently formed shells labeled $k-1$ and k . Two length scales are identified: the escape length scale ahead of the shock front, λ_{esc} , beyond which energetic particles do not scatter diffusively back to the shock, and the scale size of the structure within which energetic ions are transported diffusively, L_{diff} . (b) A related schematic showing the concentric shells and their formation time as the shock propagates into the inhomogeneous solar wind. At time t_k the shock front is located at $R(t_k)$, which creates the edge of the outermost shell, identified as shell k . After formation the shells continue to evolve, being convected with the solar wind and expanding adiabatically.

$$\frac{\partial f}{\partial t} = -U_i \frac{\partial f}{\partial x_i} + \nabla \cdot U \frac{p}{3} \frac{\partial f}{\partial p} + \nabla \cdot (K \cdot \nabla f) + Q$$

convection
energy change
diffusion
source



$$\frac{\partial f}{\partial t} + U \frac{\partial f}{\partial r} = 0$$

$$f_i(t_k) = f_i \left[r_i(t_k) - \int_{t_{k-1}}^{t_k} U(r_i(t)) dt \right]$$

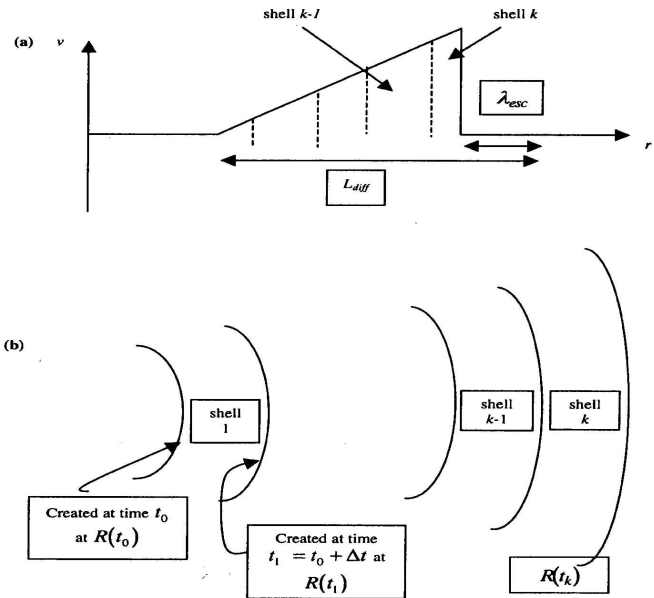


Figure 1. (a) Schematic of the density structure of an interplanetary blast wave. The total structure is subdivided into a series of concentric shells with the most recently formed shells labeled $k-1$ and k . Two length scales are identified: the escape length scale ahead of the shock front, λ_{esc} , beyond which energetic particles do not scatter diffusively back to the shock, and the scale size of the structure within which energetic ions are transported diffusively, L_{diff} . (b) A related schematic showing the concentric shells and their formation time as the shock propagates into the inhomogeneous solar wind. At time t_k the shock front is located at $R(t_k)$, which creates the edge of the outermost shell, identified as shell k . After formation the shells continue to evolve, being convected with the solar wind and expanding adiabatically.

$$\frac{\partial f}{\partial t} = \underbrace{-U_i \frac{\partial f}{\partial x_i}}_{\text{convection}} + \underbrace{+\nabla \cdot U \frac{p}{3} \frac{\partial f}{\partial p}}_{\text{energy change}} + \underbrace{+\nabla \cdot (\mathbf{K} \cdot \nabla f)}_{\text{diffusion}} + \underbrace{+Q}_{\text{source}}$$

$$\frac{\partial f}{\partial t} = \nabla \cdot U \frac{p}{3} \frac{\partial f}{\partial p}$$

$$\ln p(t_k) = \ln p(t_{k-1}) - \frac{1}{3} \int_{t_{k-1}}^{t_k} \frac{U}{r} dt - \ln \left[U(t_k) / U(t_{k-1}) \right]^{1/3}$$

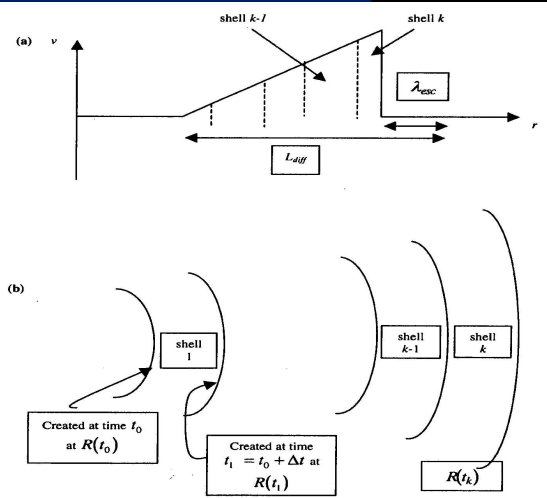


Figure 1. (a) Schematic of the density structure of an interplanetary blast wave. The total structure is subdivided into a series of concentric shells with the most recently formed shells labeled $k-1$ and k . Two length scales are identified: the escape length scale ahead of the shock front, λ_{esc} , beyond which energetic particles do not scatter diffusively back to the shock, and the scale size of the structure within which energetic ions are transported diffusively, L_{diff} . (b) A related schematic showing the concentric shells and their formation time as the shock propagates into the inhomogeneous solar wind. At time t_k the shock front is located at $R(t_k)$, which creates the edge of the outermost shell, identified as shell k . After formation the shells continue to evolve, being convected with the solar wind and expanding adiabatically.

$$\frac{\partial f}{\partial t} = \underbrace{-U_i \frac{\partial f}{\partial x_i}}_{\text{convection}} + \underbrace{+\nabla \cdot U \frac{p}{3} \frac{\partial f}{\partial p}}_{\text{energy change}} + \underbrace{+\nabla \cdot (\mathbf{K} \cdot \nabla f)}_{\text{diffusion}} + \underbrace{+Q}_{\text{source}}$$

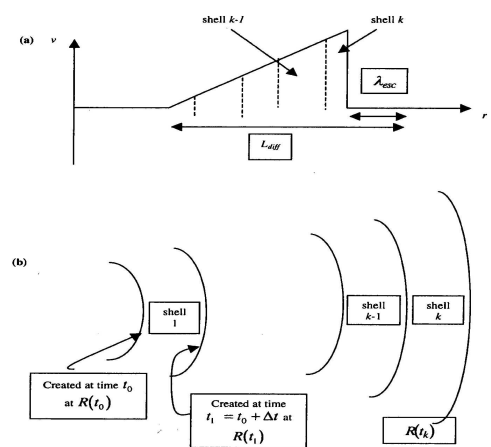
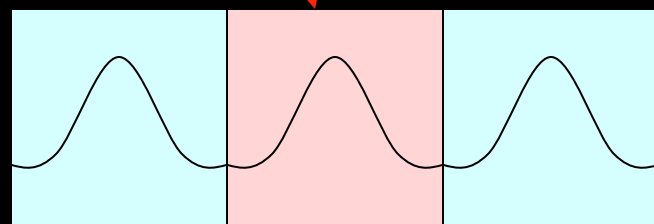


Figure 1. (a) Schematic of the density structure of an interplanetary blast wave. The total structure is subdivided into a series of concentric shells with the most recently formed shells labeled $k-1$ and k . Two length scales are identified: the escape length scale ahead of the shock front, λ_{esc} , beyond which energetic particles do not scatter diffusively back to the shock, and the scale size of the structure within which energetic ions are transported diffusively, L_{diff} . (b) A related schematic showing the concentric shells and their formation time as the shock propagates into the inhomogeneous solar wind. At time t_k the shock front is located at $R(t_k)$, which creates the edge of the outermost shell, identified as shell k . After formation the shells continue to evolve, being convected with the solar wind and expanding adiabatically.

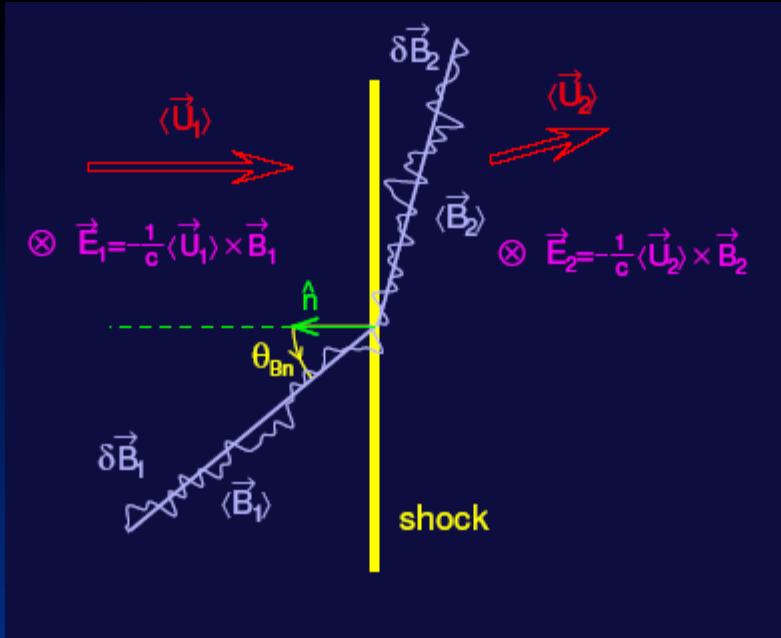
JGR, Zank et al. Vol. 105 p 25,079-25,095



$$\frac{\partial f}{\partial t} = \frac{1}{r^2} \frac{\partial}{\partial r} \left(r^2 K \frac{\partial f}{\partial r} \right)$$

$$f_i(t_k, p, r) = \frac{1}{\sqrt{\pi}} \frac{f_i^n(t_{k-1}, p)}{4\pi r_i^2(t_k)} \frac{1}{\sqrt{4K(t_k - t_{k-1}) + (\kappa/U_1)^2}} \exp \left[\frac{(r - r_i(t_k))^2}{4K(t_k - t_{k-1}) + (\kappa/U_1)^2} \right]$$

Particle acceleration time scales



$$\frac{\Delta p}{p} = \frac{U_1 - U_2}{3} \frac{\Delta t}{L}$$

$$L = \frac{\kappa}{U_1}$$

$$\Rightarrow \Delta t = \frac{3U_1}{U_1 - U_2} \frac{\kappa}{U_1^2} \frac{\Delta p}{p} = \frac{3s}{s-1} \frac{\kappa}{U_1^2} \frac{\Delta p}{p}$$

U and κ_{xx} change discontinuously across the shock

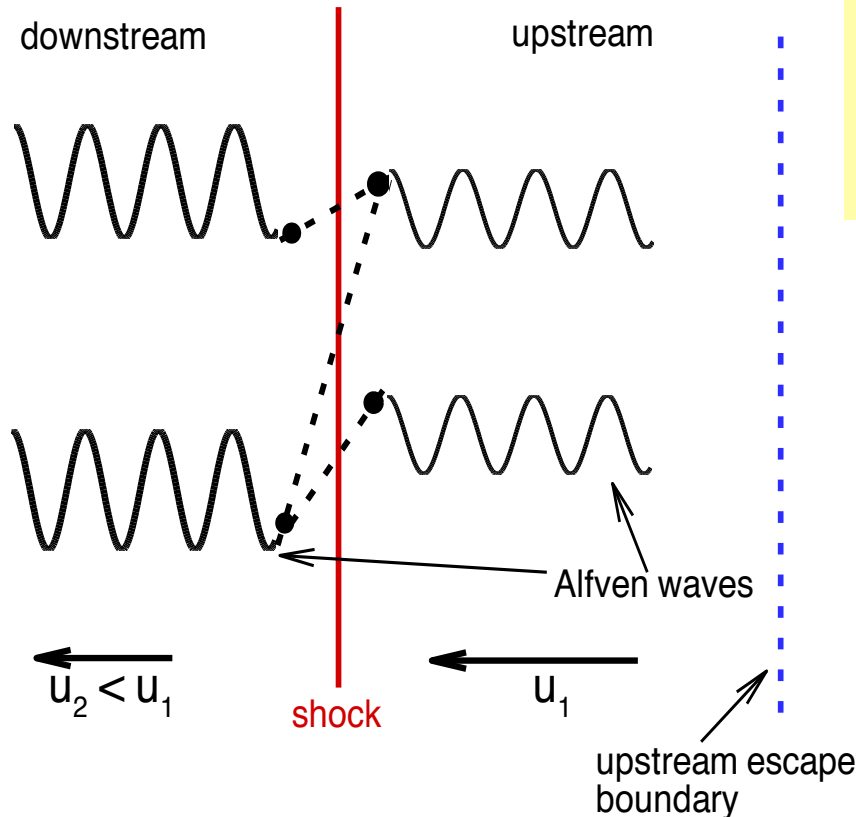
$$\tau_{acc} = p \frac{\Delta p}{p} = \frac{3s(t)}{s(t)-1} \frac{\kappa(t, p, r)}{U_1^2}$$

Maximum particle energy

- The maximum particle energy can be determined by equating the dynamic timescale of the shock with the acceleration timescale (Drury, 1983; Zank et al., 2000).

$$\frac{R(t)}{(dR/dt)} = \frac{3s}{s-1} \int_{p_{inj}}^{p_{max}} \frac{\kappa(t, p', r)}{U_1^2} d(\ln p')$$

Diffusion coefficient at parallel shock



Near the shock front, Alfvén waves are responsible for particle scattering. The particle distribution f , and wave energy density A are coupled together through:

$$\frac{\partial A}{\partial t} + u \frac{\partial A}{\partial r} = \Gamma A - \gamma A,$$

$$\frac{\partial f}{\partial t} + u \frac{\partial f}{\partial r} - \frac{p}{3} \frac{\partial u}{\partial r} \frac{\partial f}{\partial p} = \frac{\partial}{\partial r} \left(\kappa \frac{\partial f}{\partial r} \right),$$

$$\kappa(p) = \frac{\kappa_0 B_0}{A(k) B} \frac{(p/p_0)^2}{\sqrt{(m_p c/p_0)^2 + (p/p_0)^2}},$$

$$\kappa_0 = \frac{4}{3\pi} r_{p0} c = \frac{4}{3\pi} \frac{p_0 c}{e B_0},$$

Gordon et al., 1999 used to evaluate wave intensity. P_{max} , N_{inj} , p_{inj} , s , etc. Bohm limited applied when wave energy density per log bandwidth exceeds local solar wind magnetic energy density.

Maximum particle energy at quasi-parallel shock:

$$\frac{R(t)}{\dot{R}(t)} \approx \frac{q(t)}{u_1^2} \int_{p_{inj}}^{p_{max}} \kappa(p') d(\ln(p')) = \frac{q(t)}{\dot{R}^2(t)} \left(\frac{5M^2(t)+3}{M^2(t)+3} \right) \int_{p_{inj}}^{p_{max}} \kappa(p') d(\ln(p'))$$

Age

Strength

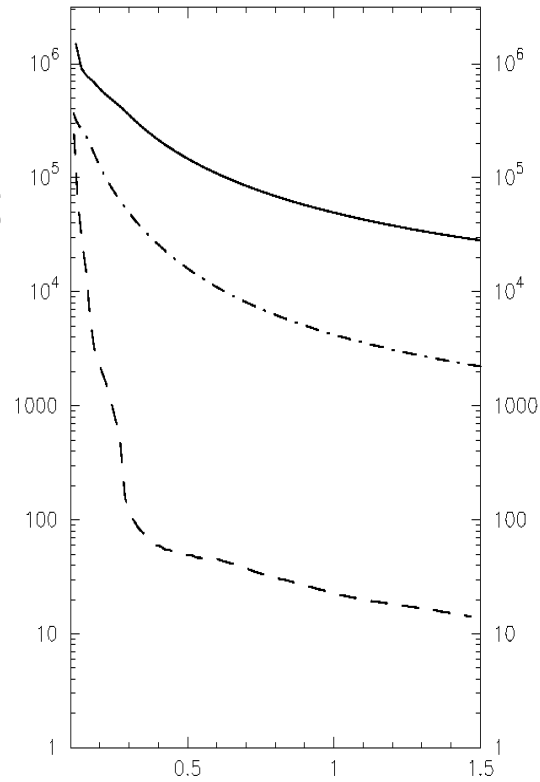
Magnetic field heliocentric dependence

$$p_{max} = \left\{ \left[\frac{M^2(t)+3}{5M^2(t)+3} \frac{R(t)\dot{R}(t)}{q(t)\kappa_0} \frac{B}{B_0} + \sqrt{\left(\frac{m_p c}{p_0}\right)^2 + \left(\frac{p_{inj}}{p_0}\right)^2} \right]^2 - \left(\frac{m_p c}{p_0}\right)^2 \right\}^{1/2}$$

$$\frac{B}{B_0} = \left(\frac{R_0}{r}\right)^2 \left[1 + \left(\frac{\Omega_0 R_0}{u}\right)^2 \left(\frac{r}{R_0} - 1\right)^2 \sin^2 \theta \right]^{1/2}$$

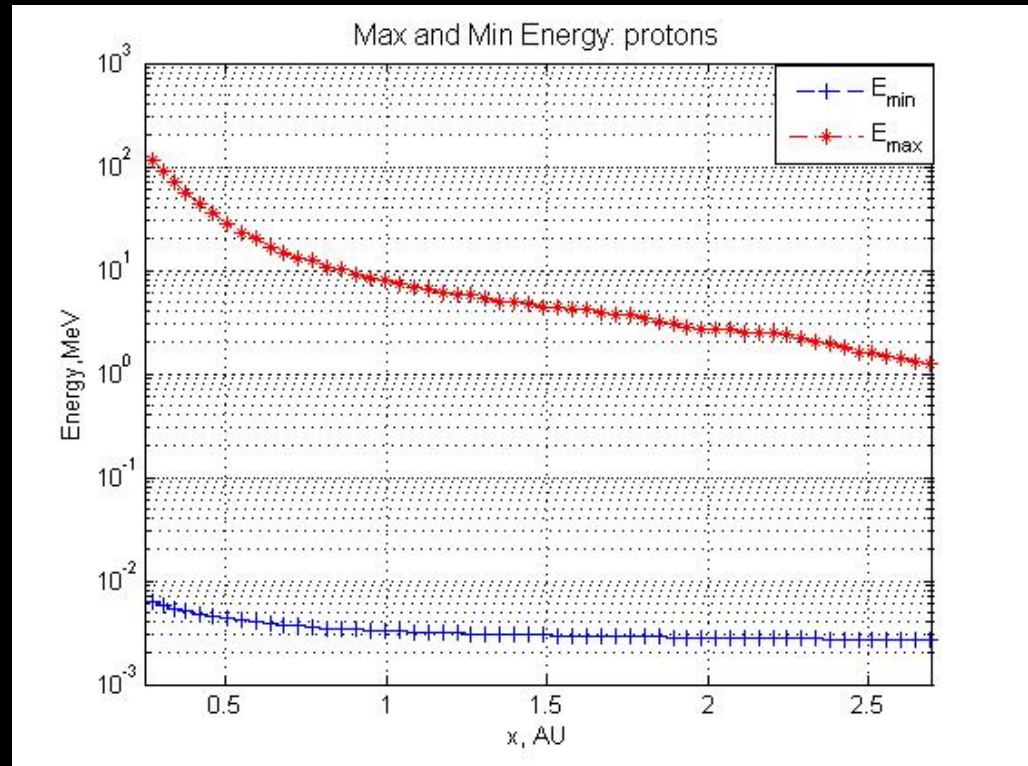
CSPAR-UAH *Maximum energies for protons*

Maximum energy keV



r (AU)

Strong, medium, weak
shock examples



SEP Event # 215 (shock arrival at
ACE: Sept. 29, 2001, 09:06 UT)

The maximum particle momentum obtained for a strong shock at early times can be as high as a few GeV - consistent with observations by Kahler [1994].

- What happens to the turbulence excited by the streaming protons?
- For quasi- \parallel shocks, turbulence excited by usual streaming instability; amplified on shock transmission
- Shell picture nice for describing the evolution of turbulence in downstream region – simplest is to assume WKB description as shell is convected outward and expands or to include turbulent dissipation.

CSPAR-UAH

Need to solve at the shock:
$$\frac{\partial f}{\partial t} + u \frac{\partial f}{\partial r} - \nabla \cdot u \frac{p}{3} \frac{\partial f}{\partial p} = \frac{\partial}{\partial r} \left(\kappa_{rr} \frac{\partial f}{\partial r} \right) + Q$$

Local shock accelerated distribution:

Local maximum energy

$$f(t_k; t_k, p) = \frac{Q(t_k) \eta R^2(t_k)}{p_0^3} \frac{3 - q(t_k)}{\left[\frac{p_{\max}(t_k)}{p_{inj}(t_k)} \right]^{3 - q(t_k)} - 1} \left(\frac{p_0}{p_{inj}(t_k)} \right)^{3 - q(t_k)} \left(\frac{p}{p_0} \right)^{-q(t_k)} \times \left\{ H(p - p_{inj}(t_k)) - H(p - p_{\max}(t_k)) \right\}$$

Injection rate per unit area

Area of shock wave

Injection momentum

$$q(t_i) = 3r_i / (r_i - 1)$$

Spatial injection flux (particles per unit time):

$$\bar{Q}(p, t) = n_{inj} \frac{\delta(p - p_{inj})}{4\pi p^2} \dot{R}(t)$$

$$Q(t) = 4\pi \int \bar{Q}(p, t) p^2 dp = n_{inj} \dot{R}(t)$$

$$4\pi R^2(t) \int \bar{Q}(p, t) d^3 p = 4\pi R^2(t) \dot{R} n_{inj} = \begin{cases} \sim t^2 \text{ (Sweep-up phase)} \\ \sim t^{1/5} \text{ (Sedov phase)} \end{cases}$$

$$n_{inj} = \delta \cdot n_1 \propto (r)^{-2}$$

$$r = Ut$$

$$\Rightarrow \begin{aligned} \text{Sweep up } (\dot{R}_{SW} = \text{const}) &\sim \text{const.} \\ \text{Sedov-Taylor } (R \propto t^{3/5}) &\sim t^{-9/5} \end{aligned}$$

Young interplanetary shocks which have not yet experienced any significant deceleration inject and accelerate particles far more efficiently than do older shocks which are in a decaying phase.

Particle Transport

Particle transport obeys Boltzmann(Vlasov) equation:

$$\frac{df(x,p,t)}{dt} + q[E + \mathbf{v} \times B] \cdot \frac{\partial f(x,p,t)}{\partial p} = \frac{df(x,p,t)}{dt} \Big|_{coll}$$

The LHS contains the material derivative and the RHS describes various “collision” processes.

- Collision in this context is pitch angle scattering caused by the irregularities of IMF and in quasi-linear theory

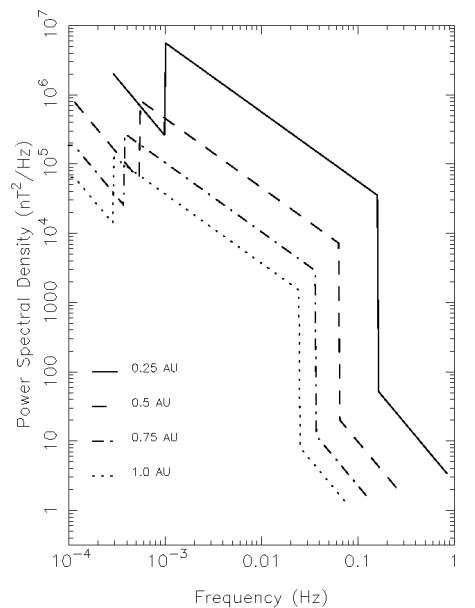
$$\frac{df}{dt} = \frac{\partial}{\partial \mu} \left(D_{\mu\mu} \frac{\partial f}{\partial \mu} \right)$$

- The result of the parallel mean free path $\lambda_{//}$, from a simple QLT is off by an order of magnitude from that inferred from observations, leading to a 2-D slab model.

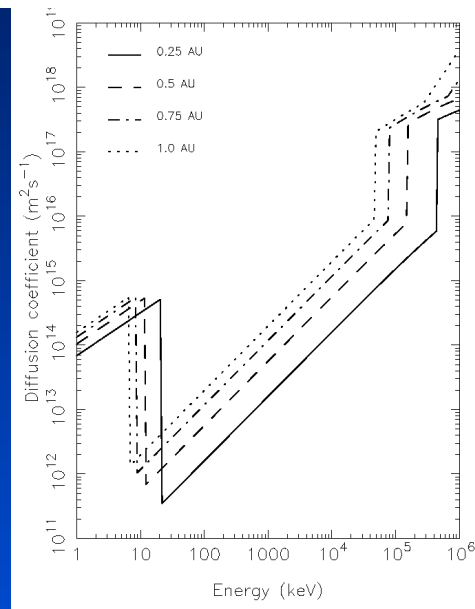
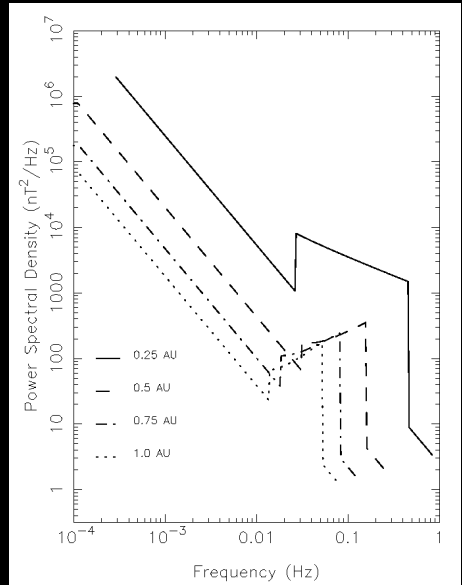
$$\frac{\lambda}{10^6 \text{ km}} = 8.30 \frac{(B/B_0)^2}{\delta B_x^2 / \delta B_{x0}^2} \left(\frac{l}{l_0} \right)^{2/3} \left(\frac{p/M_n}{B/B_0} \right)^{1/3}$$

Allows a Monte-Carlo technique.

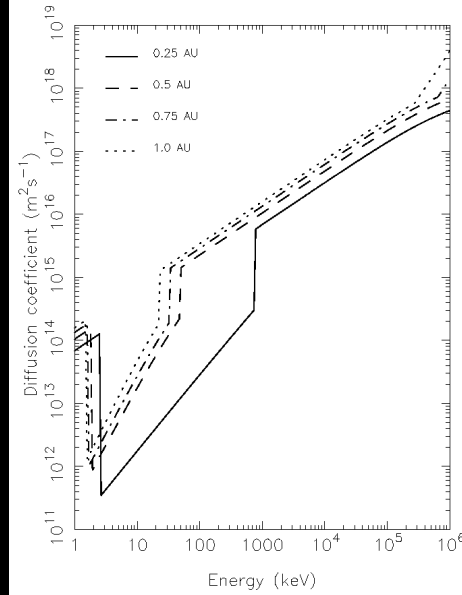
Wave spectra and diffusion coefficient at shock



Wave intensity



Diffusion coefficient

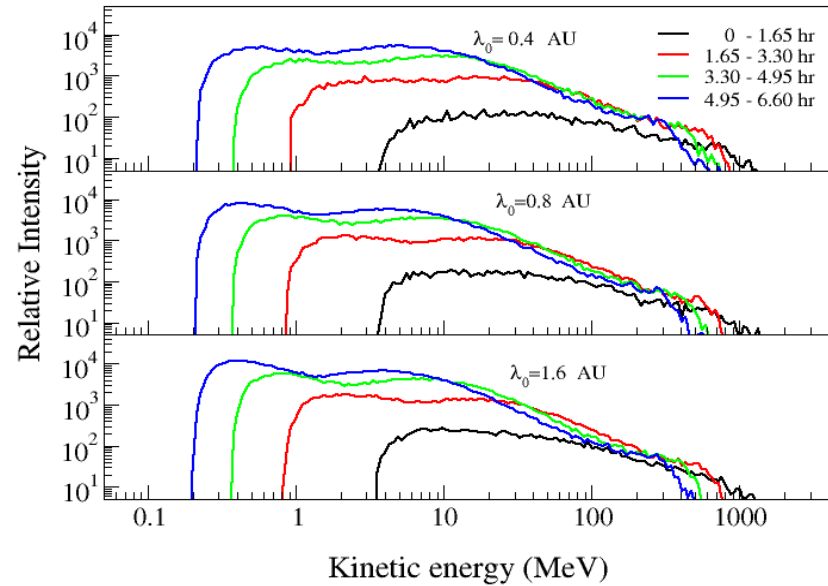
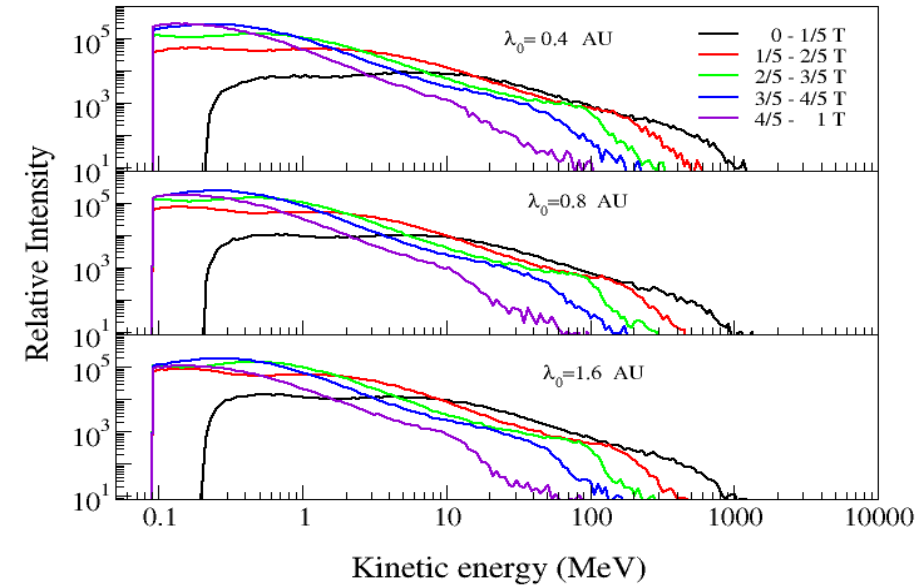


Strong shock

Weak shock

CSPAR-UAH *Upstream particle spectrum (strong shock)*

Early time

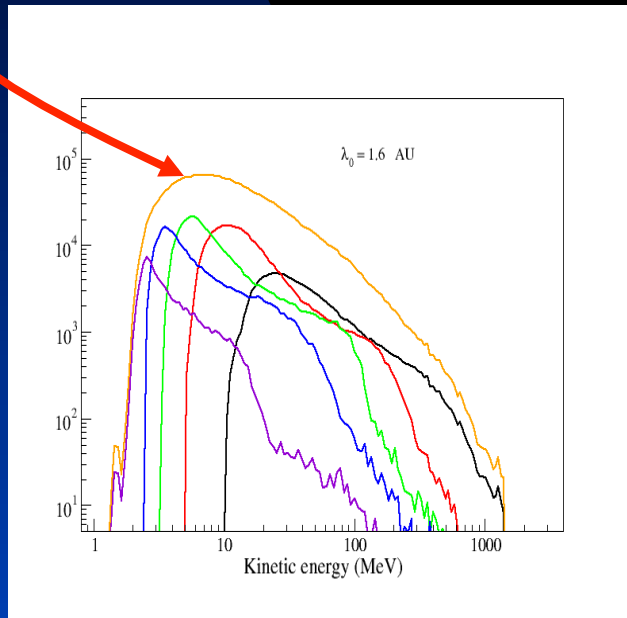


- Cumulative spectra at 1 AU for five time intervals are shown, $T=1.3$ days.
- Spectra exhibit a power law feature.
- Broken power law at later times, especially for larger mfp ($\lambda_0 = 1.6$ AU). E.g., $K=20$ MeV for the time interval $t = 4/5-1$ T - particle acceleration no longer to these energies.

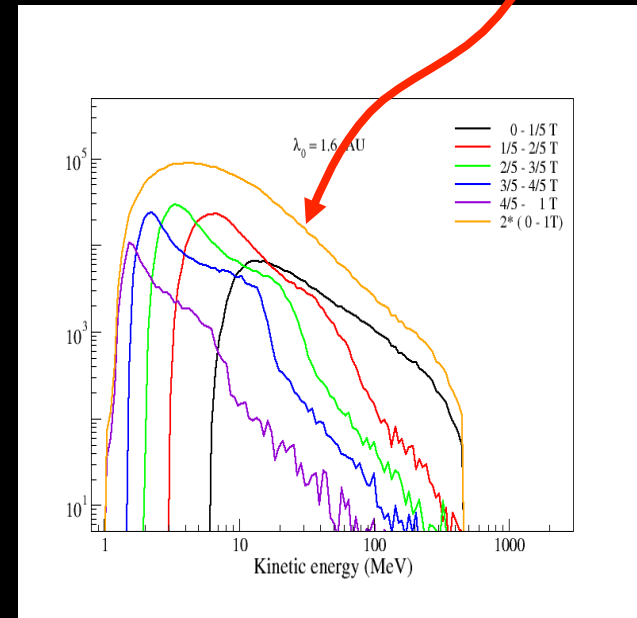
Event Integrated spectra

Total or cumulative spectrum at 1AU, integrated over the time from shock initiation to the arrival of the shock at 1AU.

Strong shock case



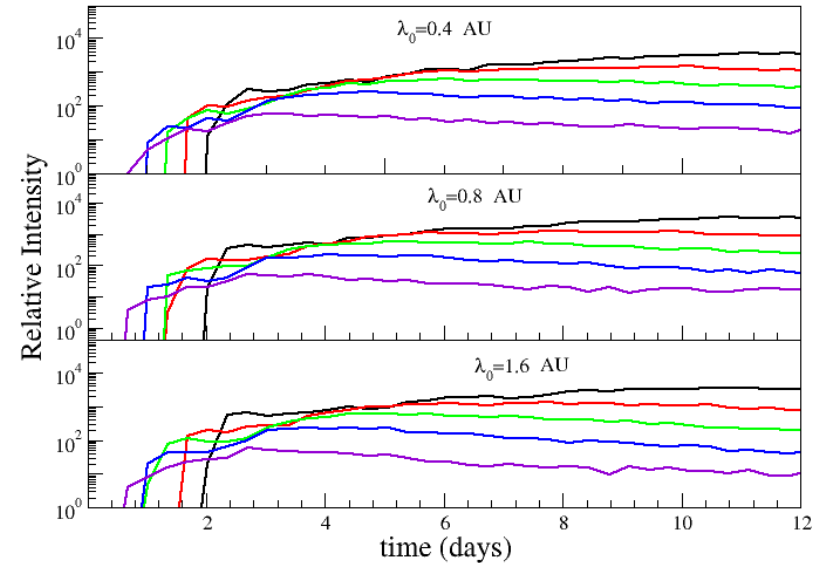
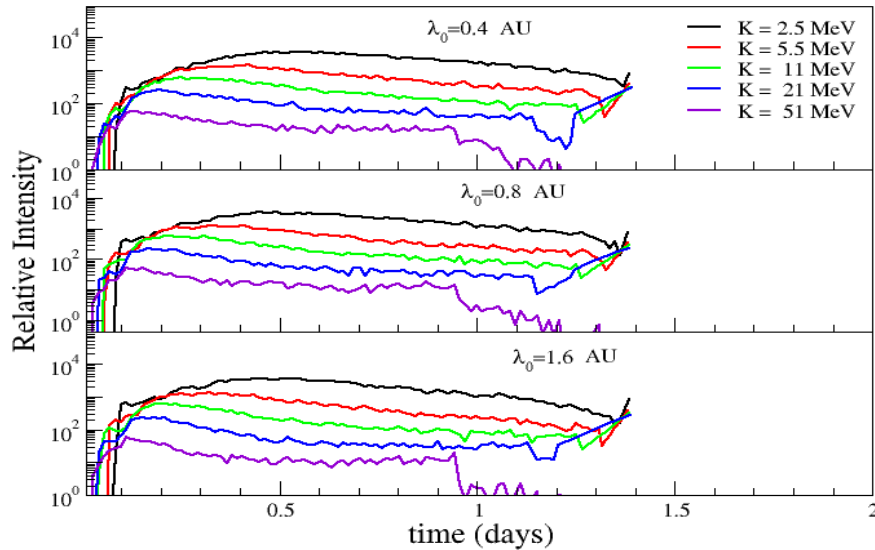
Weak shock case



Note the relatively pronounced roll-over in the cumulative strong shock spectrum and the rather flat power-law spectrum in the weak shock case.

Intensity profile (strong shock)

Early time



- Shock arrives 1.3 days after initiation
- No ~ 50 MeV particles at shock by 1 AU since shock weakens and unable to accelerate particles to this energy and trapped particles have now escaped.
- A slowly decreasing plateau feature present - result of both pitch angle scattering and shock propagation.
- Early time profile shows the brief free streaming phase.

CSPAR-UAT *Time evolution of number density in phase space*

Snap shots of the number density observed at 1 AU prior to the shock arrival at $t = 1/20, 2/20, \dots T$, with a time interval of $1/20 T$ in $(v_{\text{par}}, v_{\text{perp}})$ -space.

• Coordinates: $Z_x = \cos(\theta_{\hat{\mathbf{B}}, \hat{\mathbf{p}}})(\log(p/\text{MeV}) - 4.25);$
 $Z_y = \sin(\theta_{\hat{\mathbf{B}}, \hat{\mathbf{p}}})(\log(p/\text{MeV}) - 4.25).$

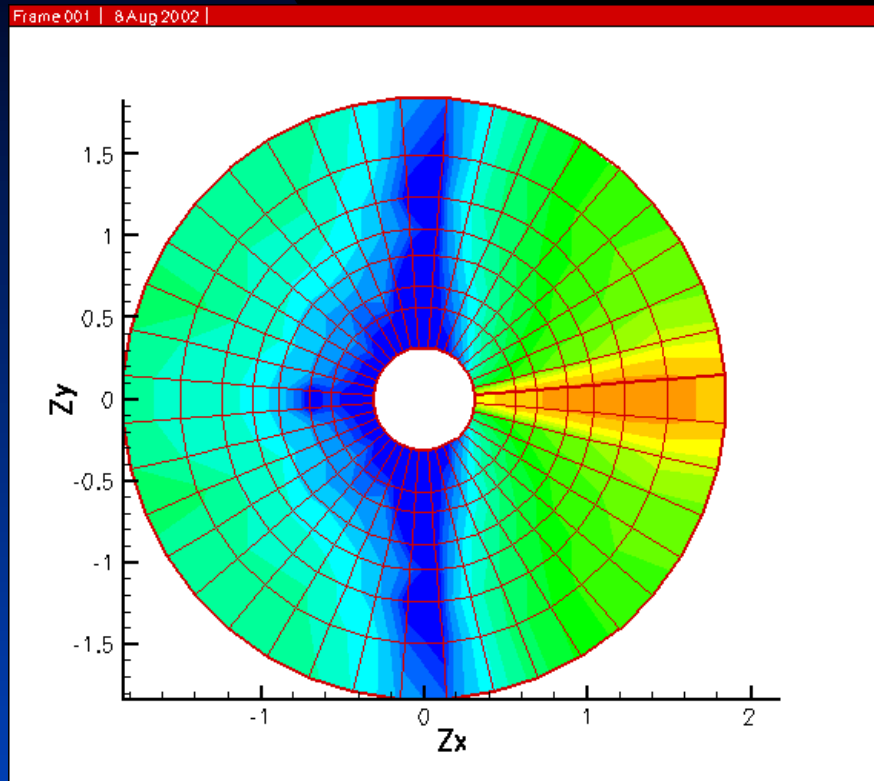
- B field along positive Z_x direction
- Particle energies from innermost to outermost circle are $K = 4.88, 8.12, 10.47, 15.35, 21.06, 30.75, 50.80, 100.13$ MeV respectively.

The next figures exhibit the following characteristics:

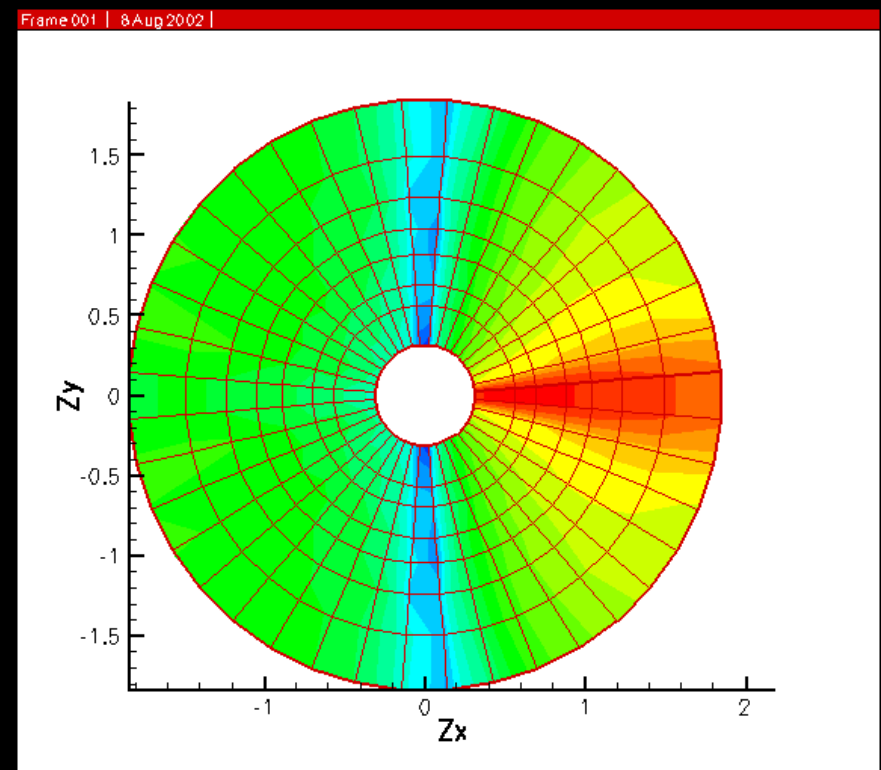
- At early times, more high energy particles cross 1 AU along +B direction, followed by lower energies later.
- Number density of higher energy particles at later times exhibits a “reverse propagation” feature corresponding to $A < 0$.
- The gap at $\Theta = 90$ degree reflects that particles must have a component along B to be observed.

Phase space evolution

Strong shock

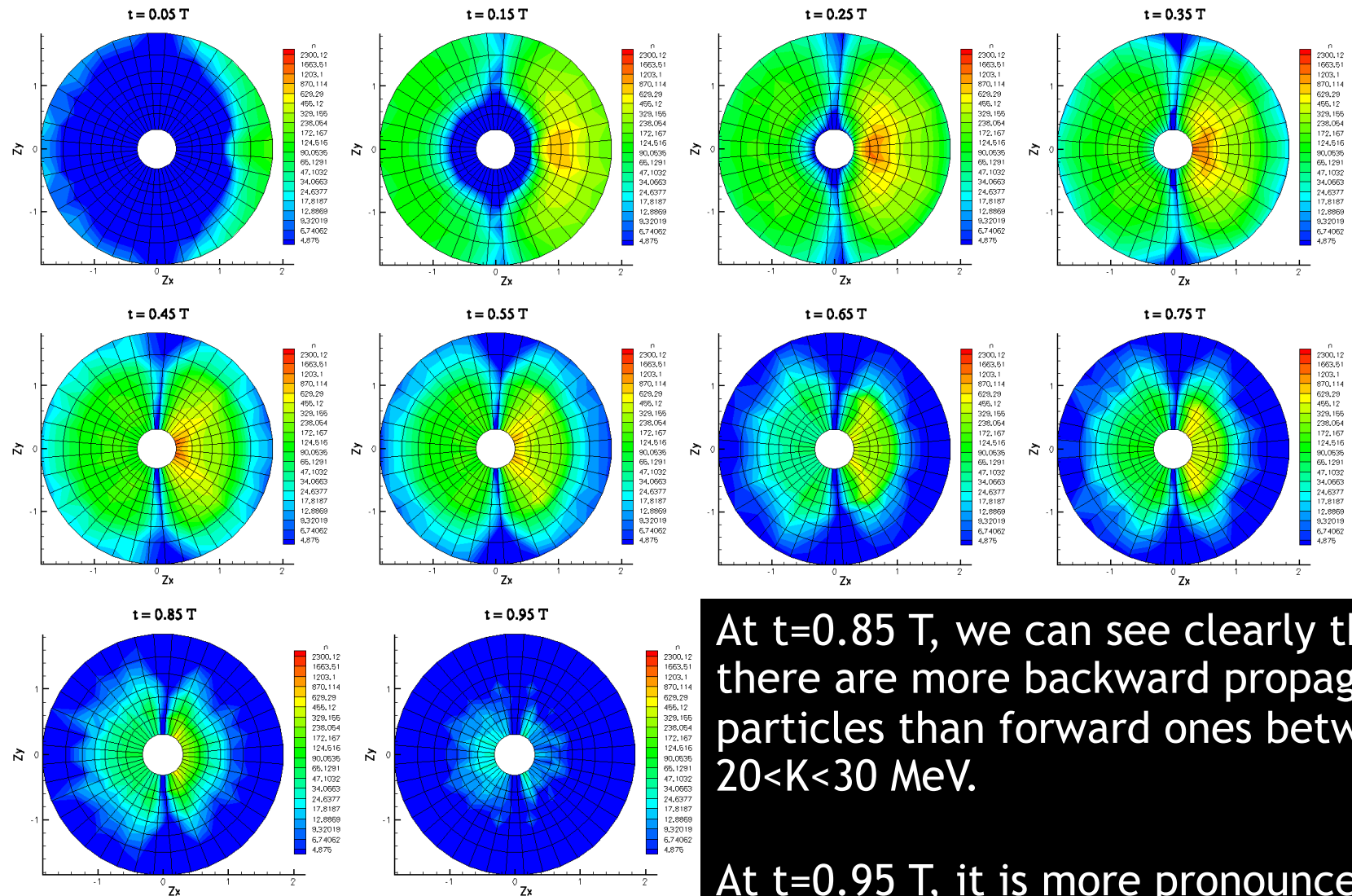


Weak shock



CSPAR-UAH

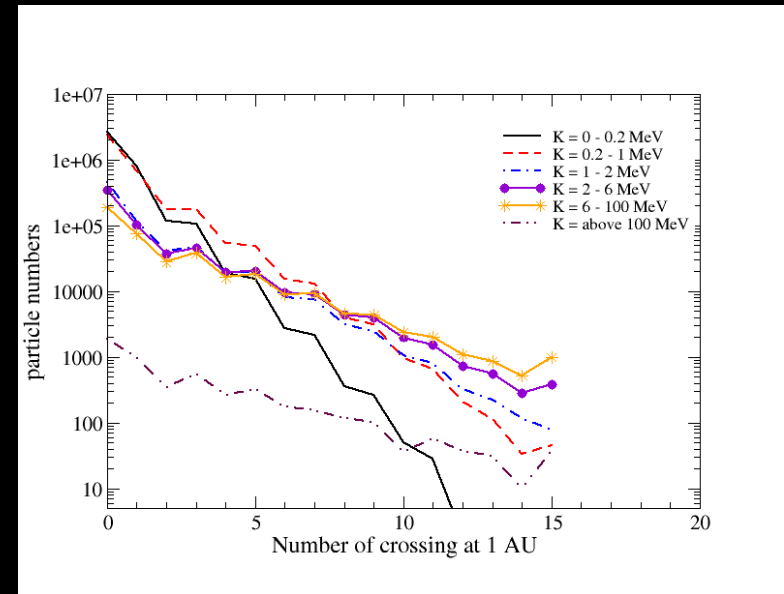
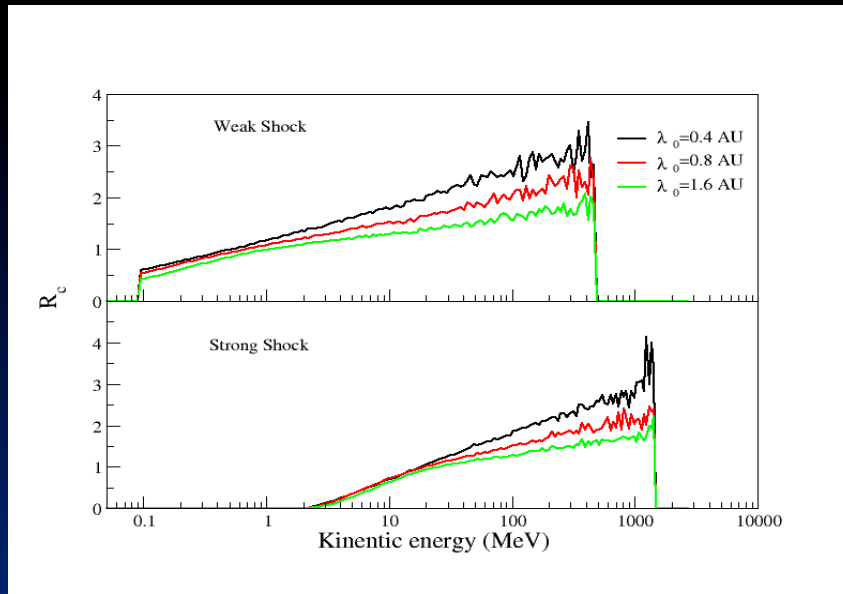
Phase space evolution - time sequence



At $t=0.85 T$, we can see clearly that there are more backward propagating particles than forward ones between $20 < K < 30$ MeV.

At $t=0.95 T$, it is more pronounced for $K \sim 10$ MeV.

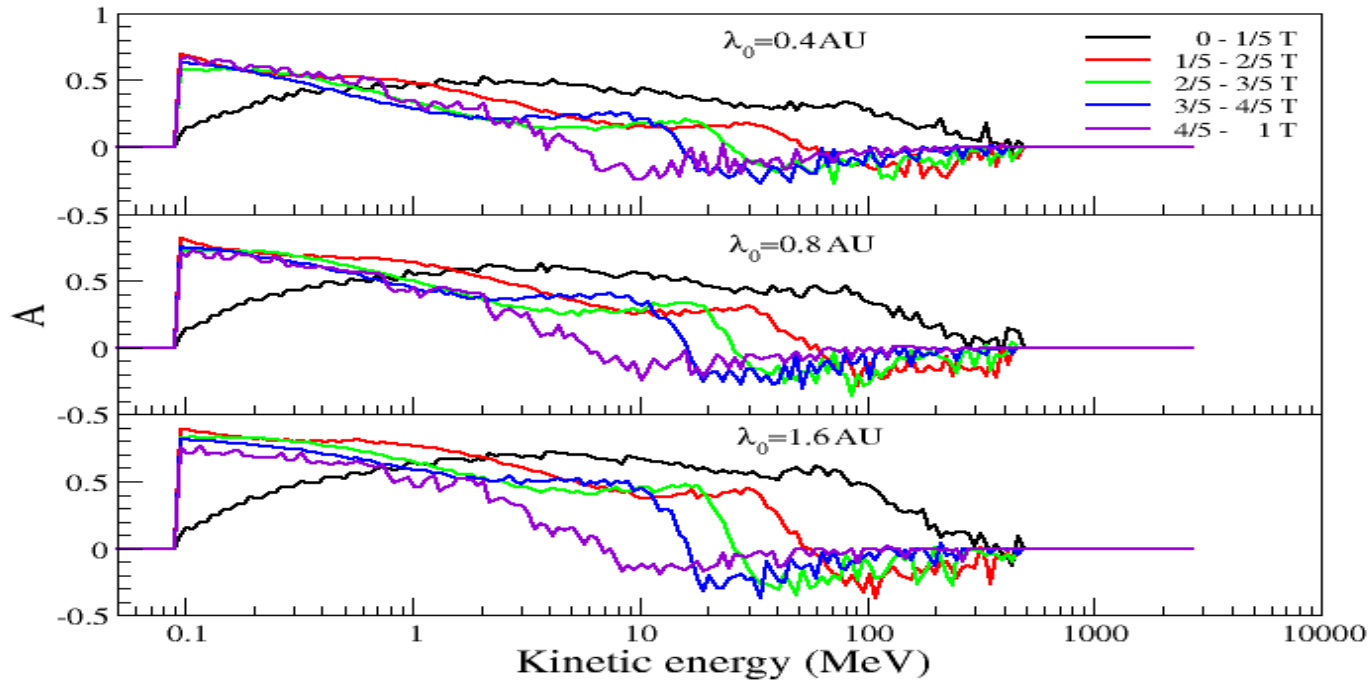
Multiple particle crossings at 1AU



$$R_c(K) \equiv \frac{\text{number of particles of energy } K \text{ that cross 1 AU}}{\text{number of particles of energy } K \text{ that leave the shock}}$$

Due to pitch angle scattering, particles, especially of high energies, may cross 1 AU more than once, and thus from both sides. In an average sense, a 100 MeV particle has $R_c \sim 2$, or on average, two crossings. Histogram shows that some particles may cross as many as 15 times. A smaller mfp leads to a larger R_c since particles with smaller mfp will experience more pitch angle scatterings.

CSPAR-UAH *Anisotropy at 1 AU (weak shock)*

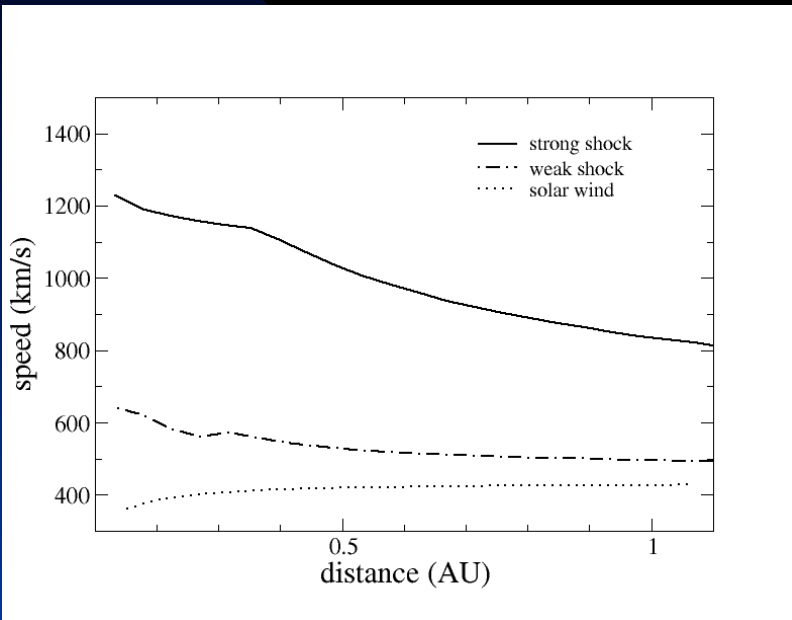


- Similar to the strong shock case.
- The value of asymmetry for larger λ_0 is consistently larger than that of a smaller λ_0 because fewer particles will propagate backward for a larger λ_0 .

HEAVY IONS (CNO and Fe)

CNO: $Q = 6$, $A = 14$

Fe: $Q = 16$, $A = 54$



Shock speeds for strong and a weak shock.

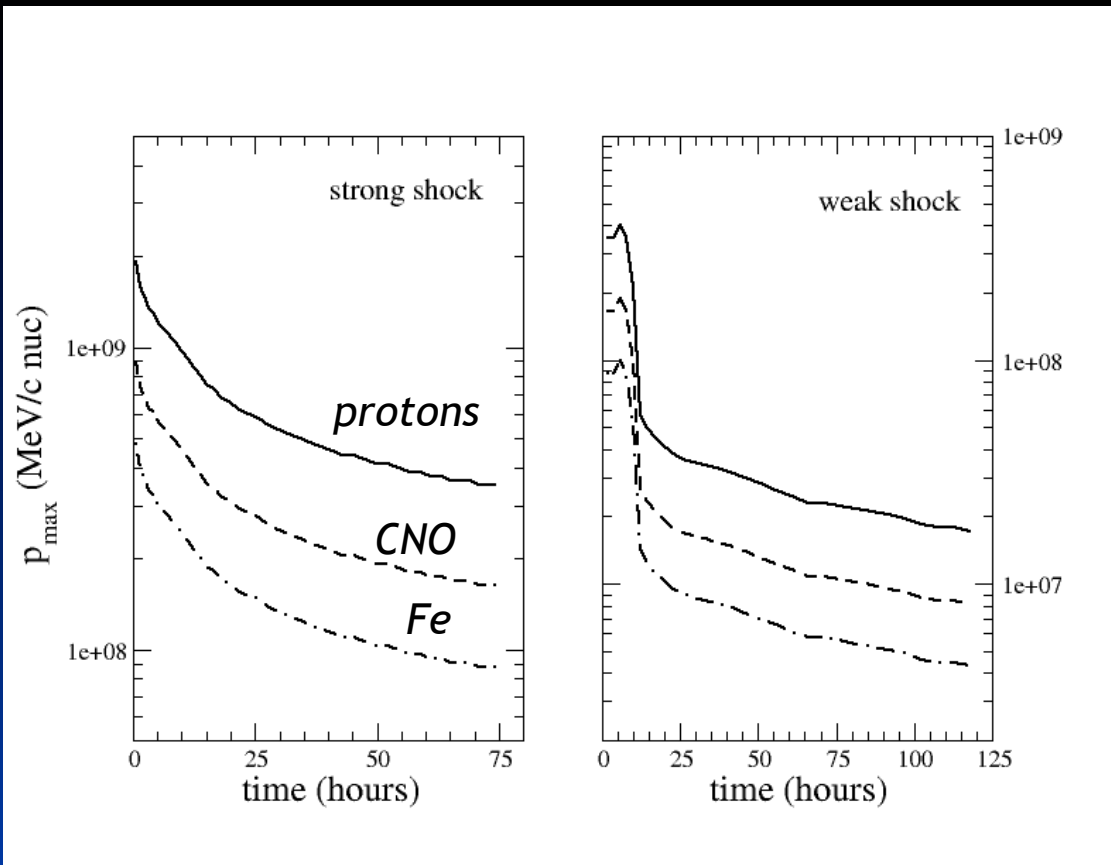
Effect of heavy ions is manifested through the resonance condition, which then determines maximum energies for different mass ions and it determines particle transport - both factors that distinguish heavy ion acceleration and transport from the proton counterpart.

$$k = \frac{\gamma m_p \Omega}{\mu p}$$

$$\Omega = \frac{(Q/A) e B}{\gamma m_p c}$$

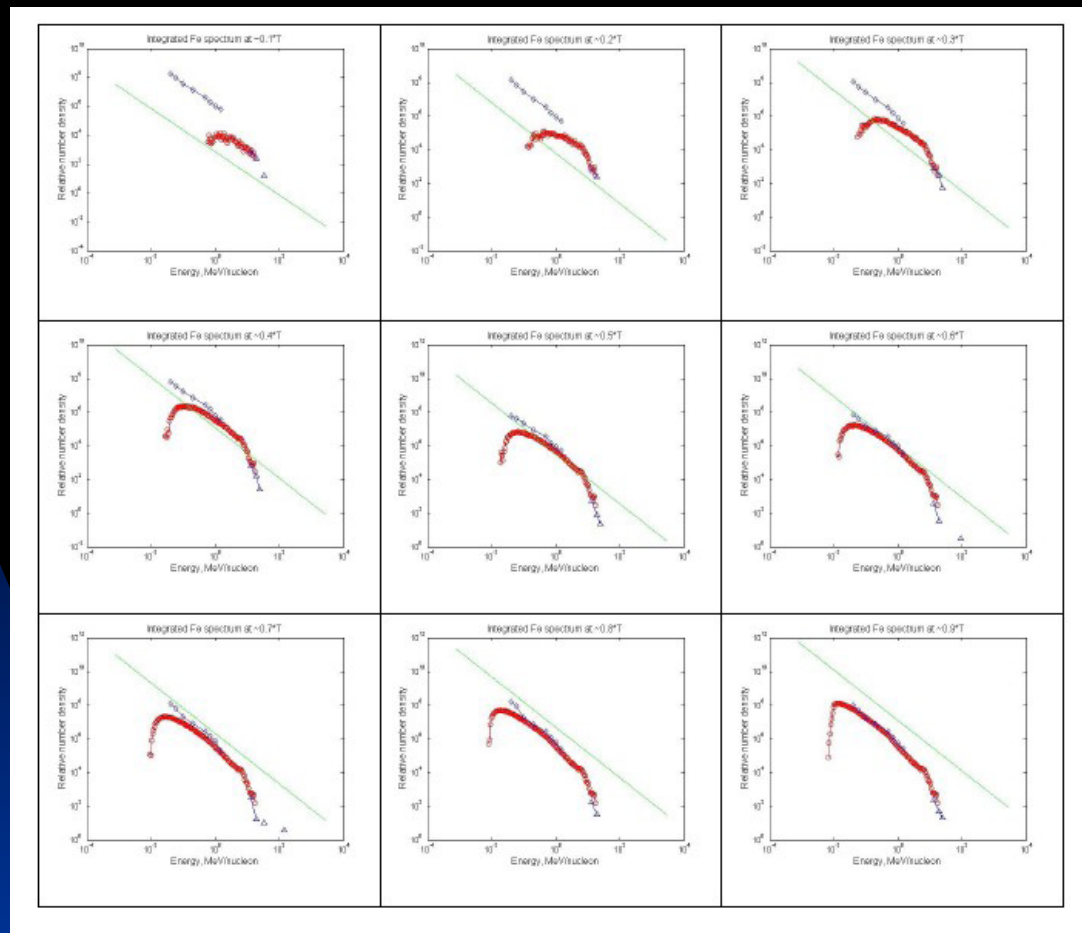
$$\lambda_{\parallel} = \lambda_0 \left(\frac{\tilde{p} c}{1 \text{ GeV}} \right)^{1/3} \left(\frac{A}{Q} \right)^{1/3} \left(\frac{r}{1 \text{ AU}} \right)^{2/3}$$

Maximum accelerated particle energy



The maximum energy accelerated at the shock front. Particles having higher energies, which are accelerated at earlier times but previously trapped in the shock complex, will “see” a sudden change of κ . The maximum energy/nucleon for CNO is higher than iron since the former has a larger Q/A , thus a smaller κ .

Bohm approximation used throughout strong shock simulation but only initially in weak shock case.

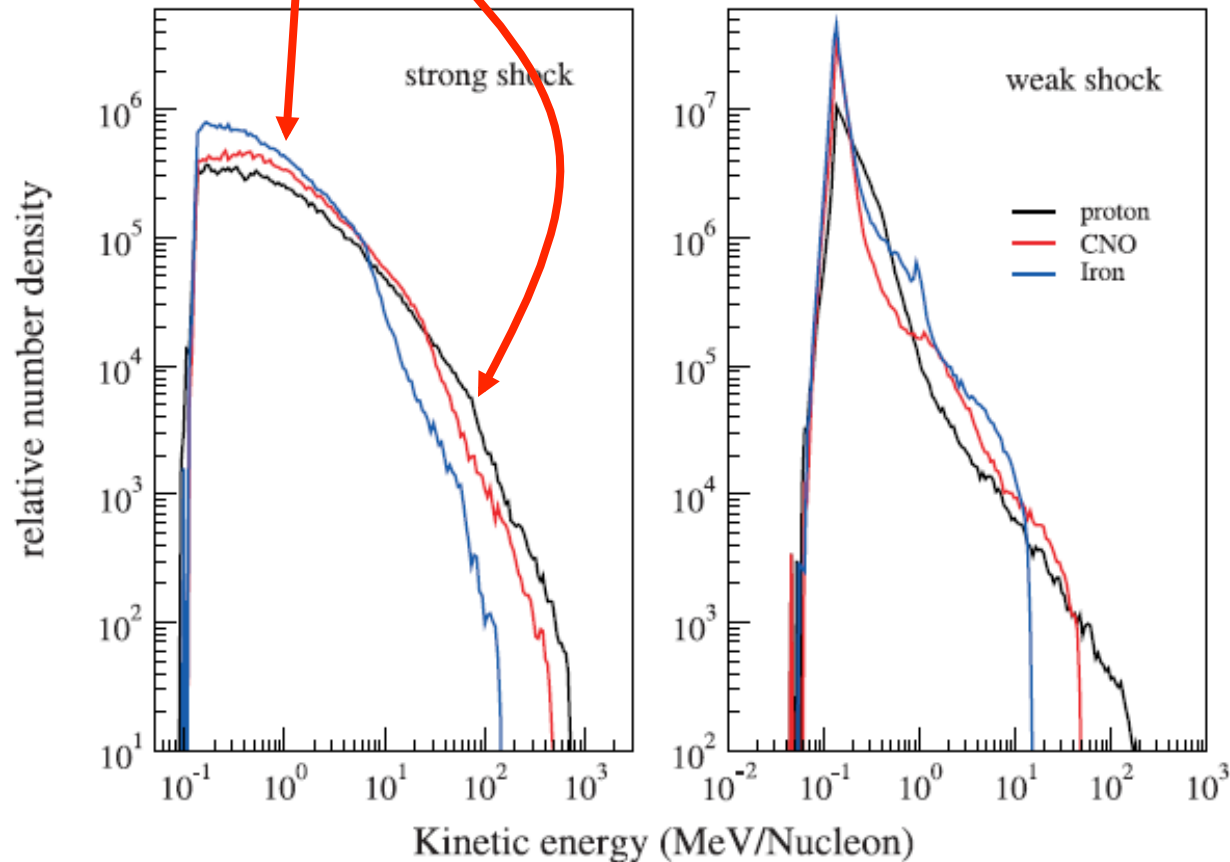


Dynamical spectra of iron ions averaged over consecutive ~5hrs time intervals until shock arrival at 1AU. ULEIS and SIS measurements are shown by blue diamonds and triangles, respectively. The straight line shows the theoretical limit for a power-law spectrum corresponding to shock parameters at 1 AU. Note the enhanced background at early times prior to the shock arrival at ~ 1AU.

SEP Event # 215 (shock arrival at ACE: Sept. 29, 2001, 09:06 UT)

Event integrated spectra

NOTE change in Fe/O ratio at about 10 MeV/nuc



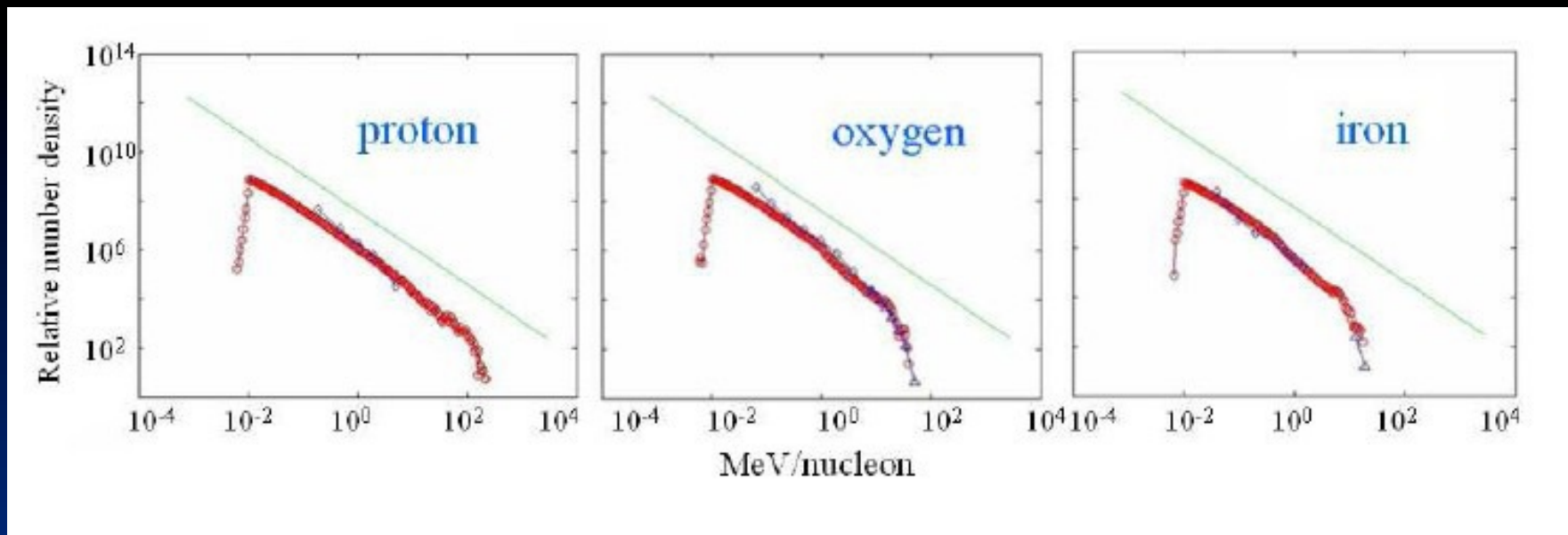
Iron $Q = 14$, $A = 56$

CNO $Q = 6$, $A = 14$

Similar spectral indices at low energies, with Iron slightly softer.

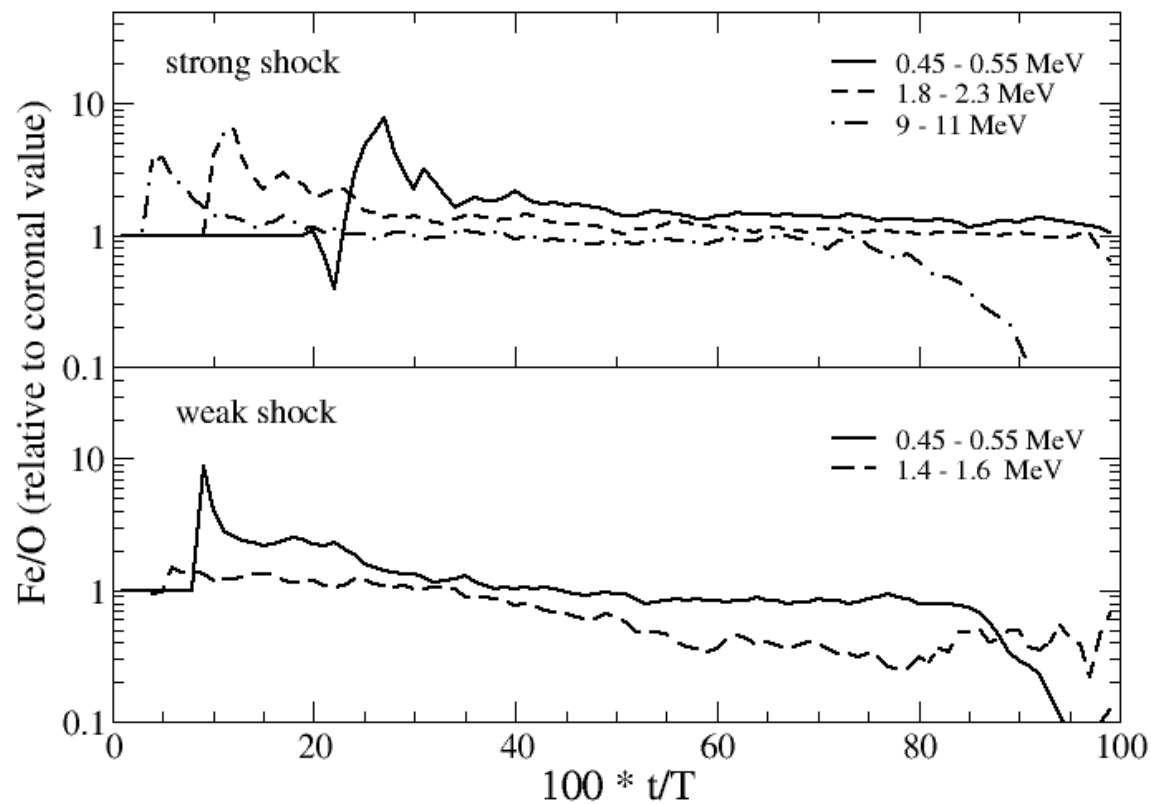
Roll-over feature at high energy end with approximately $(Q/A)^2$ dependence.

Count only those particles before the shock arrival.



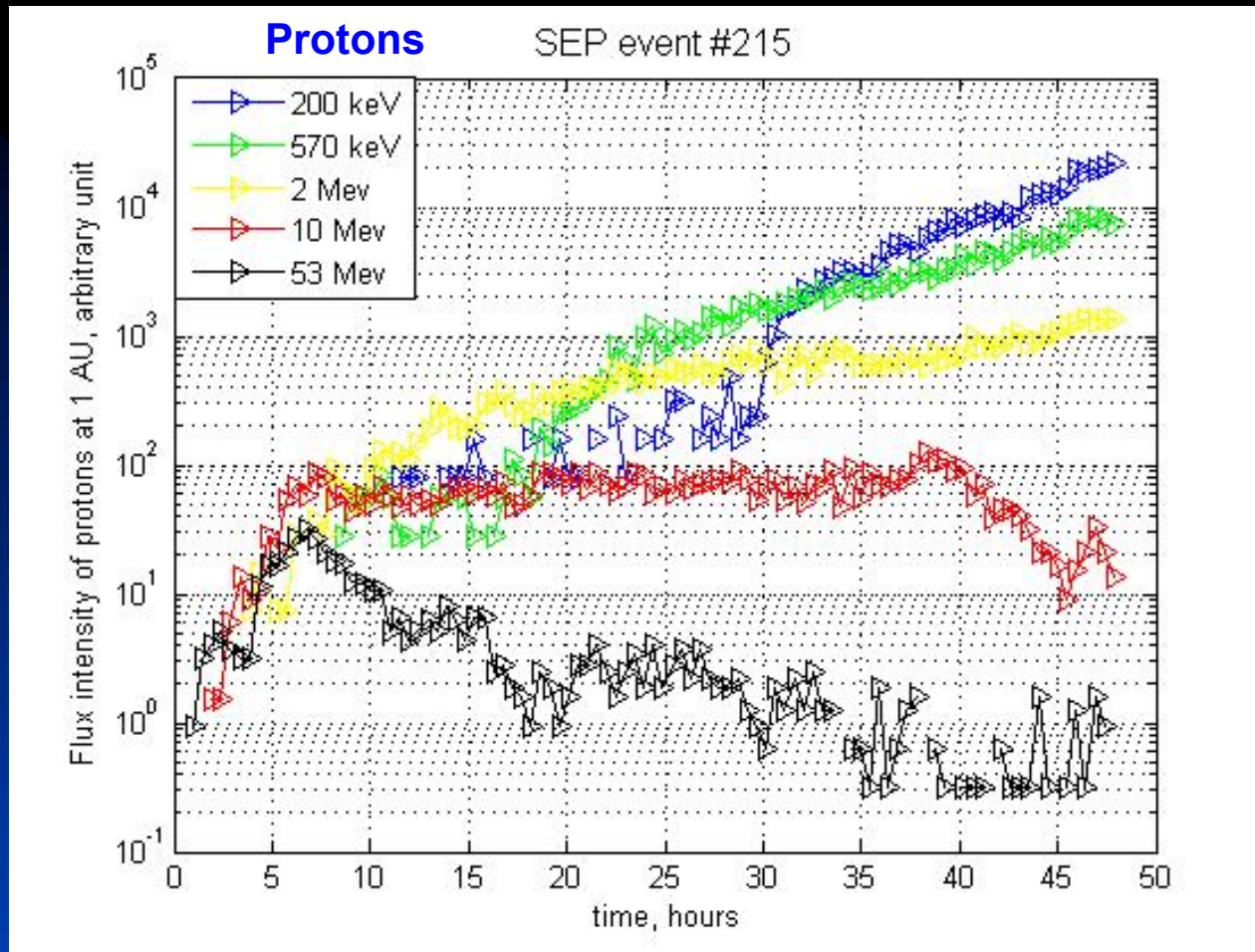
Event-integrated spectra for (a) protons, (b) oxygen and (c) iron ions. Modeling results are shown in red. ULEIS and SIS measurements integrated over the same time interval are shown by blue diamonds and triangles, respectively. The straight line shows the theoretical limit for a power-law spectrum corresponding to shock parameters at 1 AU. (Zank et al 2007; Verkhoglyadova et al. 2009).

SEP Event # 215 (shock arrival at ACE: Sept. 29, 2001, 09:06 UT)



Fe to O ratio for two cases. Differences can be ascribed to propagation and trapping - see previous figure.

Time intensity profiles



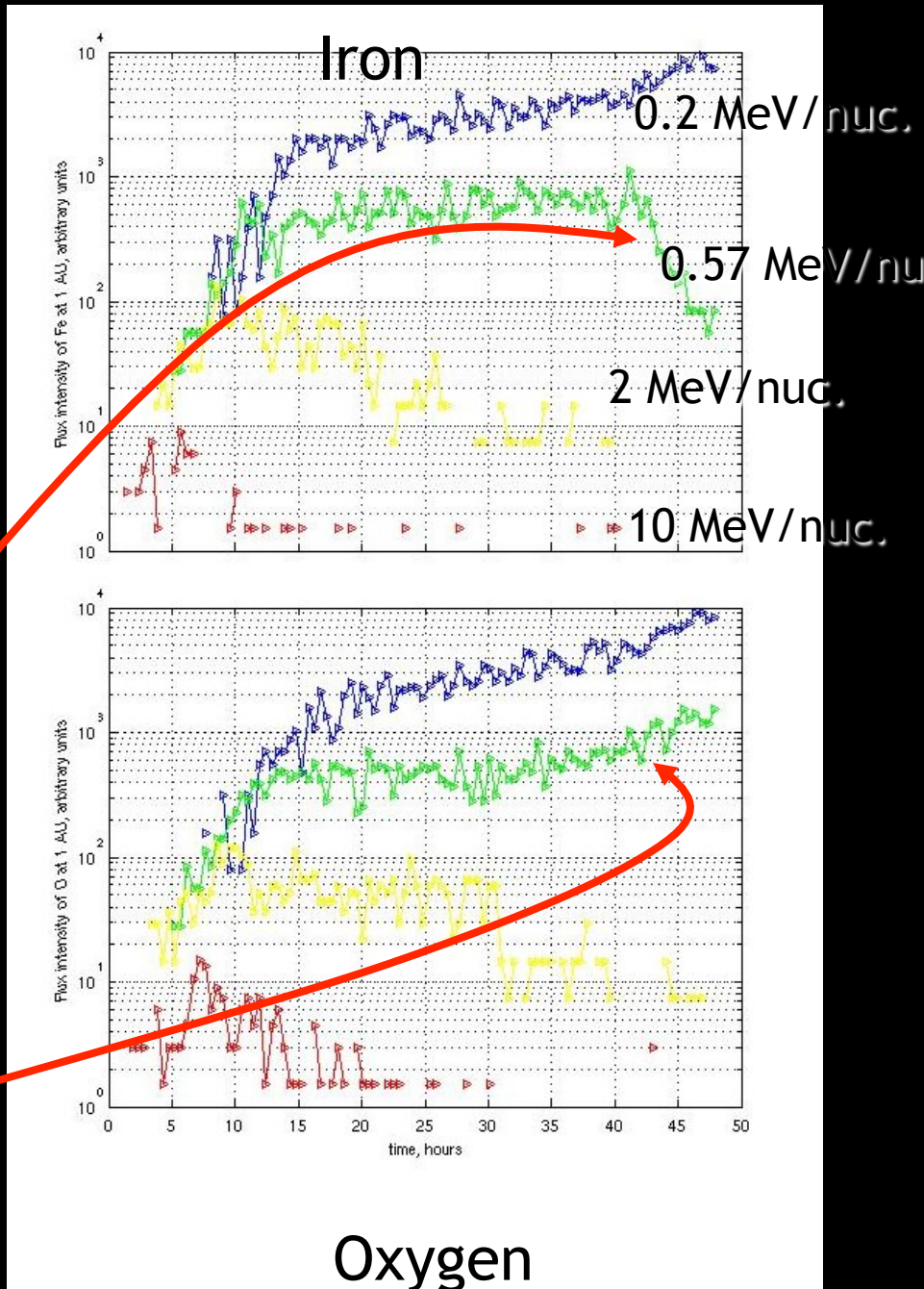
SEP Event # 215 (shock arrival at
ACE: Sept. 29, 2001, 09:06 UT)

s=2.5

Time intensity profiles

Time intensity profiles of iron and oxygen ions. Representative energies are (from top to bottom): 0.2, 0.57, 2 and 10 MeV/nucleon. Time is in hours starting from the shock launch at 0.1 AU until the shock arrival at 1 AU

NOTE change in Fe/O ratio after 40 hours



Summary of modeling - quasi-parallel shocks

- A time-dependent model of shock wave propagation (1- and 2-D), local particle injection, Fermi acceleration at the shock, and non-diffusive transport in the IP medium has been developed to describe observed SEP events: This includes spectra, intensity profiles, anisotropies.
- We can similarly model heavy ion acceleration and transport in gradual events, even understanding differences in Fe / O ratios, for example.
- We have begun to model mixed events to explore the consequences of a pre-accelerated particle population (from flares, for example) and have also related this to the timing of flare - CME events.

Perpendicular shocks

Particle acceleration at perpendicular shocks

The problems: 1) High injection threshold necessary
2) No self-excited waves

$$\frac{\partial f}{\partial t} + u \frac{\partial f}{\partial r} - \frac{p}{3} \frac{\partial u}{\partial r} \frac{\partial f}{\partial r} = \frac{\partial}{\partial r} \left(\kappa \frac{\partial f}{\partial r} \right); \quad \frac{\partial A}{\partial t} + u \frac{\partial A}{\partial r} = \Gamma A - \gamma A;$$

$$\kappa(p) = \frac{\kappa_0}{A(k)} \frac{B_0}{B} \frac{(p/p_0)^2}{\sqrt{(m_p c / p_0)^2 + (p/p_0)^2}}; \quad \kappa_0 = \frac{4}{3\pi} r_{g0} c = \frac{4}{3\pi} \frac{p_0 c}{e B_0},$$

INTEGRAL FORM OF THE NONLINEAR GUIDING CENTER THEORY

Matthaeus, Qin, Bieber, Zank [2003] derived a nonlinear theory for the perpendicular diffusion coefficient, which corresponds to a solution of the integral equation

$$K_{xx} = \frac{\alpha^2 v^2}{3B_0^2} \int_0^\infty \frac{S_{xx}(\mathbf{k}) d^3\mathbf{k}}{v/\lambda_p + k_\perp^2 K_{xx} + k_z^2 K_{zz}}$$

Superposition model: 2D plus slab

$$S_{xx}(\mathbf{k}) = S_{xx}^{2D} \delta(k_\perp) \delta(k_z) + S_{xx}^{slab} \delta(k_\perp)$$

Solve the integral equation approximately (Zank, Li, Florinski, et al, 2004):

$$\lambda_{xx}; \left(\sqrt{3}\pi\alpha^2 C\right)^{2/3} \left(\frac{\langle b_{2D}^2 \rangle}{B_0^2}\right)^{2/3} \lambda_{2D}^{2/3} \lambda_p^{1/3} \left[1 + \frac{(\alpha^2 C)^{1/3}}{(\sqrt{3}\pi)^{2/3}} \frac{\langle b_{slab}^2 \rangle}{\langle b_{2D}^2 \rangle^{2/3} (B_0^2)^{1/3}} \frac{\min(\lambda_{slab}, \lambda_p/\sqrt{3})}{\lambda_{slab}^{2/3} \lambda_p^{1/3}} \left(4.33H(\lambda_{slab} - \lambda_p/\sqrt{3}) + 3.091H(\lambda_p/\sqrt{3} - \lambda_{slab}) \right) \right]^{2/3}$$

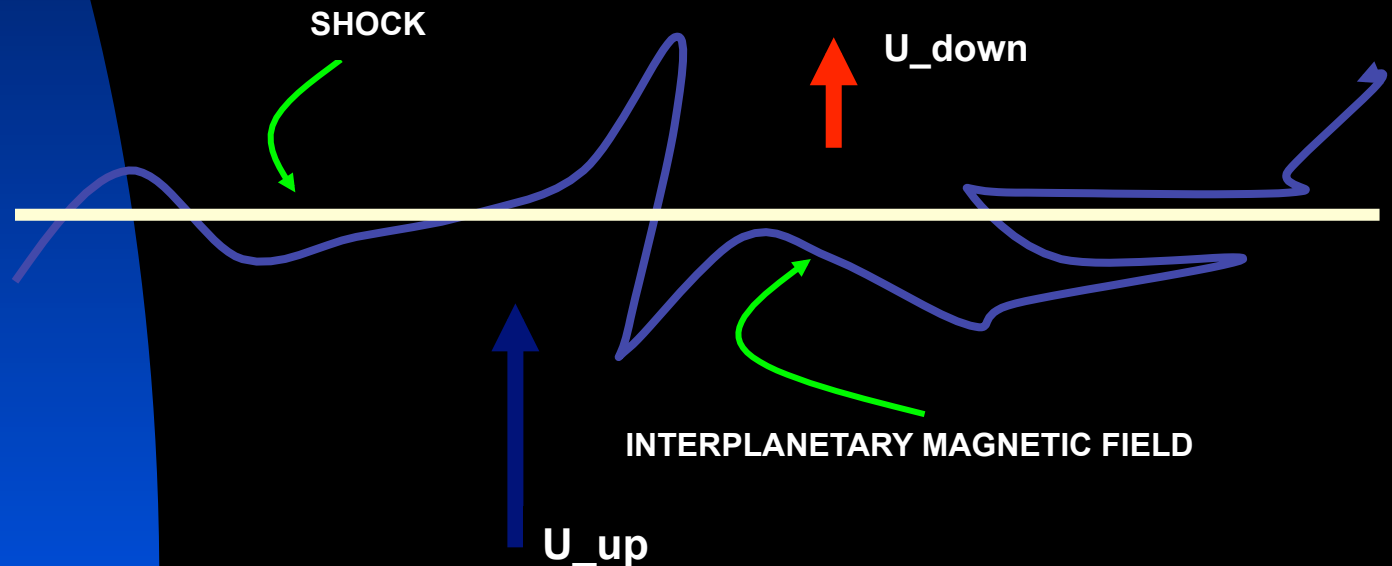
λ_p modeled according to QLT.

WHAT ABOUT WAVE EXCITATION UPSTREAM?

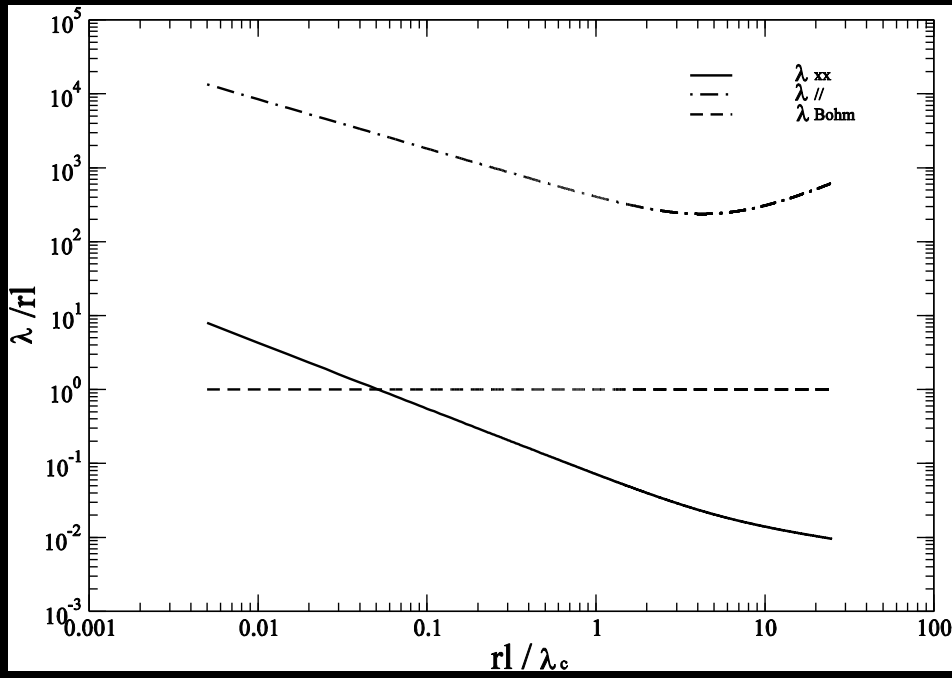
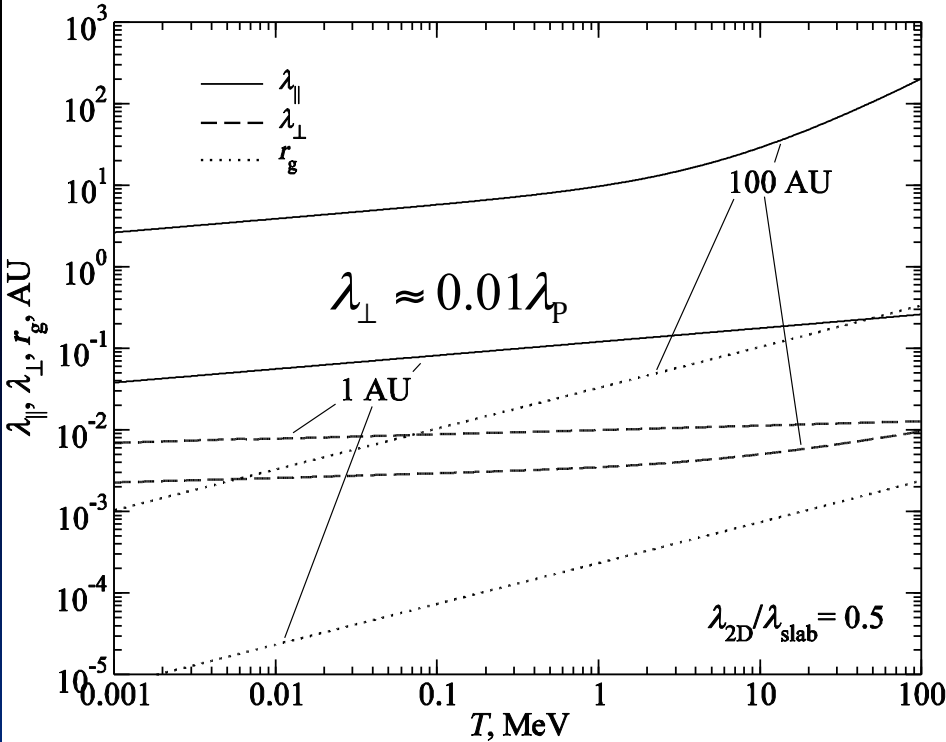
Quasi-linear theory (Lee, 1983; Gordon et al, 1999): wave excitation proportional to $\cos \psi$ i.e.,

$$\frac{\partial I}{\partial t} \approx 0$$

at a highly perpendicular shock.



CSPAR-UAH



Left: Plot of the parallel (solid curve) and perpendicular mfp (dashed curve) and the particle gyroradius (dotted) as a function of energy for 100 AU (the termination shock) and 1 AU (an interplanetary shock).

Right: Different format - plots of the mean free paths at 1 AU as a function of particle gyroradius and now normalized to the correlation length. *The graphs are equivalent to the ratio of the diffusive acceleration time to the Bohm acceleration time, and each is normalized to gyroradius.* Solid line corresponds to normalized (to the Bohm acceleration time scale) perpendicular diffusive acceleration time scale, the dashed-dotted to parallel acceleration time scale, and the dashed to Bohm acceleration time scale (obviously 1).

Remarks re maximum energies - different shock configurations and ionic species

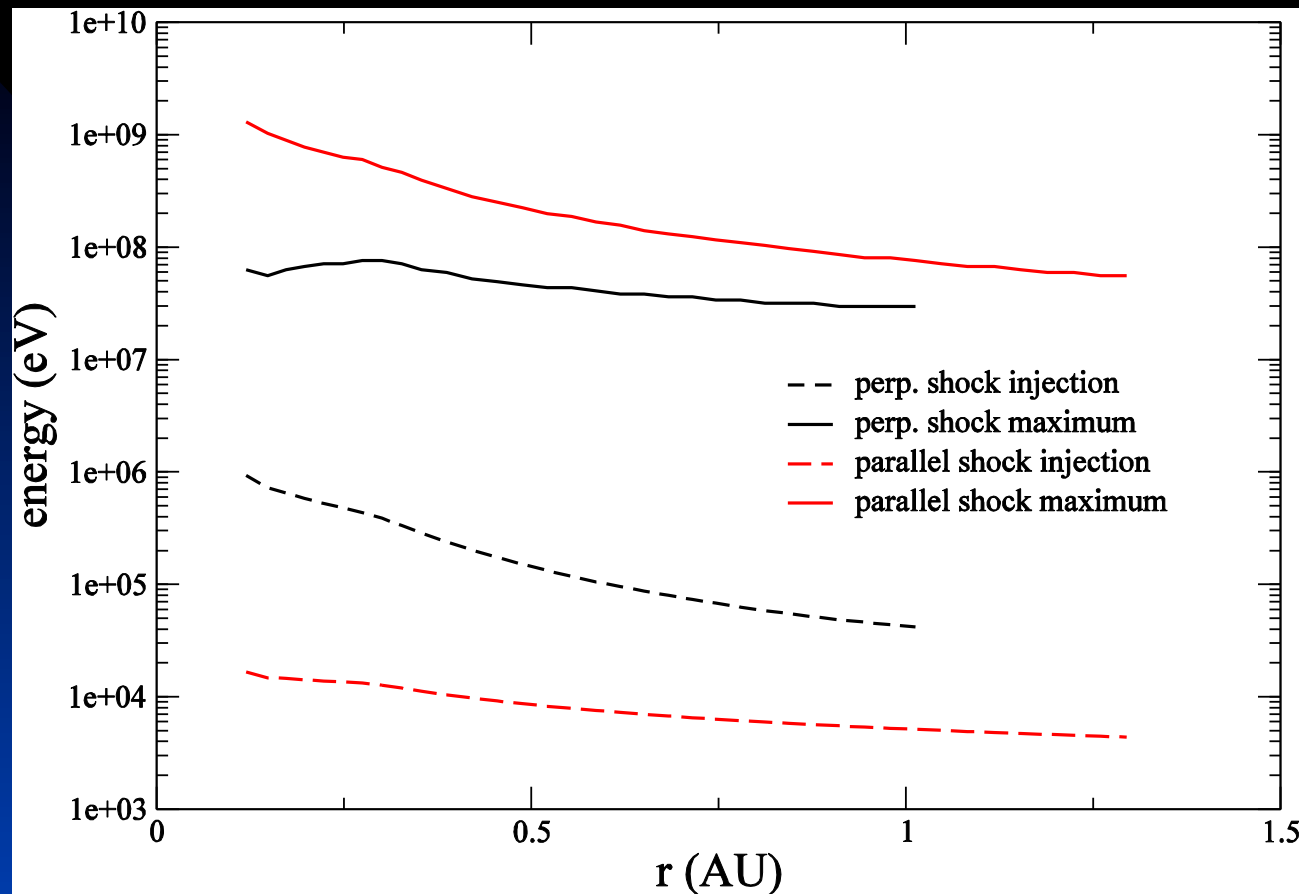
Three approaches have been identified for determining p_{\max} [Zank et al 2000; Li et al 2003, Zank et al., 2006].

- 1. For protons accelerated at quasi-parallel shock, p_{\max} determined solely on basis of balancing the particle acceleration time resulting from resonant scattering with the dynamical timescale of the shock. The wave/turbulence spectrum excited by the streaming energized protons extends in wave number as far as the available dynamical time allows.
- 2. For heavy ions at a quasi-parallel shock, the maximum energy is also computed on the basis of a resonance condition but only up to the minimum k excited by the energetic streaming ions, which control the development of the wave spectrum. Thus, maximum energies for heavy ions are controlled by the accelerated protons and their self-excited wave spectrum. This implies a $(Q/A)^2$ dependence of the maximum attainable particle energy for heavy ions.

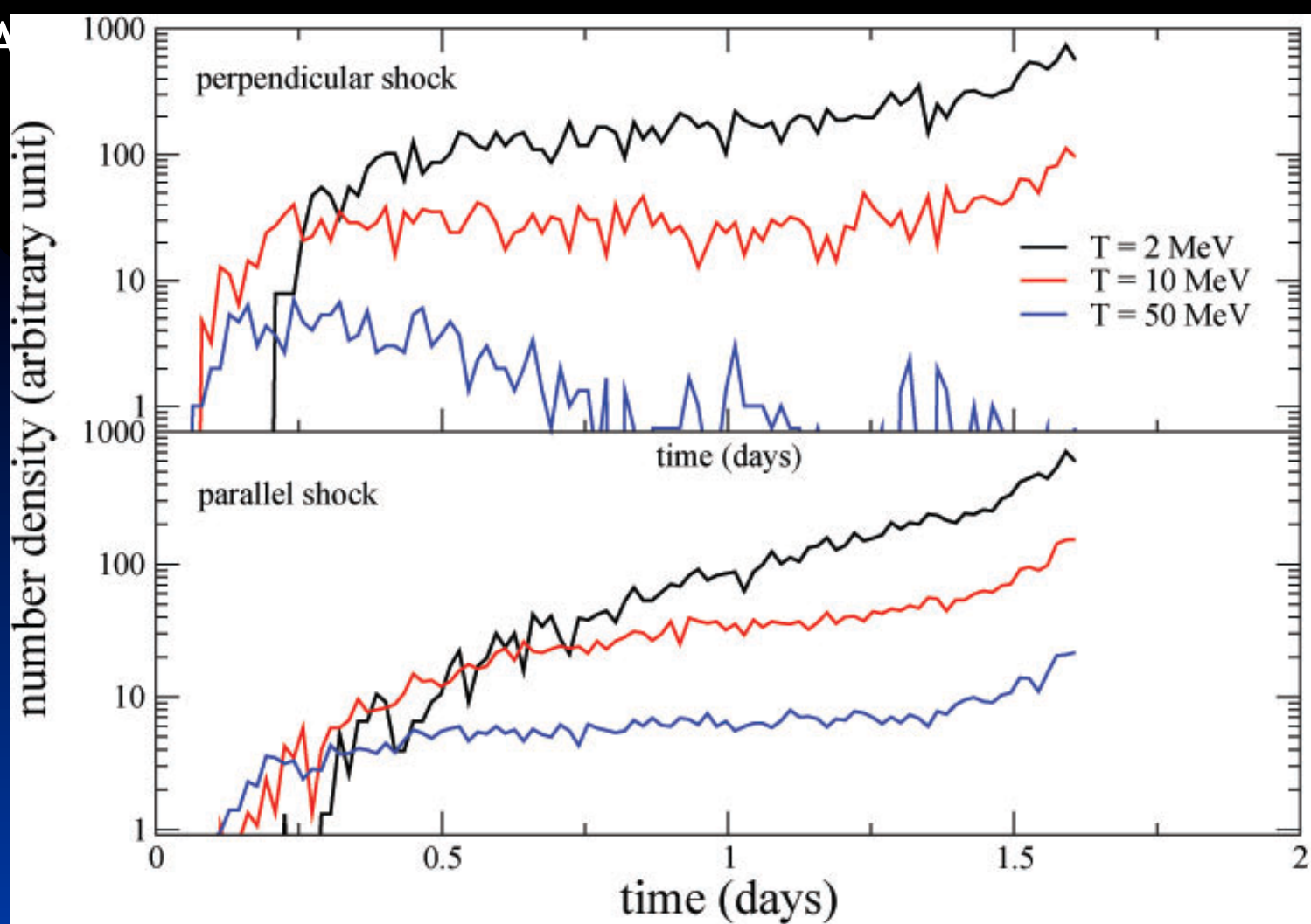
Remarks re maximum energies - different shock configurations and ionic species

- 3. For protons at a highly perpendicular shock, the maximum energy is independent of the resonance condition, depending only on the shock parameters and upstream turbulence levels. For heavy ions, this implies either a $(Q/A)^{1/2}$ or a $(Q/A)^{4/3}$ dependence of the maximum attainable particle energy, depending on the relationship of the maximum energy particle gyroradius compared to turbulence correlation length scale.
- Can extract observational signatures related to the mass - charge ratio that distinguish particle acceleration at quasi-parallel and highly perpendicular shocks (e.g., Mason et al 2012).

Maximum and injection energies

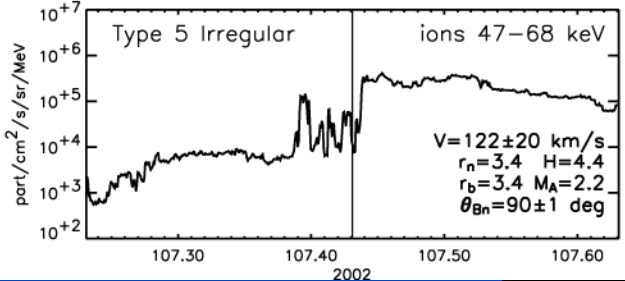
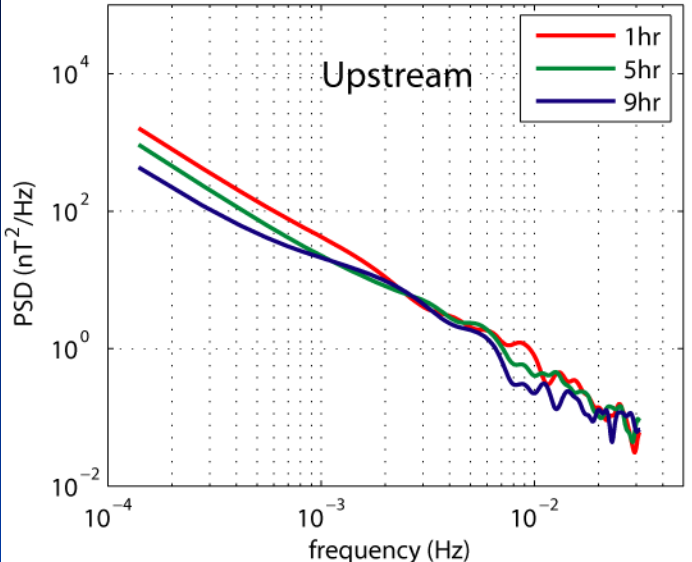
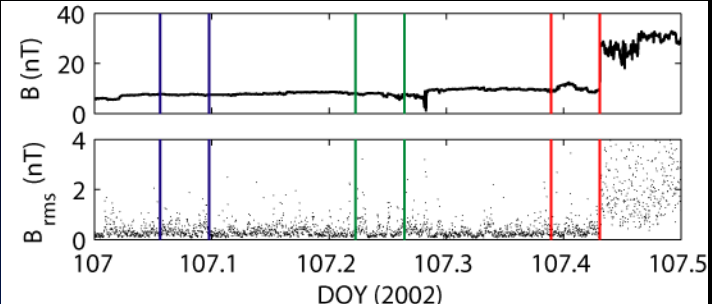


- Remarks: 1) Parallel shock calculation assumes wave excitation implies maximum energies comparable
- 3) Injection energy at Q-perp shock much higher than at Q-par therefore expect signature difference in composition

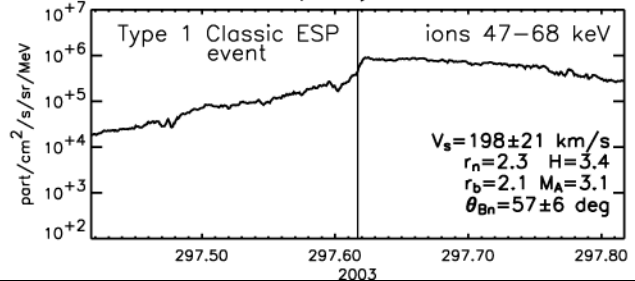
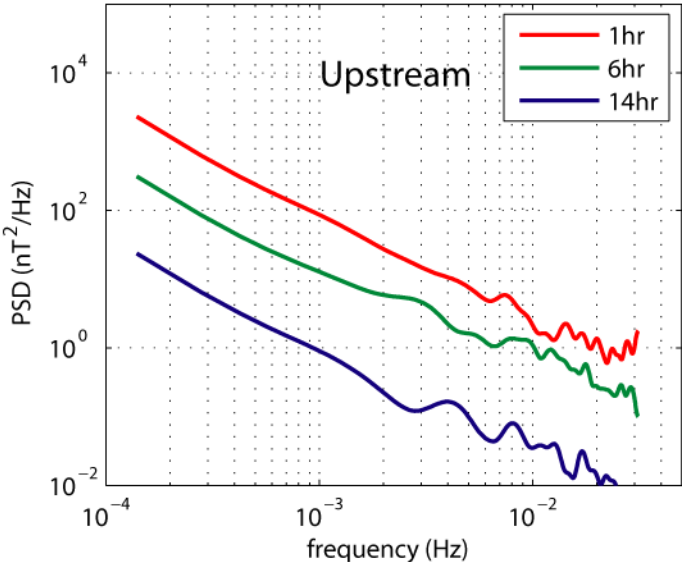
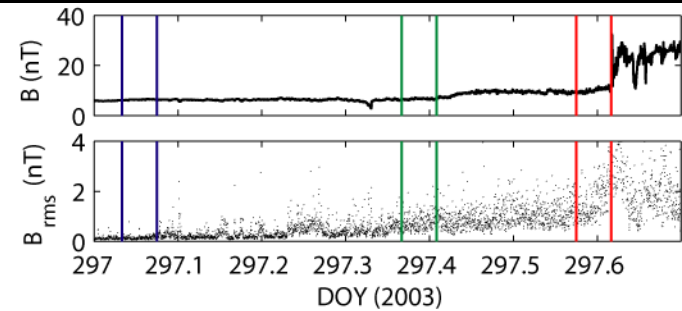


Intensity profiles emphasize important role of time dependent maximum energy to which protons are accelerated at a shock and the subsequent efficiency of trapping these particles in the vicinity of the shock. Compared to parallel shock case, particle intensity reaches plateau phase faster for a quasi-perpendicular shock - because K_{perp} at a highly perpendicular shock is larger than the stimulated K_{par} at a parallel shock, so particles (especially at low energies) find it easier to escape from the quasi-perpendicular shock than the parallel shock.

Perpendicular shock



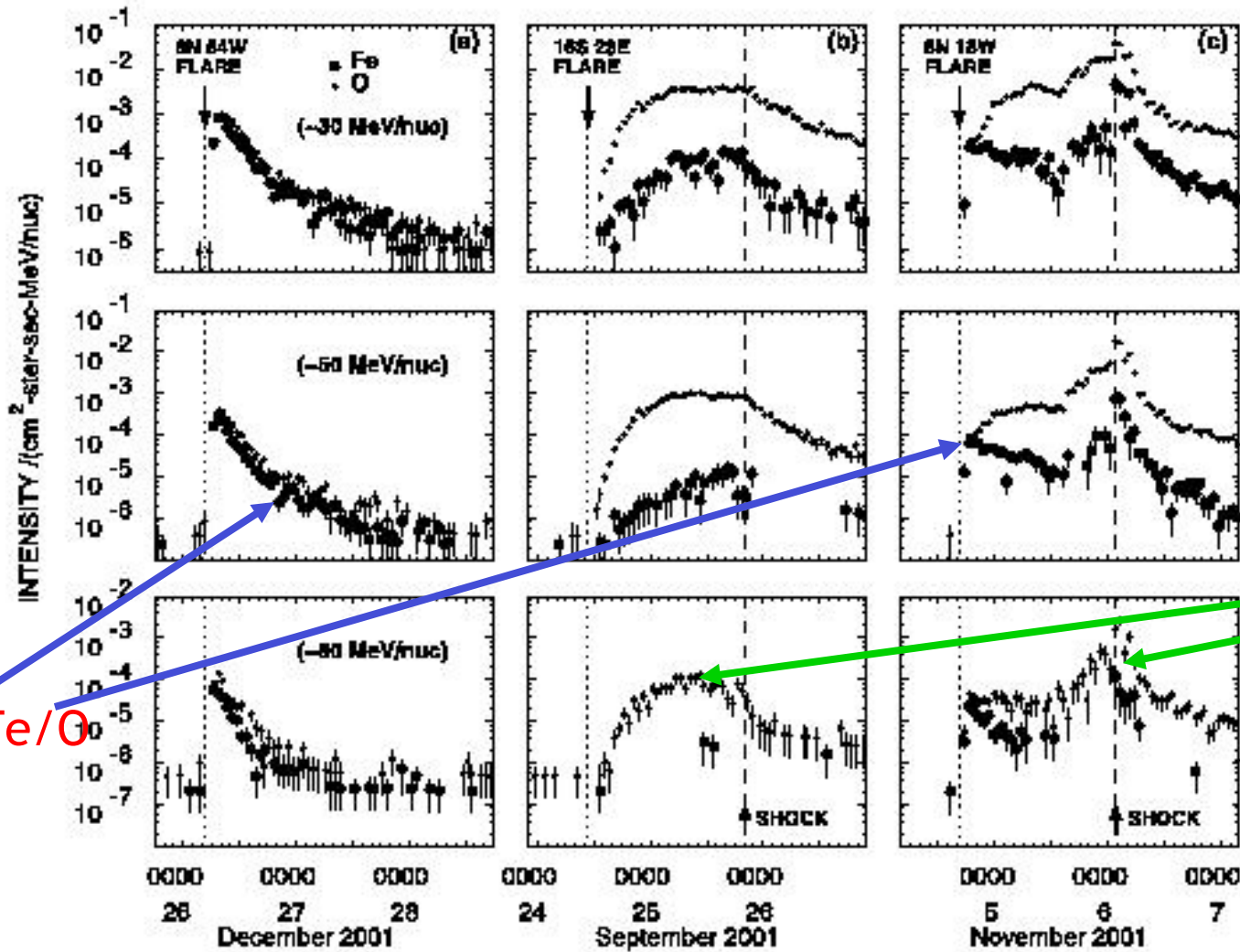
Quasi-perp shock



CONCLUDING REMARKS FOR PERPENDICULAR SHOCKS

- Developed basic theory for particle acceleration at highly perpendicular shocks based on convection of in situ solar wind turbulence into shock.
- Highest injection energies needed for quasi-perp shocks and not for pure perpendicular shock. 90 degree shock “singular” example.
- Determination of K_{perp} based on Nonlinear Guiding Center Theory
- Maximum energies at quasi-perp shocks less than at quasi-par shocks near sun. Further from sun, reverse is true.
- Injection energy threshold much higher for quasi-perp shocks than for quasi-parallel shocks and therefore can expect distinctive compositional signatures for two cases.
- Observations support notion of particle acceleration at shocks in absence of stimulated wave activity.

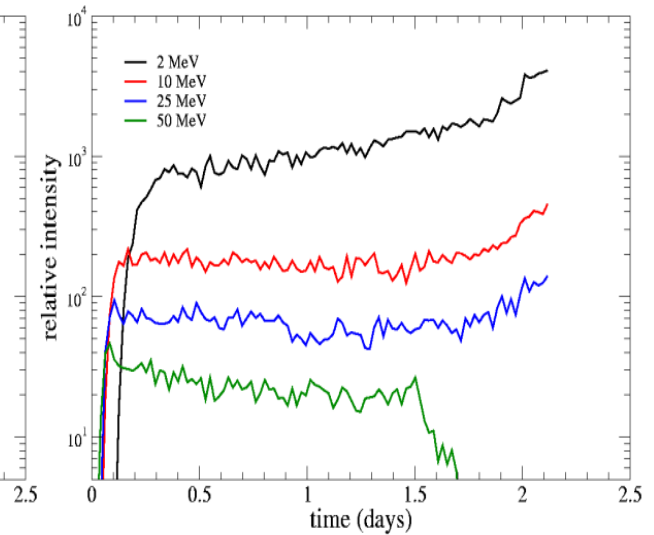
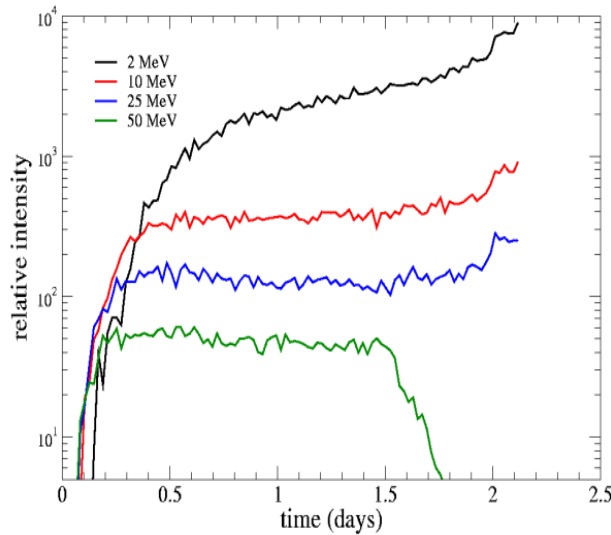
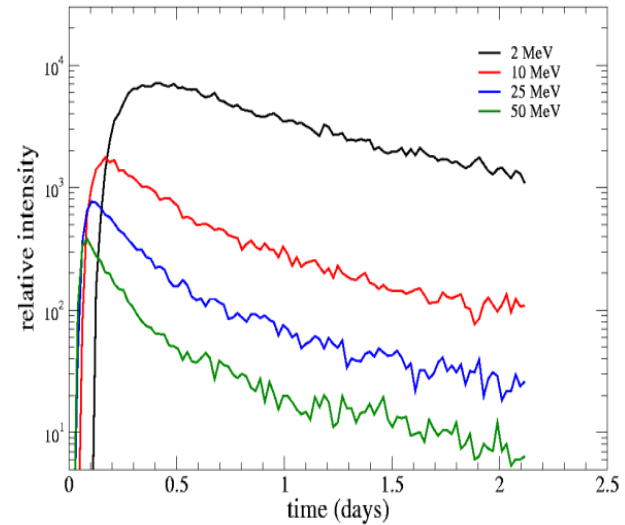
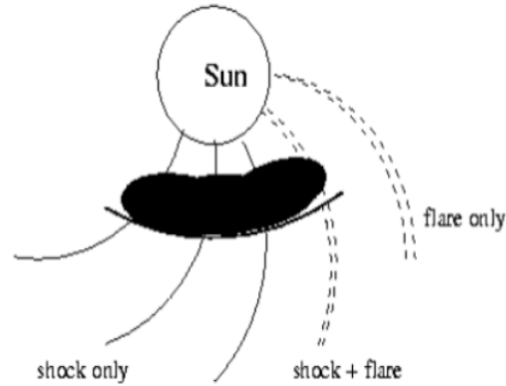
Pre-existing or no pre-existing "injection" population - Cane et al., 2003



High Fe/O

Low Fe/O

Modeling the 3 Cane possibilities



USING THE PATH CODE FOR MODELING GRADUAL SEP EVENTS IN THE INNER HELIOSPHERE

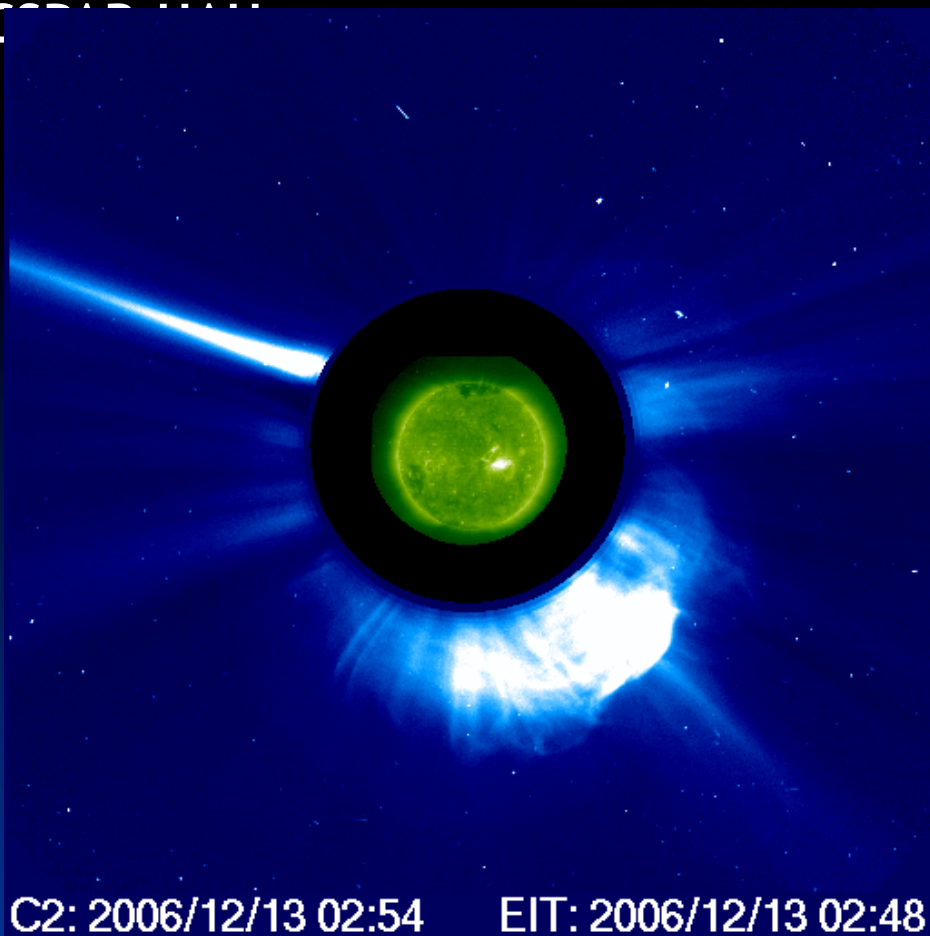
O. P. VERKHOGLYADOVA^{1,2}, G. LI^{3,1}, G. P. ZANK^{3,1}, Q. HU^{1,2}, AND R. A. MEWALDT⁴

December 13, 2006 event

JOURNAL OF GEOPHYSICAL RESEARCH, VOL. 115, A12103, doi:[10.1029/2010JA015615](https://doi.org/10.1029/2010JA015615), 2010

Understanding large SEP events with the PATH code: Modeling of the 13 December 2006 SEP event

O. P. Verkhoglyadova,¹ G. Li,^{1,2} G. P. Zank,^{1,2} Q. Hu,¹ C. M. S. Cohen,³ R. A. Mewaldt,³
G. M. Mason,⁴ D. K. Haggerty,⁴ T. T. von Rosenvinge,⁵ and M. D. Looper⁶

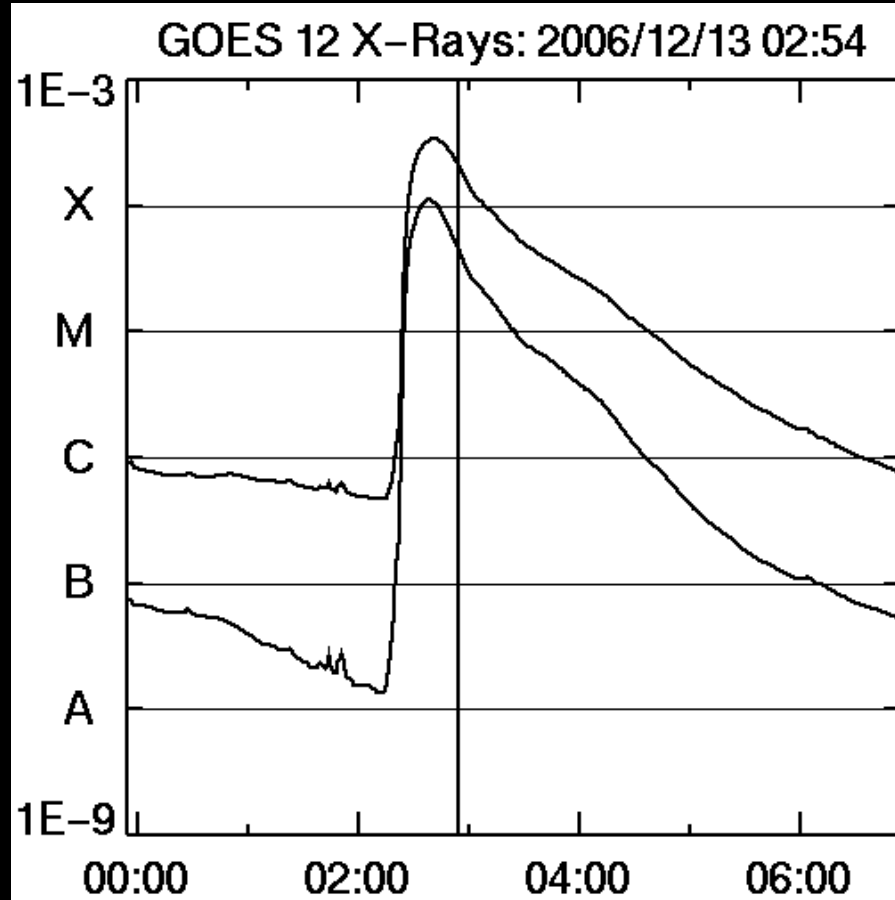


C2: 2006/12/13 02:54 EIT: 2006/12/13 02:48

Halo CME: Dec. 13, 2006: 02:54:04

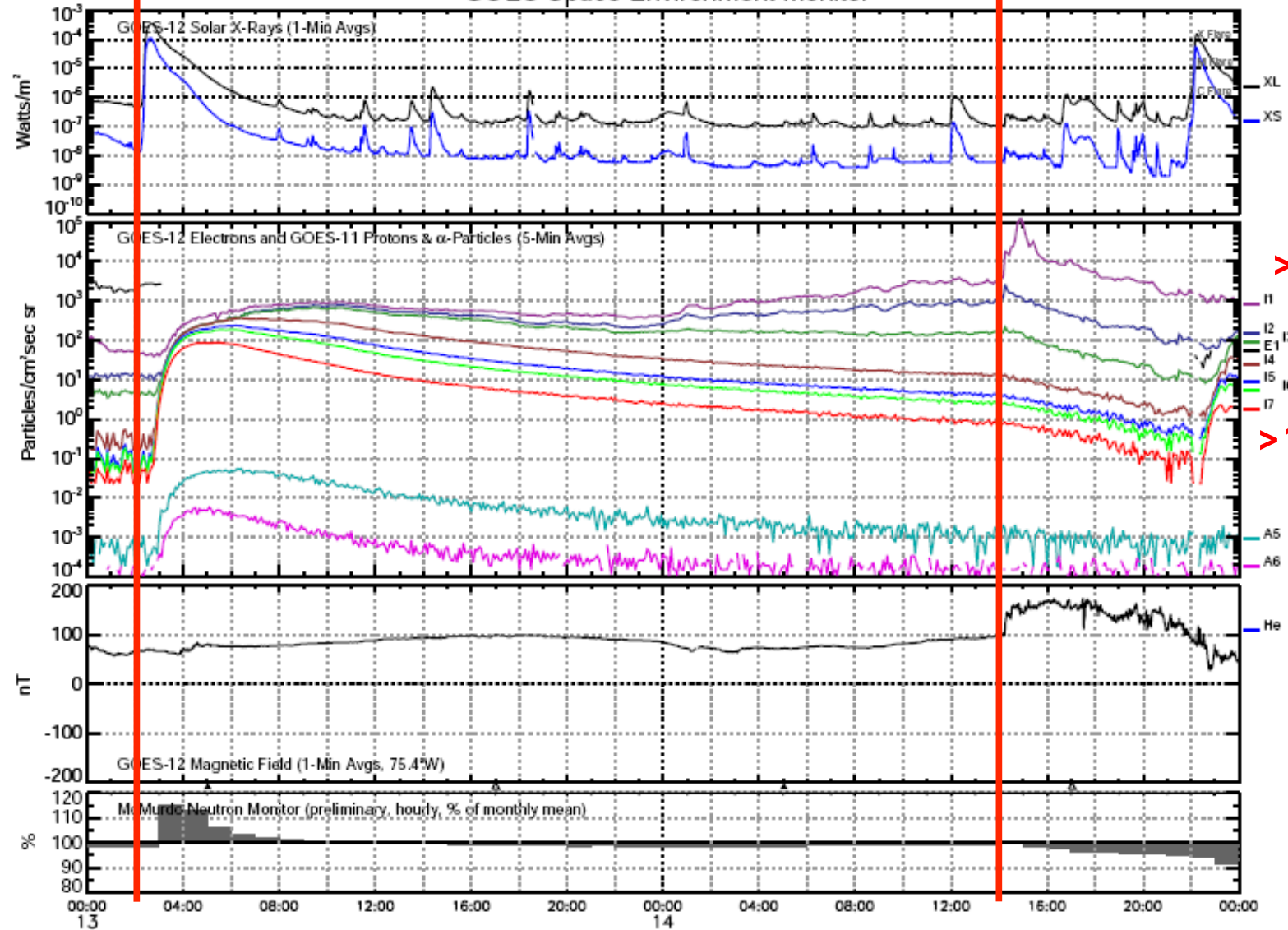
linear speed: 1774 km/sec;
speed at 20 R: 1573 km/sec;

(from the SOHO/LASCO CME
Catalog, courtesy of the CDAW
Data Center, GSFC).



ESP Event (shock arrival at ACE:
Dec. 14, ~1400 UT)

GOES Space Environment Monitor




















>1 MeV
>100 MeV

December 2006 (Universal Time)

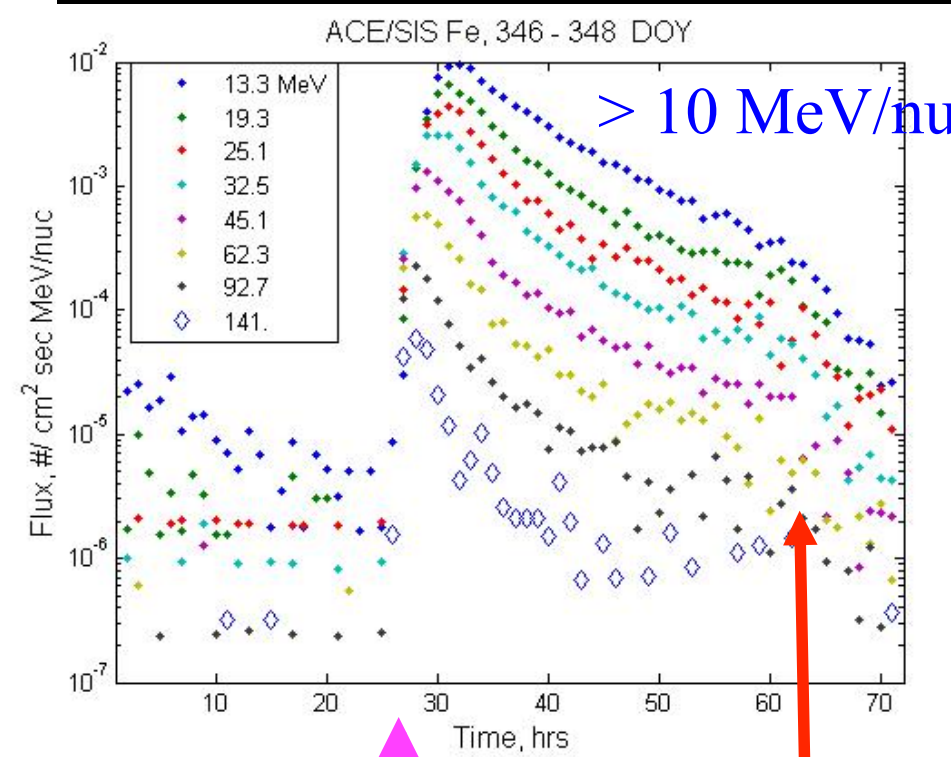
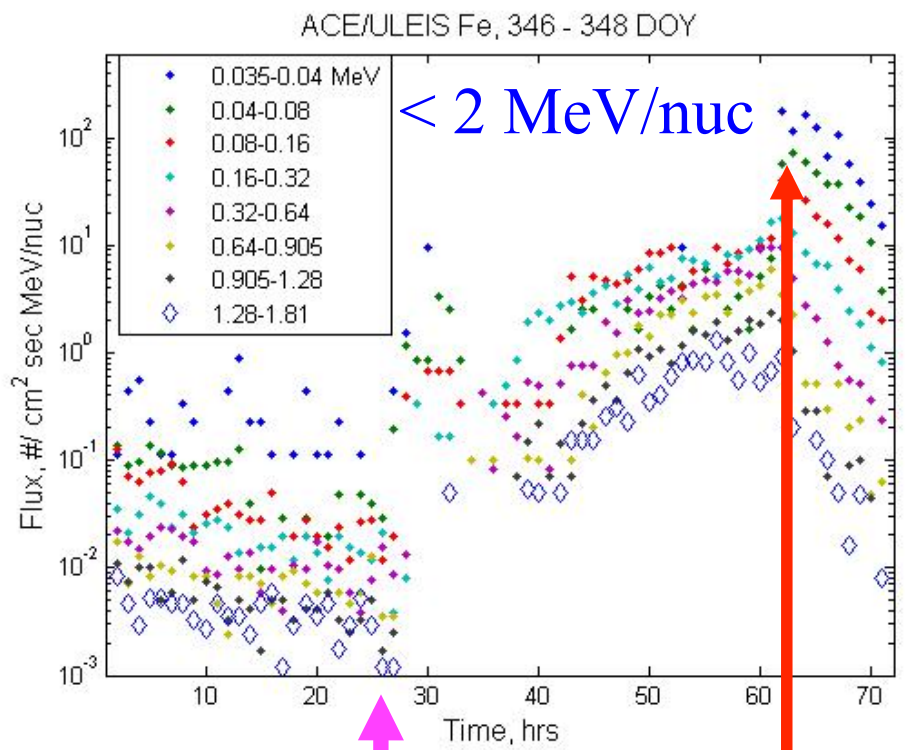


GOES SEM Data Key

	XL	1 - 8 Å X-rays (Watts/m ²)
	XS	0.5 - 3 Å X-rays, or 0.5 - 4 Å prior to GOES-8 (Watts/m ²)
	E1	> 2 MeV (Electrons/cm ² sec sr)
	I1	> 1 MeV (Protons/cm ² sec sr)
	I2	> 5 MeV (Protons/cm ² sec sr)
	I3	> 10 MeV (Protons/cm ² sec sr)
	I4	> 30 MeV (Protons/cm ² sec sr)
	I5	> 50 MeV (Protons/cm ² sec sr)
	I6	> 60 MeV (Protons/cm ² sec sr)
	I7	> 100 MeV (Protons/cm ² sec sr)
	A5	150-250 MeV, 160-260 prior to GOES-8 (α-particles/cm ² sec sr MeV)
	A6	300-500 MeV, 330-500 prior to GOES-8 (α-particles/cm ² sec sr MeV)
	H _P	Perpendicular to orbital plane (nanotesla)
	H _E	Earthward (nanotesla)
	H _N	Normal to H _P and H _E .
	△	Satellite Local Noon
	▲	Satellite Local Midnight



ACE observations: Fe ions



flare

Energy ranges are in MeV/nuc

Approximate shock arrival time.

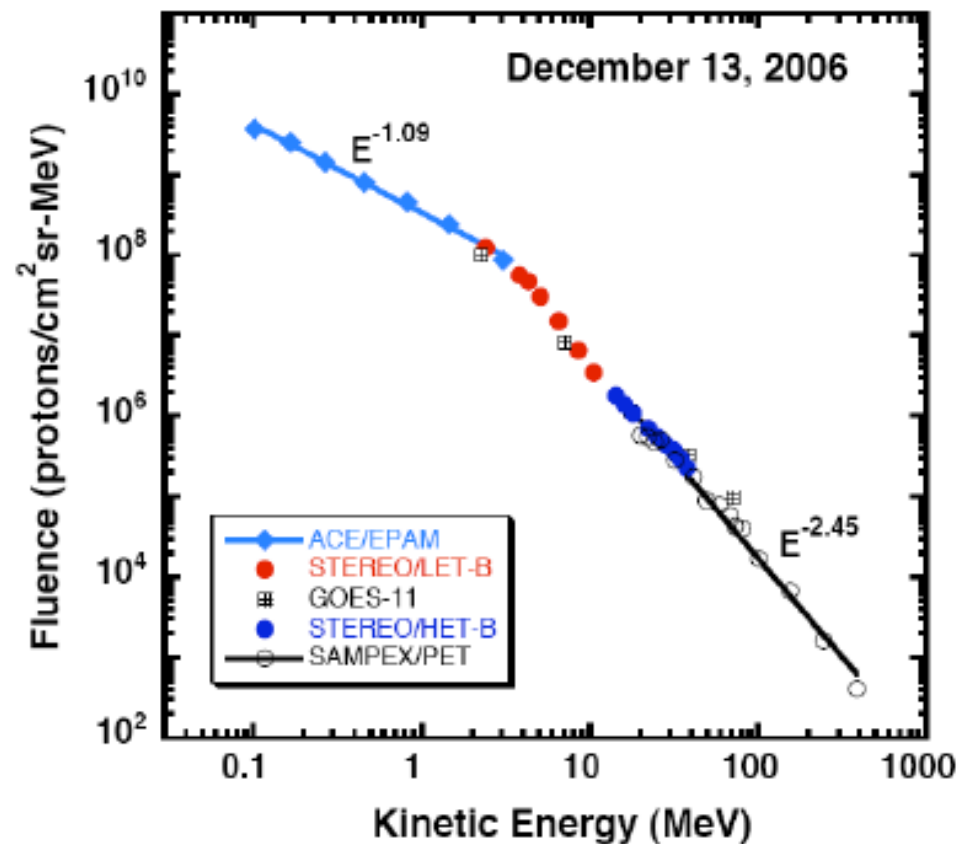
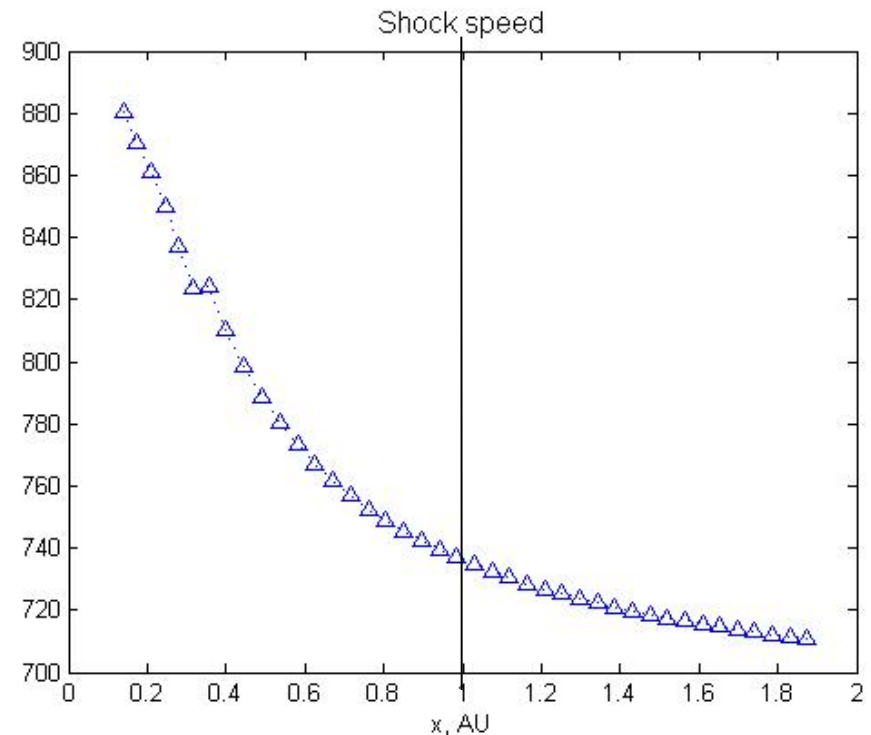
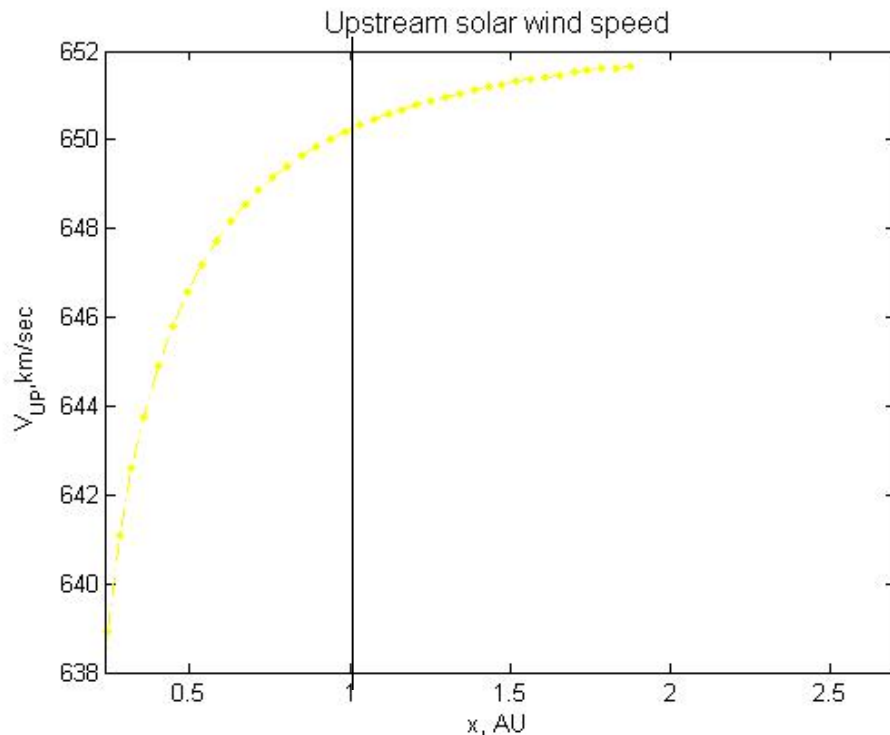


Figure 3. Event-integrated energetic proton spectra obtained with ACE, STEREO, GOES-11 and SAMPEX for the December 13, 2006 SEP event.

The PATH code (1D):

- ☑ SW modeling: initialization of the code;
- ☑ 1D MHD shock modeling: boundary conditions;
- ☑ DSA at a quasi-parallel shock (seed particles)
- ☑ Transport to 1 AU (time-intensity profiles; event-integrated spectra, etc.)



Shock parameters at 1 AU (derived from ACE observations):

Compression ratio: 3.0 ± 0.3

Upstream SW speed: 650 ± 30 km/sec;

Shock speed: 800 ± 50 km/sec;

Arrival time ~ 35 hrs

Theta_Bn ~ 30;

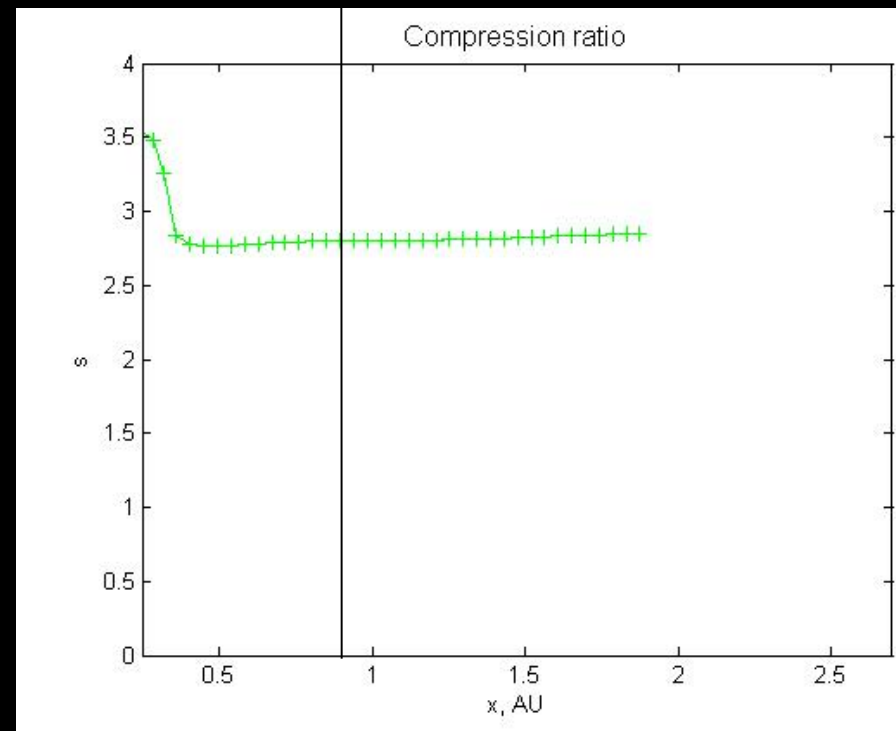
Model (at 1 AU):

Compression ratio: 2.8

Upstream SW speed: 650 km/sec;

Shock speed: 730 km/sec;

Arrival time ~ 49 hrs



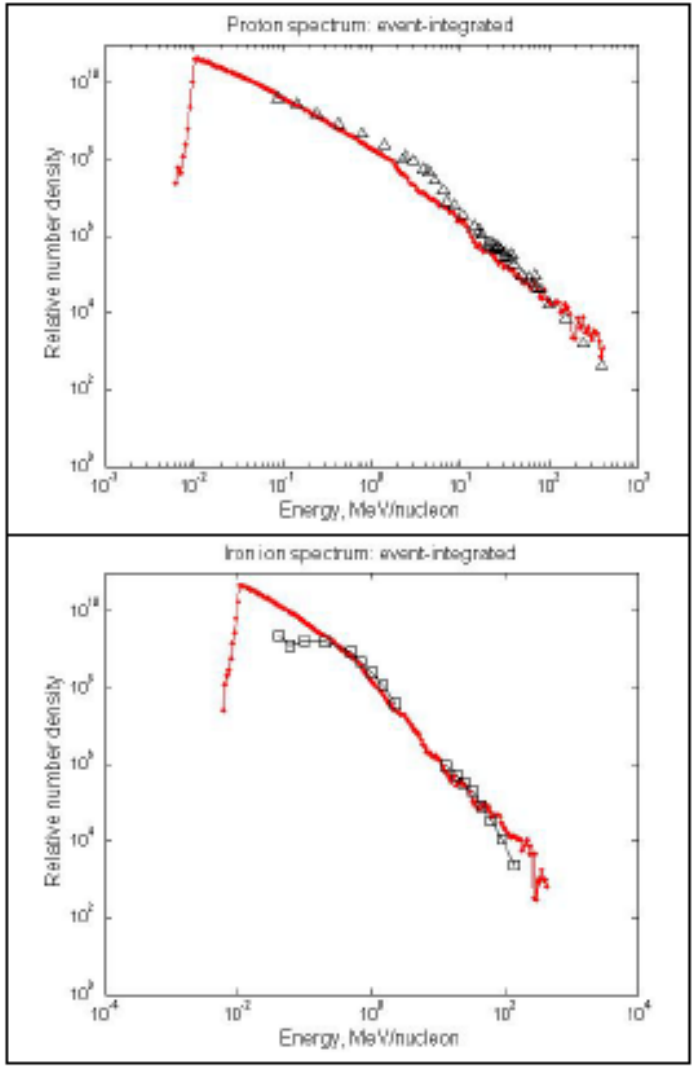


Figure 8. a) Event-integrated proton spectrum. PATH code results are shown by the red line. Fluences obtained with ACE, STEREO, GOES-11 and SAMPEX are shown by triangles. b) Event-integrated iron ion spectrum. PATH code results are shown by the red line. Fluences derived from ACE measurements are shown by squares.

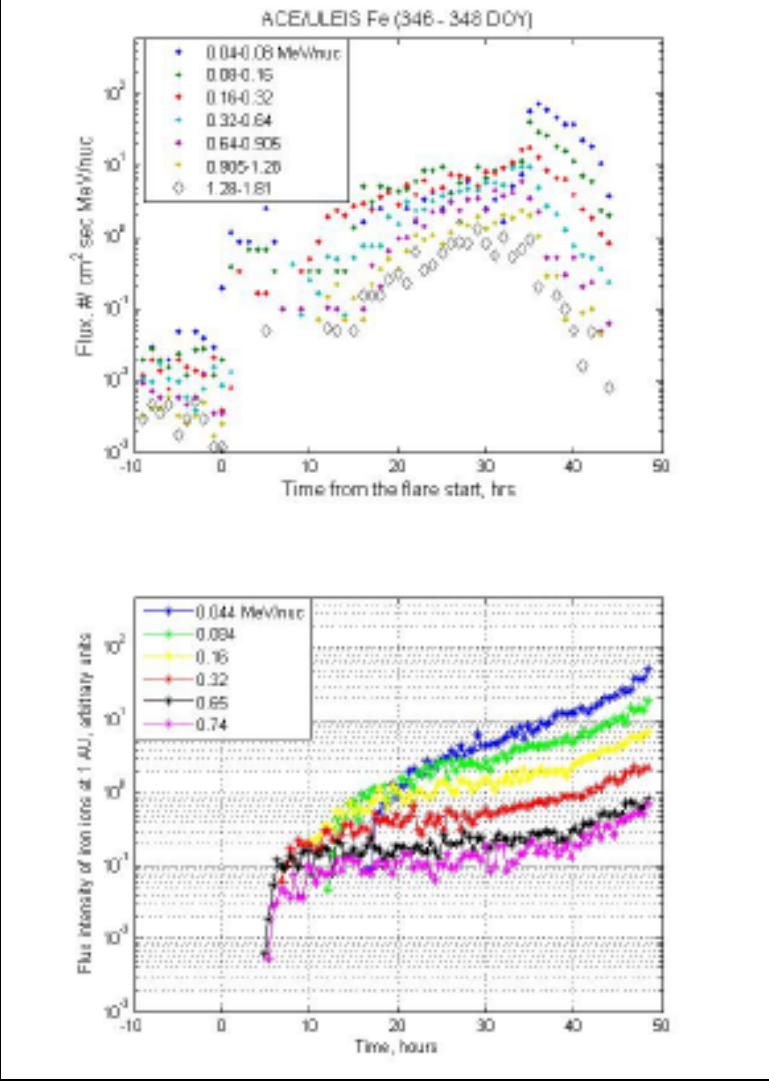


Figure 7. Iron ion fluxes derived from ACE/ULEIS measurements in a low-energy range of ~35 keV/nuc – 2 MeV/nuc at 1 AU (top panel) and corresponding modeling results with the PATH code (bottom panel). Notice a rise in particle fluxes around the shock arrival time.

Conclusions:

- PATH model applied to explain observations of the large SEP event of Dec. 13, 2006.
- Based on the PATH model we can describe/understand main features of ion spectra and intensity profiles.
- Modeling results describe contribution from both flare and shock-accelerated particles.
- Currently our model is being extended to 2D/3D geometry (oblique shock configuration) with perpendicular diffusion included.
- Different charge states for the particles and SW suprathermals will be included in the model.

Free parameters of the model

- Escape length (p)
- MFP scaling and dependence on r and p
- *Injection energy (10 keV) and efficiency (1% flux density)*
- *Flare parameters: duration, max/min p , spectra;*
- *Ratio of flare to shock-accelerated particles*
(Zank et al., 2000; Li et al., 2003; 2005; Zank et al., 2007)

Summary of modeling

- A time-dependent model of shock wave propagation (1- and 2-D), local particle injection, Fermi acceleration at the shock, and non-diffusive transport in the IP medium does remarkably well in describing observed SEP events: This includes spectra, intensity profiles, anisotropies.
- We can similarly model heavy ion acceleration and transport in gradual events, even understanding differences in Fe / O ratios, for example.
- We have begun to model mixed events to explore the consequences of a pre-accelerated particle population (from flares, for example) and have also related this to the timing of flare - CME events.
- Have not discussed results for multi-D shocks and particle acceleration.

Particle acceleration via reconnection processes¹

G.P. Zank(1,2), P. Hunana (1), P. Mostafavi (2), J.A. le Roux(1,2), G.M. Webb(1), and O. Khabarova(3)

(1) Center for Space Plasma and Aeronomic Research

(2) Department of Space Science

University of Alabama in Huntsville

(3) Heliophysical Laboratory, IZMIRAN, Troitsk, Moscow

1

THE ASTROPHYSICAL JOURNAL, 797:28 (18pp), 2014 December 10

© 2014. The American Astronomical Society. All rights reserved. Printed in the U.S.A.

doi:10.1088/0004-637X/797/1/28

PARTICLE ACCELERATION VIA RECONNECTION PROCESSES IN THE SUPERSONIC SOLAR WIND

G. P. ZANK^{1,2}, J. A. LE ROUX^{1,2}, G. M. WEBB¹, A. DOSCH¹, AND O. KHABAROVA³

Derive a first-order correct equation for a nearly isotropic distribution function

$$\begin{aligned}
 & \frac{\partial f_0}{\partial t} + (U_i + 3|V_E|_i) \frac{\partial f_0}{\partial x_i} - \frac{c}{3} \frac{\partial U_i}{\partial x_i} \frac{\partial f_0}{\partial c} + \frac{1}{c^2} \frac{\partial}{\partial c} \left(\frac{c^3}{3} 2\eta_c f_0 \right) \\
 & = \frac{\partial}{\partial x_i} \left(K_{ij} \frac{\partial f_0}{\partial x_j} \right) - c \frac{\partial}{\partial x_i} \left(|V_E|_i \frac{\partial f_0}{\partial c} \right) - |V_E|_i c \frac{\partial^2 f_0}{\partial x_i \partial c} \\
 & + 3 \frac{V_E^2}{\tau_s} \frac{1}{c^2} \frac{\partial}{\partial c} \left(c^2 \frac{\partial f_0}{\partial c} \right) + \frac{1}{5} \left(\frac{1}{3} \frac{\partial U_i}{\partial x_i} + \frac{\eta_c}{3} + \eta_m \right)^2 \\
 & \times \frac{1}{c^2} \frac{\partial}{\partial c} \left(c^2 \kappa_s \frac{\partial f_0}{\partial c} \right). \tag{16}
 \end{aligned}$$

First-order convection due to induced electric field

First-order energization by induced electric field, island contraction, and flow gradient

Second-order energization due to contraction, merging and flow

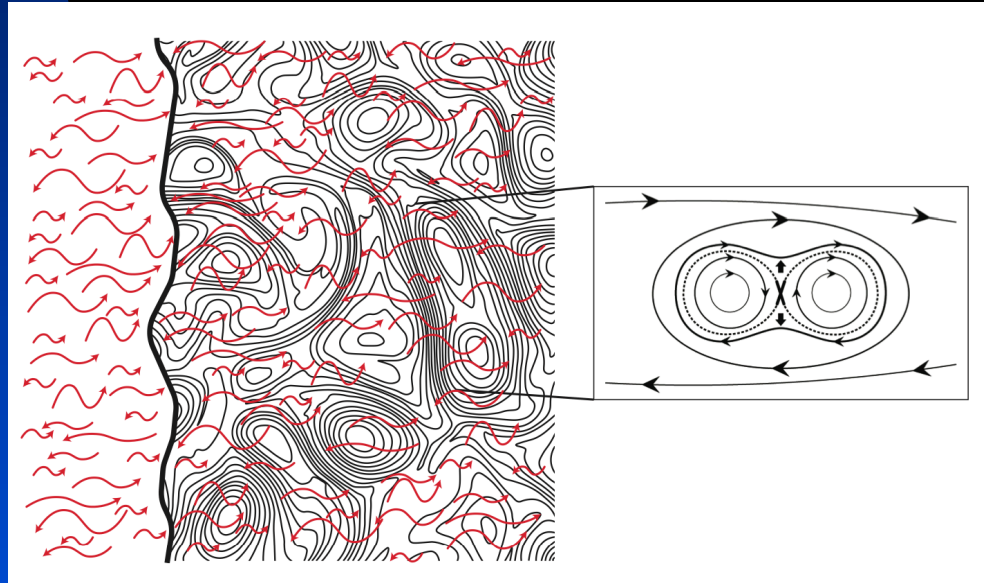
Diffusion due to particle scattering

Consider two applications:

- 1) Magnetic islands distributed throughout the supersonic solar wind - particularly in neighborhood of current sheet.*
- 2) Particle acceleration at fast mode shock waves.*

Why shocks?

- i) Shocks generate vortical turbulence which is advected downstream (e.g., Giacalone & Jokipii, 2007)*

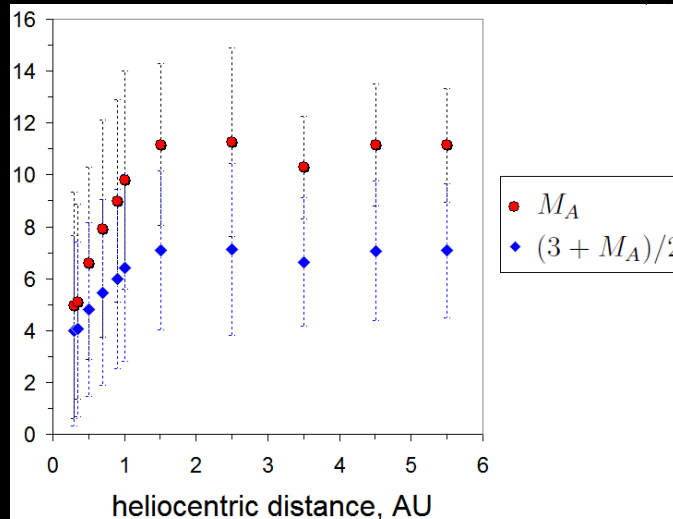
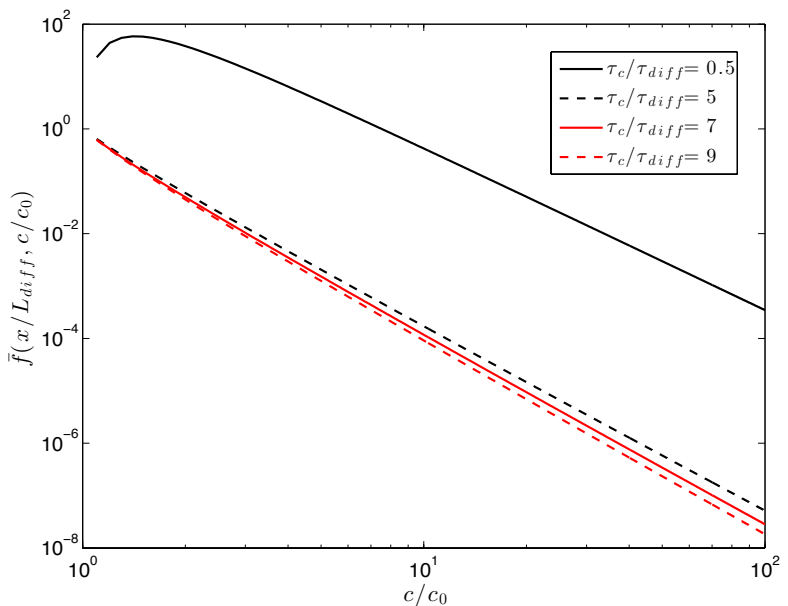
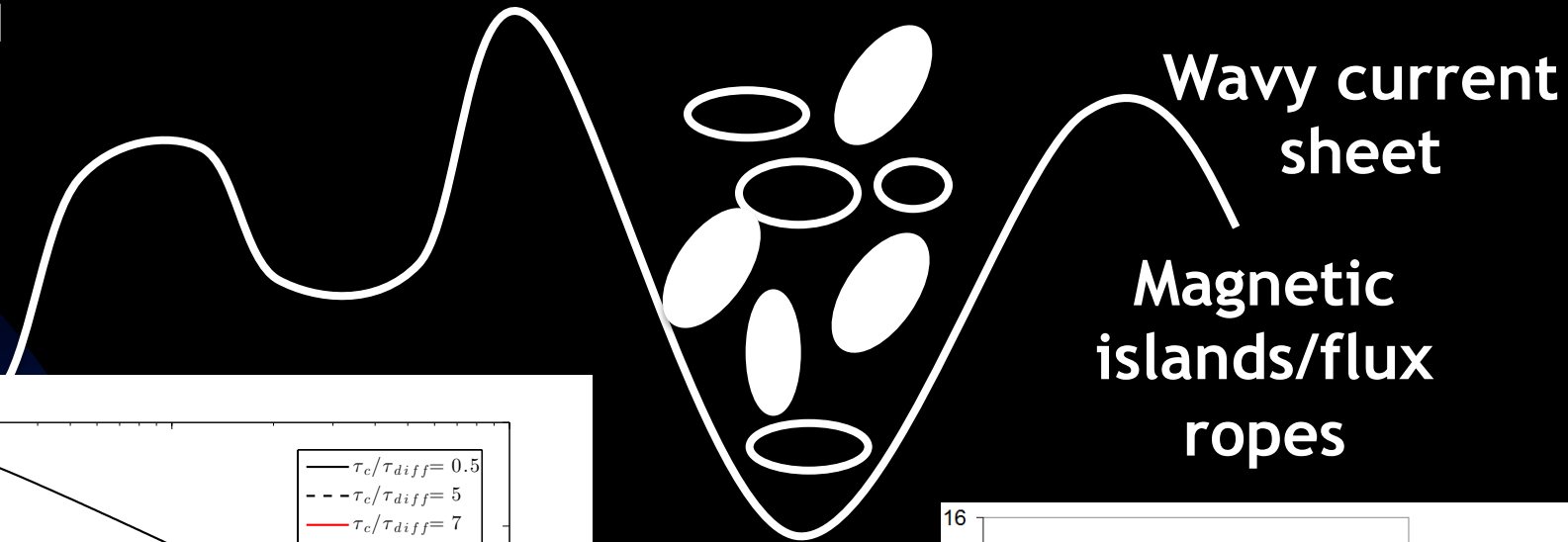


Consider two applications:

- 1) Magnetic islands distributed throughout the supersonic solar wind - already discussed.*
- 2) Particle acceleration at fast mode shock waves.*

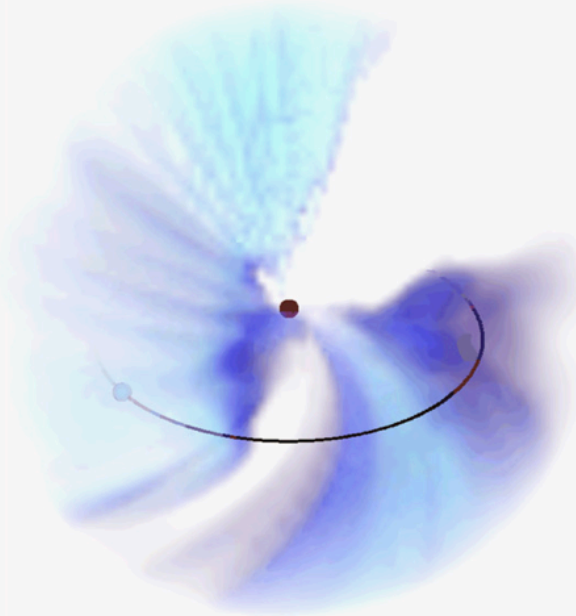
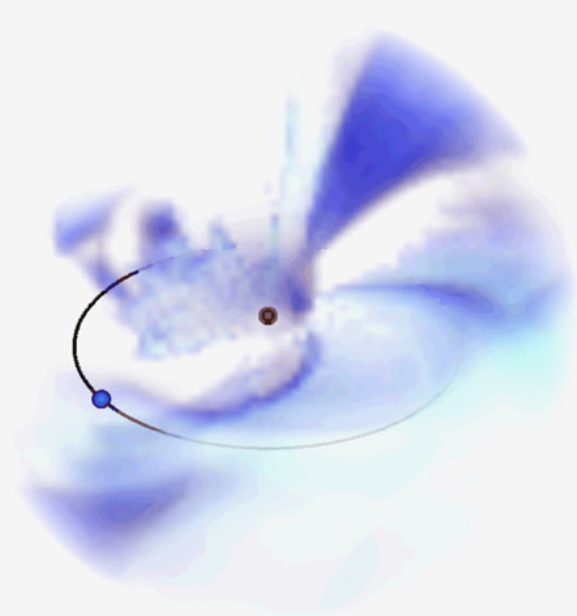
Why shocks?

- i) Shocks generate vortical turbulence which is advected downstream (e.g., Giacalone & Jokipii, 2007).*
- ii) Despite predicted particle intensity profile peaking at shock in DSA, HTS did not exhibit this behavior for ACR component [Stone et al., 2008], intensity of electrons increases rapidly after passage of shock [Stone et al., 2008 for IHS] and in solar wind [e.g., Ho et al., 2008].*
- iii) Spectra observed at interplanetary shocks often harder than predicted by DSA, just as often softer, and there appears to be no correlation between predicted spectral slope and shock compression ratio [Neergaardt-Parker & Zank, 2013; van Ness et al., 1984].*

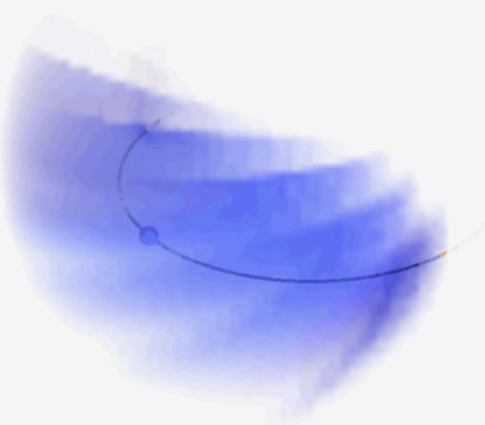


Normalized solution for particles accelerated by the anti-reconnection electric field and magnetic island contraction. Five curves are plotted, two for values of $\tau_c/\tau_{diff} < 1$ and three for $\tau_c/\tau_{diff} > 1$.

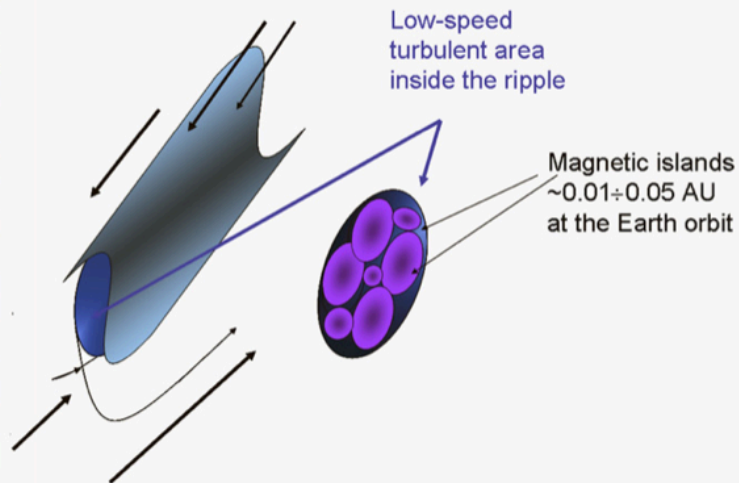
(a) These solutions assume that $M_A = 7$, which is possibly appropriate for the inner heliosphere within 1 AU or for periods of solar minimum.

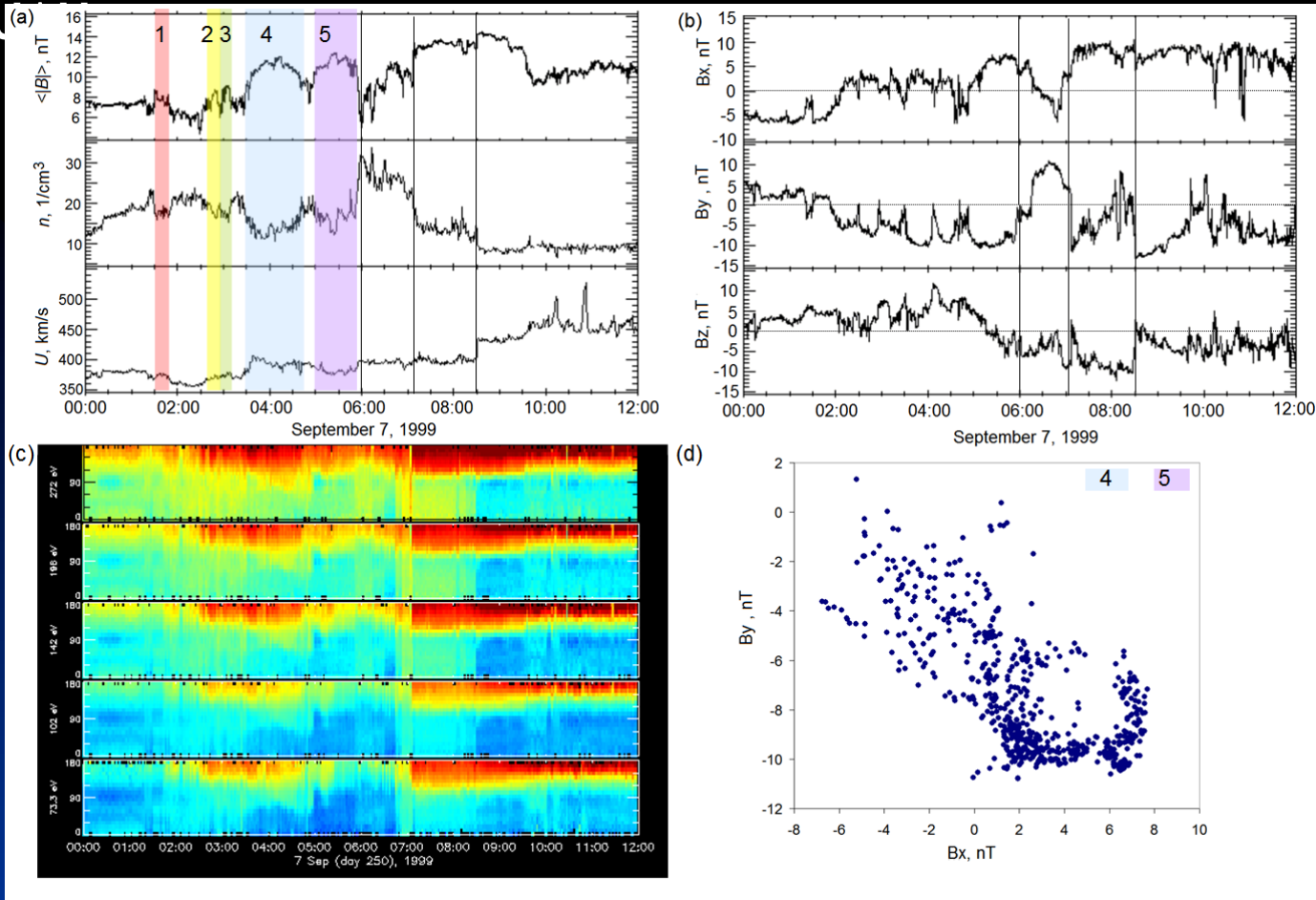


CASS ↔ UCSD STEL
2007/11/28 21



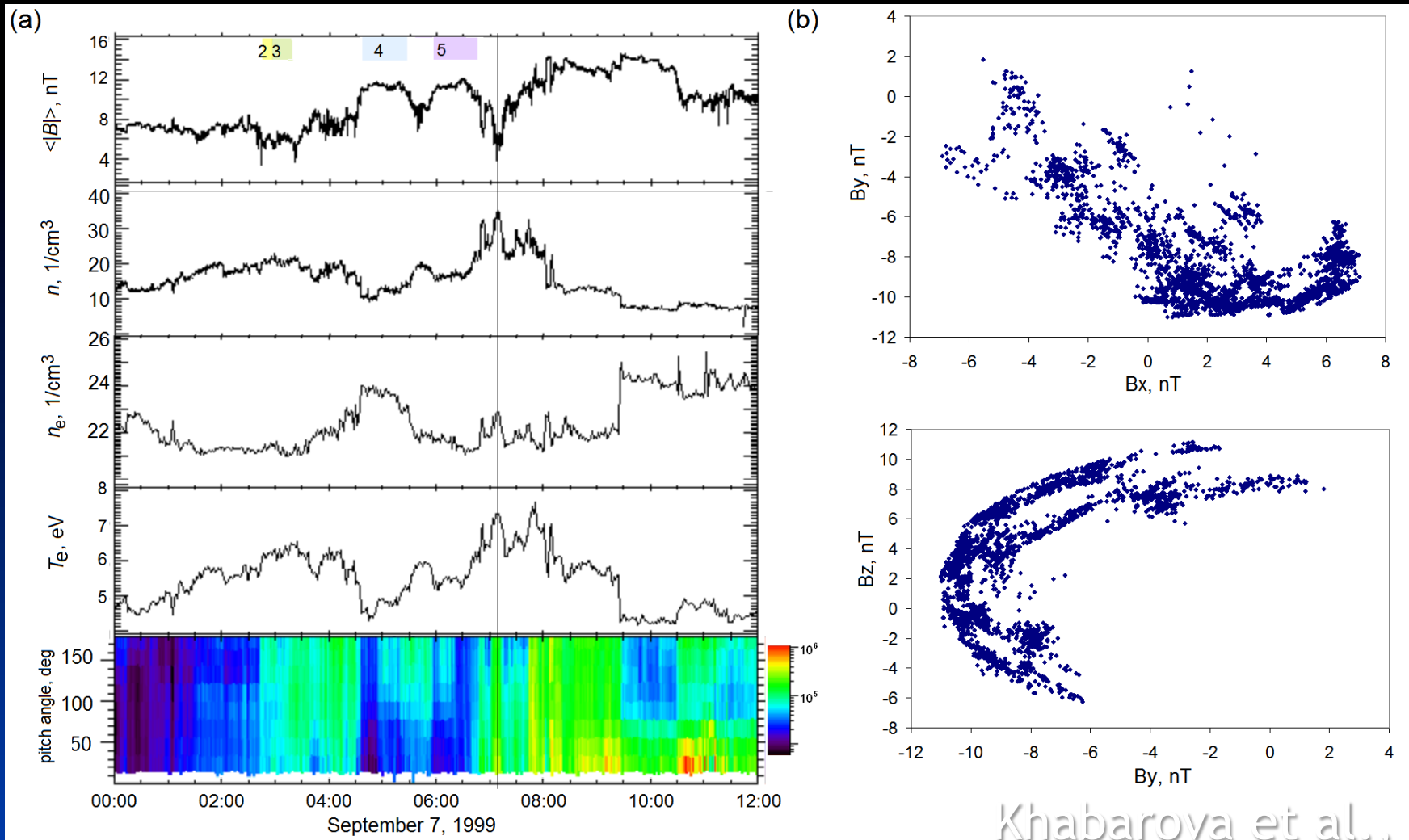
V (km s⁻¹)
500





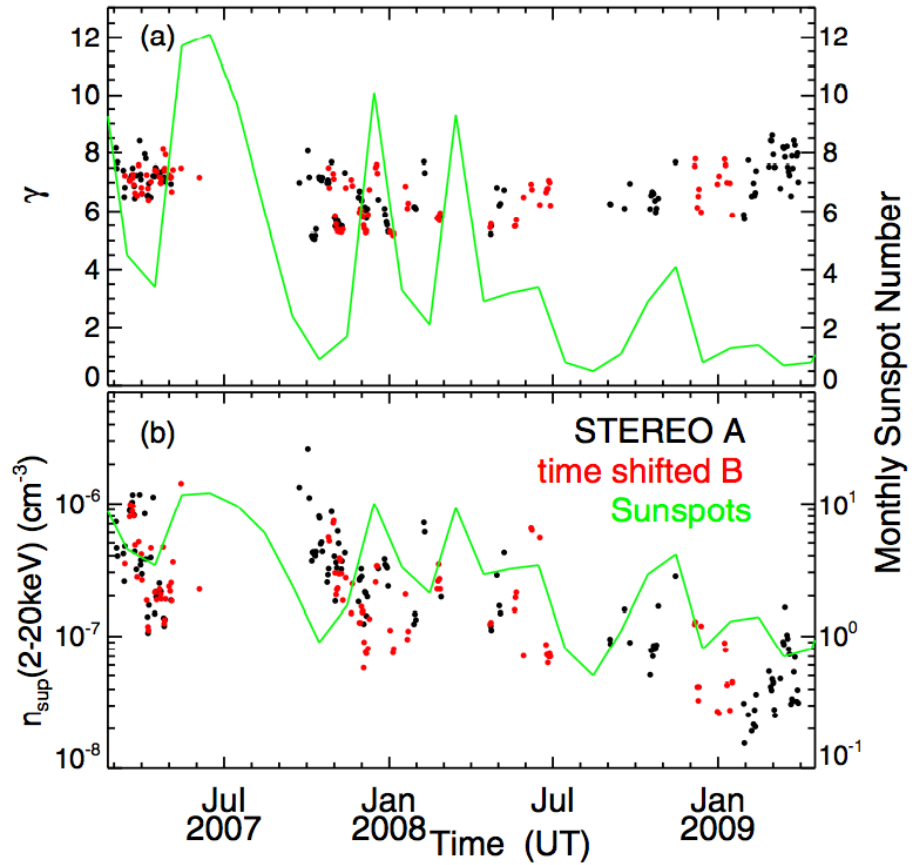
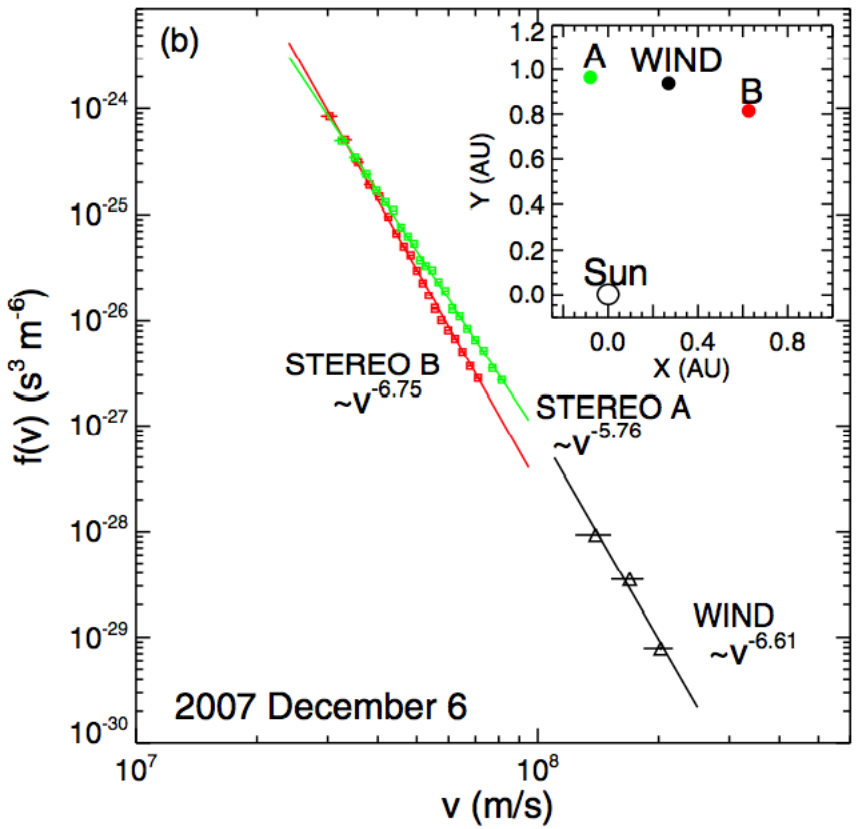
Khabarova
et al., 2015

Merging magnetic islands observed by ACE near heliospheric current sheet crossing of 7 September, 1999. (a) Magnetic field strength, plasma density, SW speed. Three small-scale and two medium-scale magnetic islands are identified by colored strips. Vertical black lines identify main crossings of heliospheric current sheets. (b) Components of IMF in GSE coordinates. (c) ACE SWEPAM suprathermal electron PADS. (d) Hodogram of the magnetic field variations in the ecliptic plane inside the magnetic islands 4 and 5.



Khabarova et al., 20

Figures show ongoing merging of islands 4 and 5. Smaller islands 2 and 3 already merged - island 3 swallowed island 2! Merging and elongation of islands results in widening of magnetic islands 4 and 5 as well as x-line area between

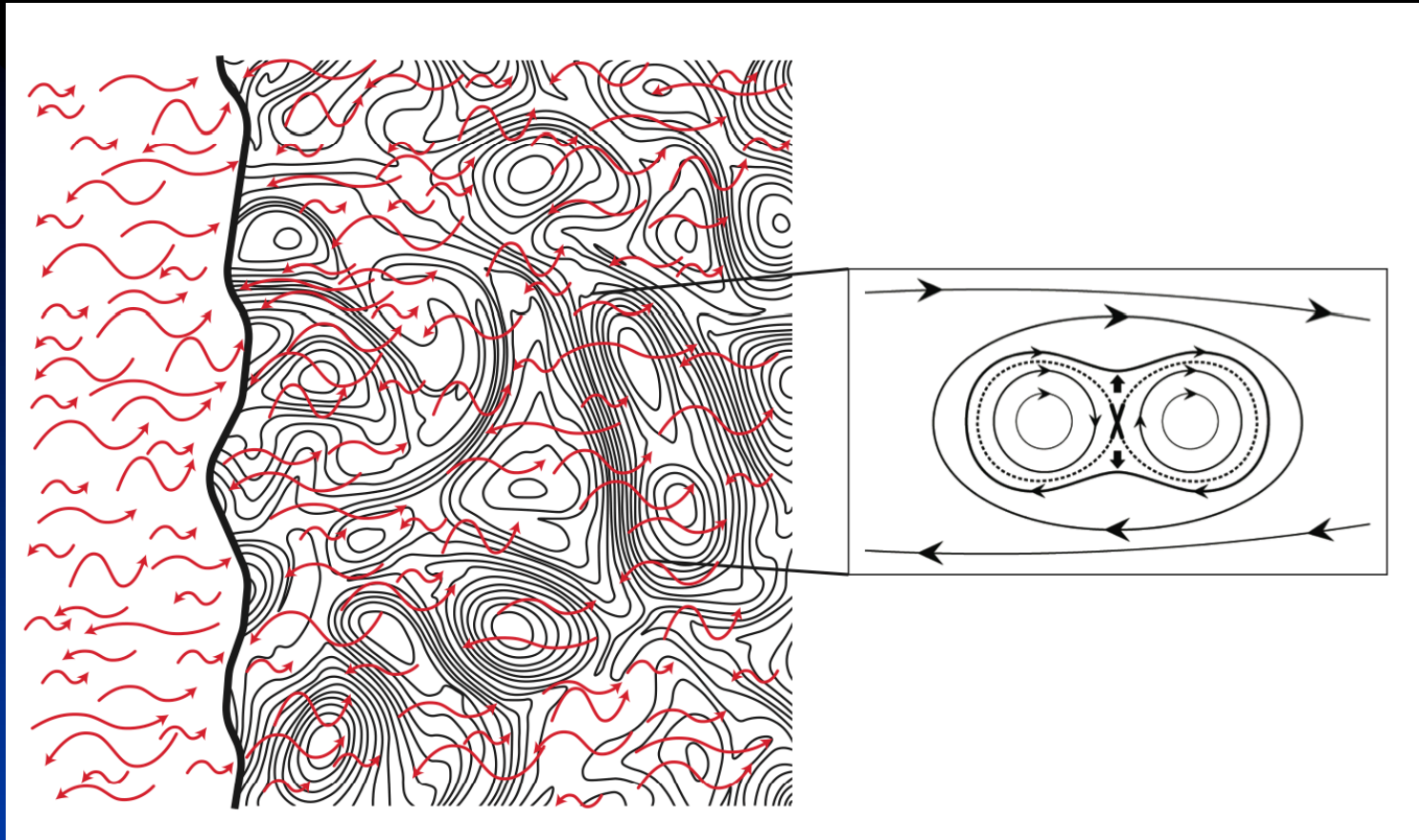


Wang et al 2014: quiet time electron distributions in the ecliptic from 2 - 20keV: power laws with index $\sim q = -6.6$

Several conclusions, some of which discussed and others not:

- 1) Multiple-reconnection is a fundamental dissipative process in an evolving turbulent magnetized plasma, and the turbulent cascade produces a distribution of reconnecting magnetic islands. Most apparent in vicinity of current sheet.
- 2) In the presence of a strong guide magnetic field, MHD turbulence is anisotropic and exhibits a quasi-2D character with 2D-like reconnecting structures.
- 3) Transport theory for acceleration by particles interacting with multiple magnetic islands yields power law spectra that depend in part on M_A , and indices predicted to range from -5 to -7.
- 4) Evidence for magnetic islands and their dynamical evolution in vicinity of current sheet/
- 5) The quiet time electron distributions observed to be power law distributions with power law indices ~ -6.6 . Support for statistical acceleration by magnetic islands/ flux ropes.

CSPAR-UAH 2) *DSA at Fast mode Shocks in presence of Reconnection Processes²*



Upstream: no islands present; reduces to standard DSA

Downstream: plasmoids present; modified transport equation necessary

²Zank et al., ApJ, in press, 2015

Conservation form of transport equation:

$$\frac{\partial f}{\partial t} + \frac{\partial S_i}{\partial x_i} + \frac{1}{c^2} \frac{\partial}{\partial c} (c^2 J_p) = 0,$$

$$\mathbf{S} \equiv -\mathbf{K} \cdot \nabla f - \frac{c}{3} \frac{\partial f}{\partial c} (\mathbf{U} - 3|\mathbf{V}_E|),$$

streaming in space, and

$$J_p \equiv \frac{c}{3} (\mathbf{U} + |\mathbf{V}_E|) \cdot \nabla f + \frac{c}{3} 2\eta_c f,$$

Accelerated spectrum:

$$g(\xi) = \frac{3\bar{Q}}{U_1 - U_2} \frac{1}{\Gamma} \frac{1}{\alpha - 3} \left[((a - 3) + d(s_1 + 3)) \left(\frac{c}{c_0}\right)^{-3} + ((\alpha - a) - d(s_1 + \alpha)) \left(\frac{c}{c_0}\right)^{-\alpha} + d\beta \int_0^\xi (e^{-3\tau} - e^{-\alpha\tau}) \frac{e^{s_1(\xi-\tau)}}{\xi - \tau} I_1(\beta(\xi - \tau)) d\tau \right]. \quad (28)$$

$$f(x, \xi) = g(\xi) e^{(U_1/K)x}, \quad x < 0;$$

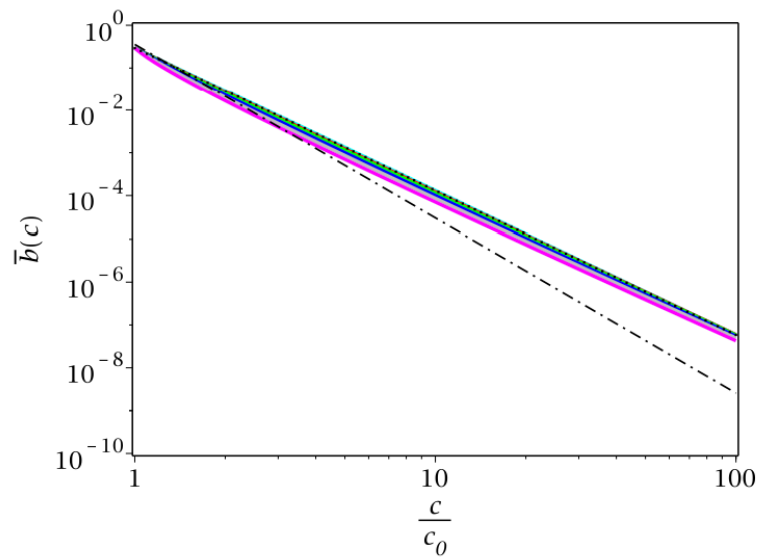
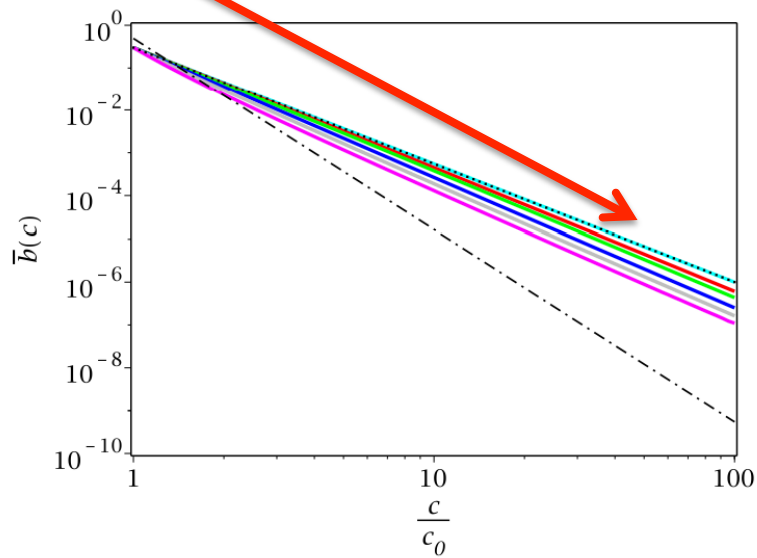
$$f(x, \xi) = e^{-\eta_c/(3|V_E|x)} g(\xi) + \frac{|V_E|}{K} x e^{-\eta_c/(3|V_E|x)}$$

$$\times \int_0^\xi g(\tau) e^{s_1(\xi-\tau)} \frac{\beta I_1\left(\beta \sqrt{(\xi - \tau) \left(\xi - \tau + \frac{2|V_E|x}{K}\right)}\right)}{\sqrt{(\xi - \tau) \left(\xi - \tau + \frac{2|V_E|x}{K}\right)}} d\tau, \quad x > 0.$$

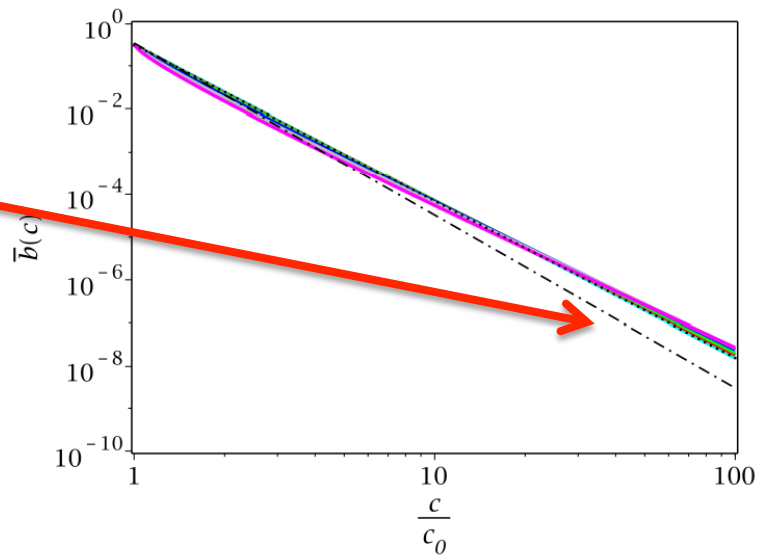
Complete upstream and downstream solution

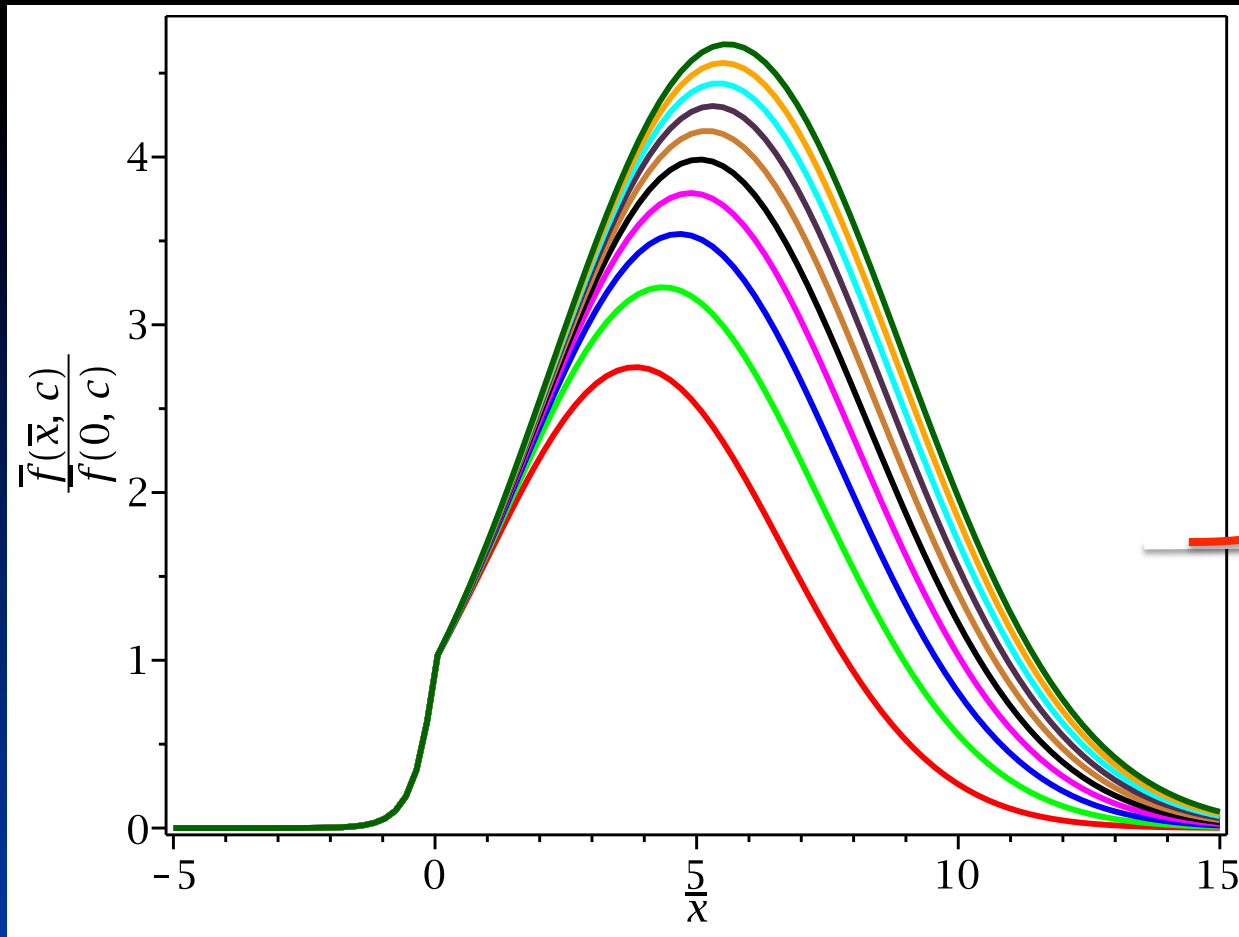
Spectra for the General Case

Induced electric field case

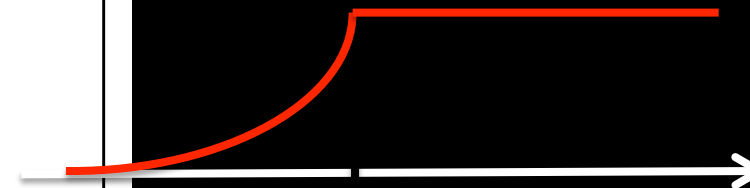


Conventional DSA





$$f(x,c)/f(0,x)$$



The amplification factor $f(x,c/c_0) / f(0,c/c_0)$ for fixed energies as a function of position for (left) magnetic island contraction-only case, (right) conventional DSA. Amplification factor ordered by energy i.e., largest energy has highest amplification; peak location ordered by energy i.e., highest energy has peak located furthest from shock.

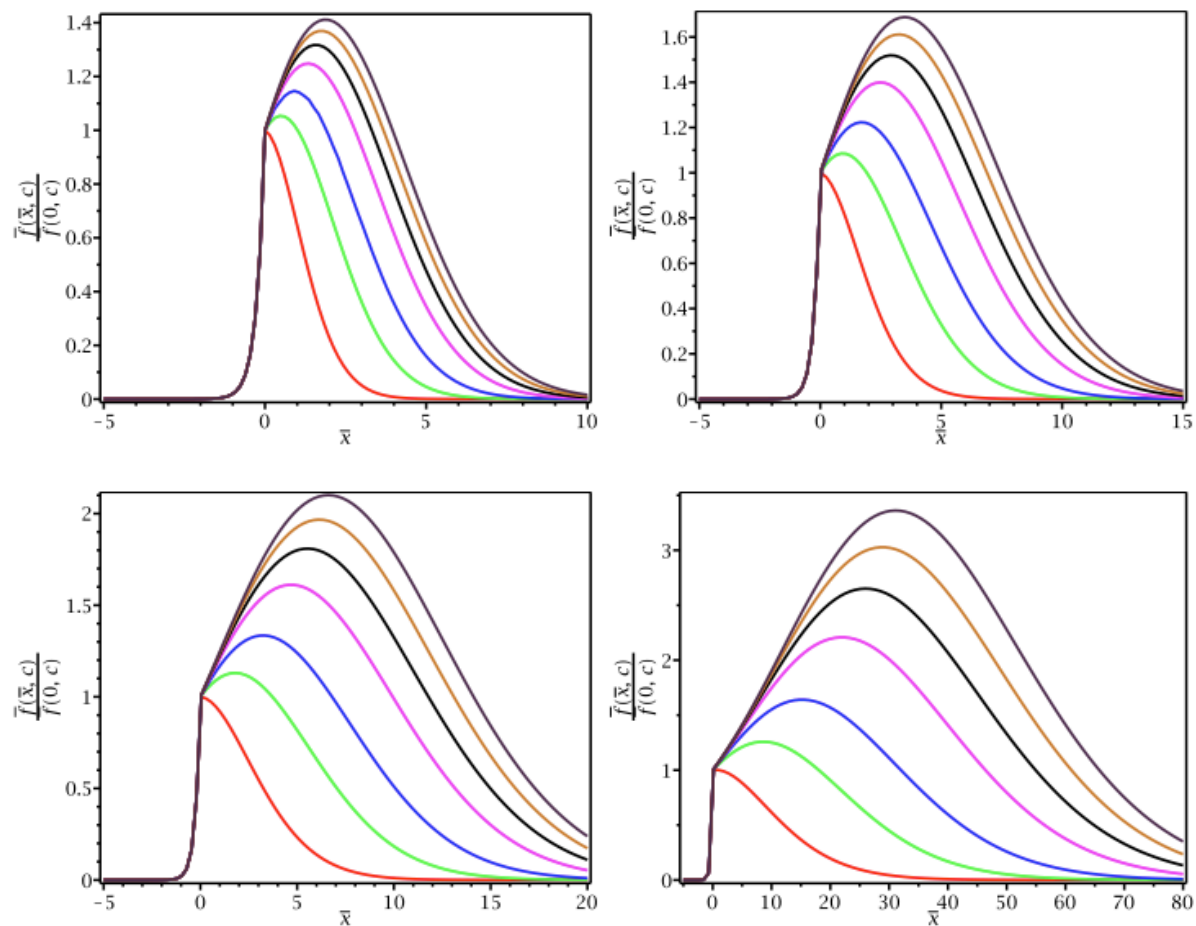
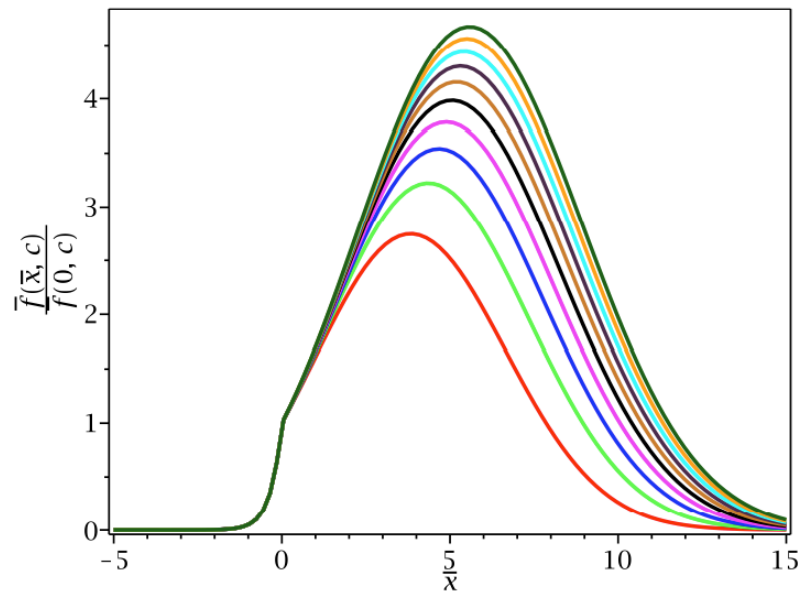
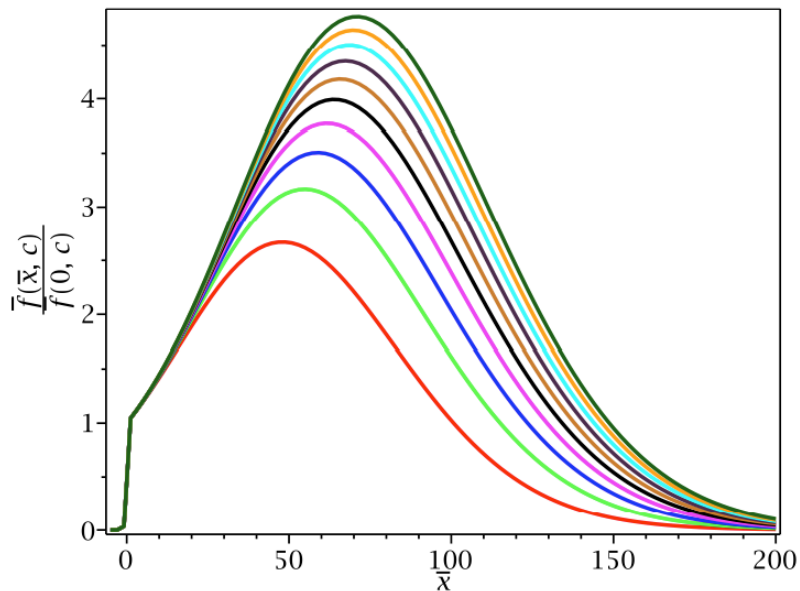
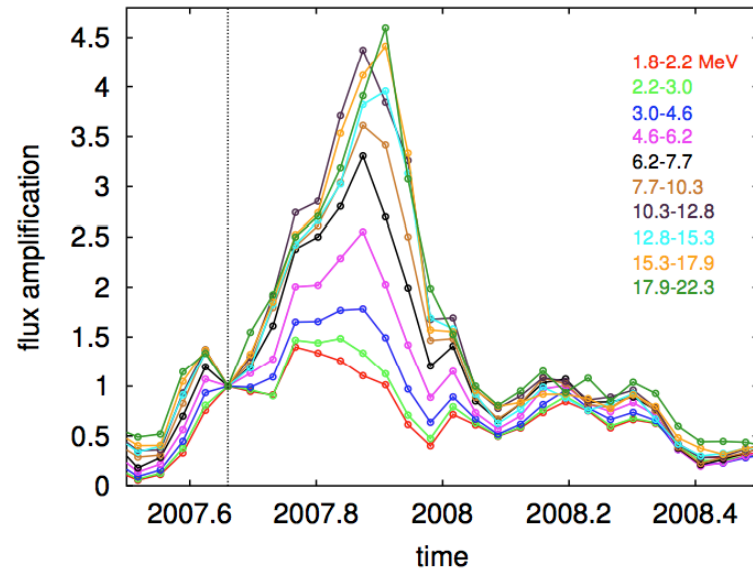
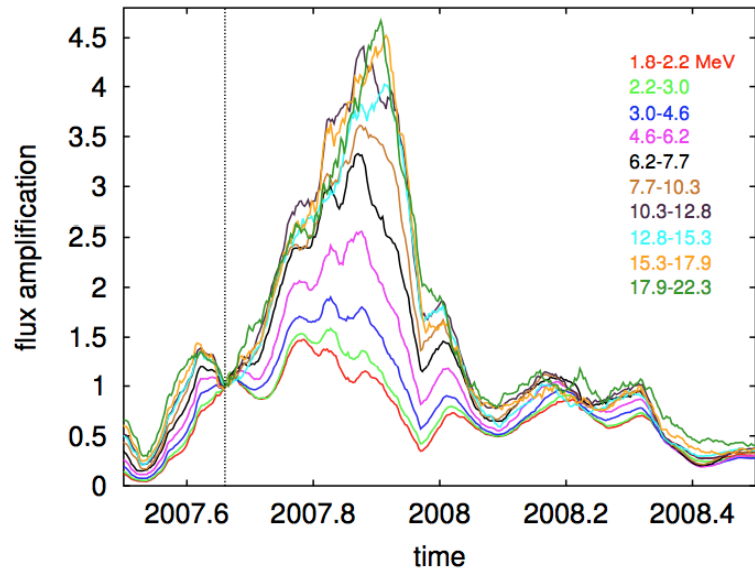


Fig. 12.— Particle intensity plots as a function of position, with the shock located at $x = 0$, for the general case, showing the peak location and the amplification factor relative to the value at the shock. The solution is for $U_2/|V_E| = 10$ and $r = 3.95$. The colors correspond to particle (square root of the) energy: $c/c_0 = 2$ (red line), $c/c_0 = 5$ (green line), $c/c_0 = 10$ (blue line), $c/c_0 = 20$ (magenta line), $c/c_0 = 30$ (black line), $c/c_0 = 40$ (gold line), $c/c_0 = 50$ (violet line). **Top left:** $\tau_{diff}/\tau_c = 2.0$, **Top right:** $\tau_{diff}/\tau_c = 1.0$, **Bottom left:** $\tau_{diff}/\tau_c = 0.5$, **Bottom right:** $\tau_{diff}/\tau_c = 0.1$.

Three important predictions for coupled DSA-reconnection particle acceleration emerge that distinguish this process from the conventional DSA model.

- 1) particle acceleration by a combined DSA-magnetic island contraction process yields particle spectra that are harder than the standard DSA spectrum for a given compression ratio;
- 2) particle intensities peak downstream of the shock and the peak location is ordered by particle energy, and
- 3) the particle intensity is amplified downstream of the shock, and the amplification factor is ordered by energy.

CSPAR-UAH Voyager 2 CRS data at HTS crossing: 13 day moving and non-moving averages.



- Multiple magnetic island-reconnection a primary dissipation process in an evolving turbulent magnetized plasma. Derived transport equation in a dissipative multi-reconnection super-Alfvenic plasma.
- Applied to steady solar wind (vicinity of HCS) and fast-mode shocks
- Predicts fairly steep (-5 to -7) power law spectra during quiet time solar wind - observed by Wang et al 2012 in electrons. Appears to be only viable explanation.
- DSA + Magnetic islands → three predictions
- Tested ideas against heliospheric termination shock observations of energetic particles - quite remarkable consistency with the energies considered. What about interplanetary shocks?
 - 1) Conventional DSA inconsistent with CRS observations
 - 2) Intensity peak and ordering of amplification with energy downstream of HTS consistent with DSA + Magnetic Islands
 - 3) Location of peak and ordering with energy downstream of HTS consistent with DSA + Magnetic Islands





The Radiation, Interplanetary Shocks, & Coronal Sources (RISCS) Toolset

G.P. Zank(1,2), E.K. Newton(1), C. Fry(1,3), J. H. Adams, Jr(1), P. Benson(4), and the RISCS Collaboration

(1) Center for Space Plasma and Aeronomic Research (CSPAR),
University of Alabama in Huntsville, Huntsville, AL 35805

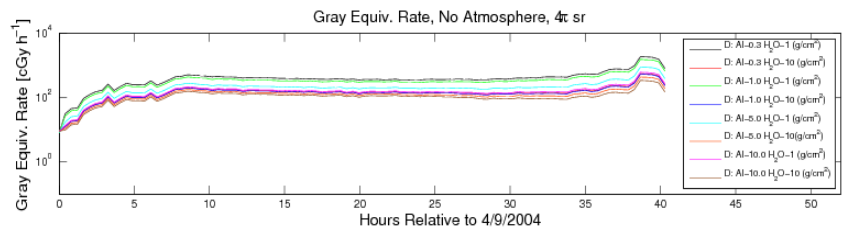
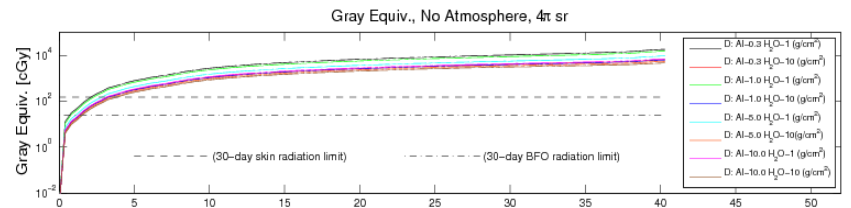
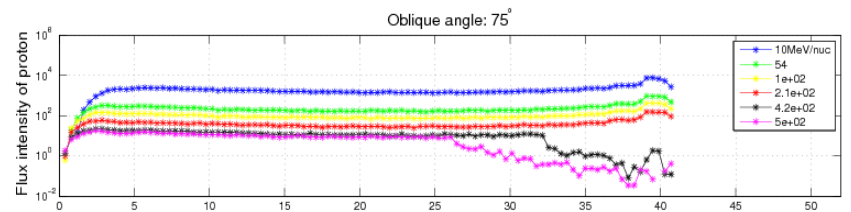
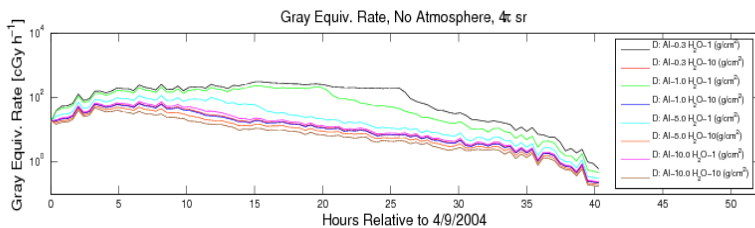
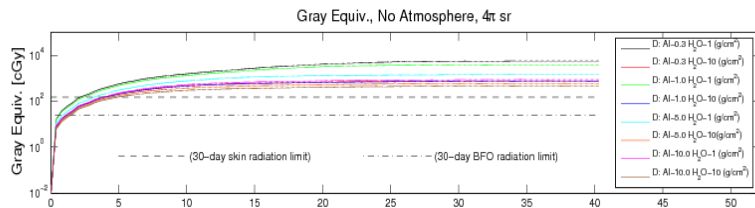
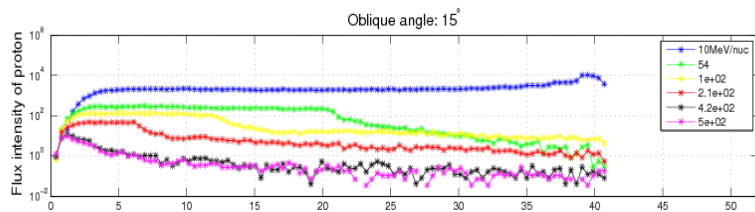
(2) Physics Department, University of Alabama in Huntsville, Huntsville,
AL 35899

(3) Exploration Physics International, Inc., 6275 University Dr NW,
Huntsville, AL 35806-1776

(4) NASA, Marshall Space Flight Center, MSFC/EV13, Huntsville, AL
35812

The goal of this project is to serve the needs of space system designers and operators by developing an interplanetary radiation environment model within 10 AU: Radiation, Interplanetary Shocks, and Coronal Sources (RISCS) toolset.

- The RISCS toolset will provide specific reference environments for space system designers and nowcasting and forecasting capabilities for space system operators.
- We envision the RISCS toolset providing the spatial and temporal radiation environment external to the Earth's (and other planets') magnetosphere, as well as possessing the modularity to integrate separate applications (apps) that can map to specific magnetosphere locations and/or perform the subsequent radiation transport and dosimetry for a specific target.



Top panel: PATH code modeled proton flux in a CME-driven shock SEP event at 1 AU with shock oblique angle 15 degree; middle panel: corresponding particle radiation dosage measured in Gray Equivalent; bottom panel: Gray Equivalent changing rate.

. Top panel: PATH code modeled proton flux in a CME-driven shock SEP event at 1 AU with shock oblique angle 75 degree; middle panel: corresponding particle radiation dosage measured in Gray Equivalent; bottom panel: Gray Equivalent changing rate.

Space System Designers & Operators: Needs & Deliverables

- Radiation in space arises primarily from three natural sources and can affect space systems and astronauts: 1) galactic cosmic rays; 2) solar energetic particles; and 3) energetic particles trapped in planetary magnetic fields.
- Two broadly defined space weather communities need to understand, anticipate, and mitigate such space radiation: space system designers and space system operators.
- Designers include engineers of crewed and non-crewed space systems and equipment for space-based activities (e.g., extra-vehicular activity).
- Operators include launch directors, spacecraft operators, and radiation exposure managers for crewed missions or commercial air travel.

Designer needs

- To design space systems for safe and reliable performance, designers need descriptions of specific reference environments.
- Typically a reference environment corresponds to the most severe conditions expected at some confidence level during a mission.
- Such a worst-case reference environment can be obtained by modeling the historical database using extreme value theory, yielding the peak differential energy spectra, the fluence spectra integrated over an episode of solar activity or over an entire mission, or the worst-case duration of fluxes above some threshold value.
- The selection of such reference environments is a non-trivial exercise and active area of research, requiring tools to develop climatological models (Adams et al., [2011])

Operator needs

- To ensure the safety and performance of mission and crew, space system operators need space situational awareness, i.e., reliable information on current space weather conditions and forecasts of near-term conditions (next hours to few days) extrapolated from current conditions, rather than simply predicted by climatological models.
- Whether focused on astronauts' radiation exposure, as NASA Johnson Space Flight Center Space Radiation & Analysis Group (SRAG) is, or that of commercial, military and federal space systems, space weather support is critical for determining appropriate operational responses, ranging from 'riding it out' or delaying plans, to safing, lowering voltages, restricting operations, or shutting down sensitive subsystems.
- What is needed [Adams et al. 2008 in report to the JSC SRAG)
 - 1) predictions of the temporal evolution profile of the next most likely Solar Energetic Particle (SEP) event at selected energies with associated probabilities, before particles begin to arrive;
 - 2) the capability to refine the temporal profiles and associated probabilities as the data arrive in real-time;
 - 3) reliable forecasts of no solar activity of interest, that is, all-clear forecasts.

Software Deliverables: An Operational Toolset as a Strategic Capability

- Serving these two space weather service provider communities requires three critical components:
 - a) probabilities for incipient solar activity (both “all clear forecasts” and the “when, where, and how strong” for outbursts);
 - b) the ability to use these probabilities and daily solar coronal and solar wind observations to continuously model the 3D time-dependent heliosphere within 10 AU; and
 - c) the ability to model the acceleration and transport of energetic protons and heavy ions based on “events” that are occurring or are forecast to occur in the heliosphere.

- RISCS toolset will provide all three elements:
 - 1) MAG4: predicts active region outbursts with up to 72 hours warning
 - 2) HAFv3 and MS-FLUKSS: kinematic and MHD modeling of interplanetary background and event-driven solar wind
 - 3) PATH: Particle Acceleration and Transport throughout the Heliosphere code

Figure 1: Conceptual Flow of the RISCS Toolset Serving Space Weather Service Providers

Figure 1a: RISCS Toolset for Space System Designers

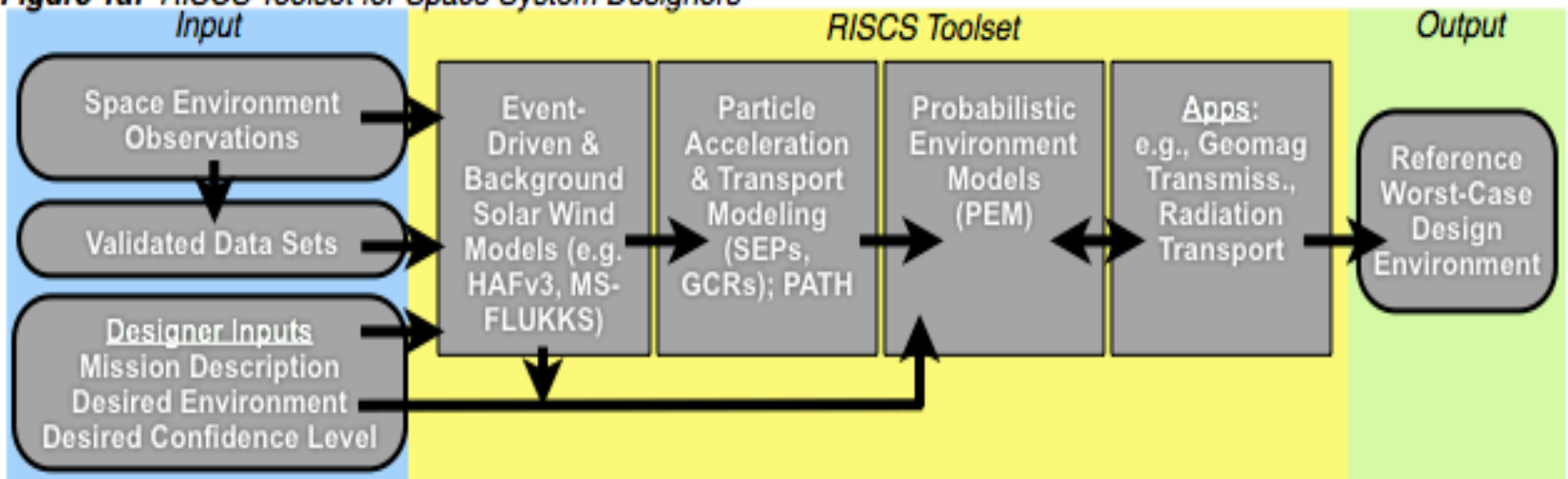
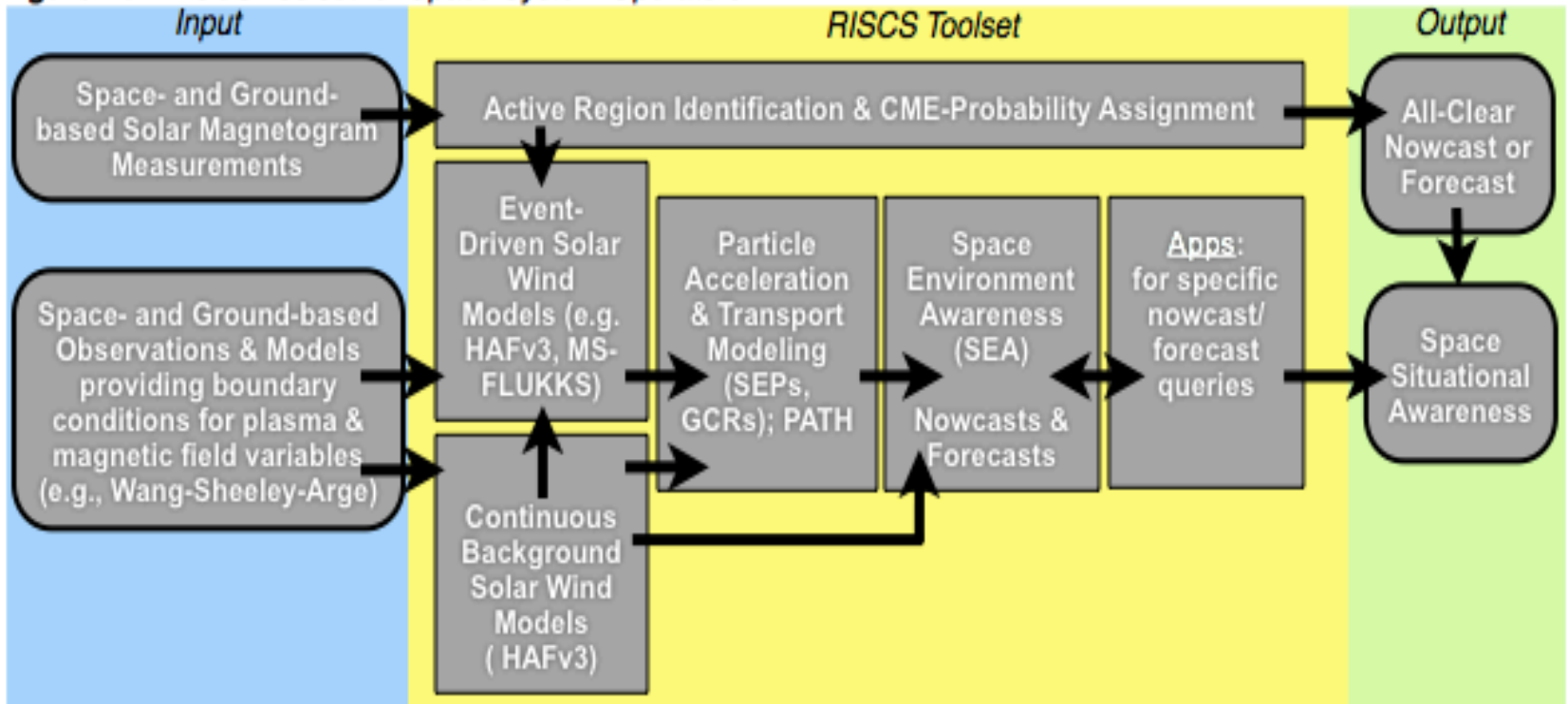


Figure 1b: RISCS Toolset for Space System Operators



Summarizing the RISCS

The RISCS toolset will provide a web-based “front-end” operational forecast and “nowcast” capability. The front-end dashboard will provide

- 1) predicted solar energetic particle (SEP) intensities;
- 2) spectra of protons and heavy ions;
- 3) predicted maximum energies and their duration;
- 4) SEP composition;
- 5) cosmic ray intensities, and
- 6) plasma parameters, including shock arrival times, strength and obliquity at any given heliospheric location and time.
- 7) The toolset will have a 72 hour predicative capability, with associated probabilistic bounds, that will be updated hourly thereafter to improve the predicted event(s) and reduce the associated probability bounds.
- 8) This toolset will also provide designers with worst-case reference environments that can be use for mission planning and space system design.
- 9) The RISCS toolset will be highly portable and capable of running on a variety of platforms including those of the Community Coordinated Modeling Center (CCMC).